Carbon Nanofibrous Binary and Ternary Composites as High-Performance Electrodes for Supercapacitors

A Thesis submitted in the partial fulfillment of the requirements for the award of the degree of

DOCTOR OF PHILOSOPHY IN
CHEMICAL ENGINEERING

by

Mr. DONTHULA KIRAN

(Roll No: 719084)

Under the guidance of

Dr. MANOHAR KAKUNURI
(Supervisor)

DEPARTMENT OF CHEMICAL ENGINEERING
NATIONAL INSTITUTE OF TECHNOLOGY
WARANGAL, (TELANGANA),
INDIA-506004

November 2023

DECLARATION

This is to certify that the work presented in the thesis entitled **"Carbon Nanofibrous Binary and Ternary Composites as High-Performance Electrodes for Supercapacitors"**, is a trustworthy work done by me under the supervision of Dr. Manohar Kakunuri was not submitted in another place for the award of any degree.

I declare that all ideas and words in this submission are mine alone, without the involvement of other people's words or ideas. The original sources have been adequately referenced and cited. In addition, I declare that I have abided by all of the principles of academic and integrity and honesty in this submission and did not misinterpret, fabricate or falsify any information, data, or fact. If these guidelines are violated, the Institute will take disciplinary action against me and the sources whose work was not properly cited or permission wasn't obtained when required will also face consequences.

Date:
Place: Warangal

Mr. Kiran Donthula)

Research Scholar

Roll No.719084

CERTIFICATE

This is to certify that the thesis entitled **"Carbon Nanofibrous Binary and Ternary Composites as High-Performance Electrodes for Supercapacitors"** that is being submitted by **Mr. Kiran Donthula** in partial fulfillment for the award of Doctor of Philosophy (**Ph.D.)** in the Department of Chemical Engineering, National Institute of Technology, Warangal, is a record of trustworthy work carried out by him under my supervision and guidance. I have not submitted any parts of this thesis for degree or diploma awards to any other universities or institutes.

Dr. Manohar Kakunuri
Assistant professor
Department of Chemical Engineering
National Institute of Technology Warangal

ACKNOWLEDGEMENT

It is with great pleasure that I express my gratitude and heartfelt worship to my esteemed supervisor **Dr. Manohar Kakunuri,** Assistant professor, Chemical Engineering Department, National Institute of Technology, Warangal - 506004, Telangana state, India for his constructive suggestions, unreserved guidance, unabashed inspiration, thought provoking discussions and in encouragement this research work. I have had the pleasure of spending many opportune moments under the expert guidance of the perfectionist at the peak of professionalism. As a result of the alacrity, inspiration, and ardent personal interest displayed by him during the writing of this thesis, the present work is a testament to his assiduity, enthusiasm, and personal commitment.

I wish to sincerely thank university authorities, **Prof. Bidyadhar Subudhi**, Director, National Institute of Technology, Warangal and other top officials who gave me an opportunity to carry out research work.

I also sincerely thank **Dr. P.V. Suresh**, Head, Chemical Engineering Department, National Institute of Technology, Warangal for his continuous support towards carrying out research work.

I wish to express my sincere and whole hearted thanks and gratitude to my doctoral scrutiny committee (DSC) members **Dr. Raghu Raja Pandiyan K**, Assistant Professor, Department of Chemical Engineering, **Dr. Ramya Araga,** Assistant Professor, Department of Chemical Engineering and **Dr. Rakesh Kumar Rajaboina,** Assistant Professor, Department of Physics, National Institute of Technology, Warangal for their kind help, encouragement and valuable suggestions for successful completion of research work.

I would like to extend my thanks to all the faculty members in Department of Chemical Engineering for their valuable suggestions and encouragement.

I am also thankful to all the supporting and technical staff of Department of Chemical Engineering who has directly or indirectly helped during the course of my work.

I am thankful to all my fellow colleagues' research scholars and specially, to Dr. Basant Kumar, Dr. Usha Rani, Mrs. Kamala Thota, Mr. Vamshi, Mr. Dinesh, Mr. Dilip Kumar and Mr. Surya Teja and Mr. Sampath Kumar, Dr. Ankit for their constant help for research samples characterization.

Gratitude is not enough to express my sincere gratitude to my family members for their constant love and support. Their blessings have made my journey worthwhile. In particular, I would like to thank my father Sri. **D. Rajaram**, mother Smt. **D. Shoba**, who has always been an encouragement to me during my higher studies. For their love and support, I am grateful to my sister and brother.

.

(Mr. Kiran Donthula)

ABSTRACT

In response to climate concerns and the global energy crisis, the focus has shifted to renewable energy sources like solar and wind power. However, their intermittent nature creates a challenge in matching energy supply with demand. Electrochemical energy storage devices, especially supercapacitors, offer advantages over batteries but lack high energy density. Scientists are tackling this by developing electrode materials with high capacitance and optimizing electrode architecture. The goal is to enhance supercapacitors' energy density while maintaining safety and power density, paving the way for more efficient and eco-friendly energy storage solutions.

This doctoral dissertation is devoted to the advancement of high-performance supercapacitors through the utilization of cutting-edge carbon-based materials, electrochemically stable metal oxides. The aim is to tackle and surpass the limitations typically associated with supercapacitors. In the present study, two dimensional MXene embedded carbon nanofiber (CNF) and pseudocapacitive material (metal oxides & conductive polymers) composites are synthesized using different techniques such as electrospinning, electrodeposition, and in-situ polymerization. Prepared electrode surface morphology, chemical composition, and microstructure analysis were performed using a range of techniques such as FESEM. HRTEM, XRD, FTIR, and BET surface area analysis. A thorough assessment of electrochemical performance was carried out using both two- and three-electrode systems using synthesized binary and ternary composites as electrode materials for the symmetric supercapacitor.

The first objective of the thesis deals with the synthesis of ruthenium oxide/MXene/CNF ternary nanocomposite using a facile electrospinning method. CNF is a host material in this nanocomposite, which acts as a backbone to the ruthenium oxide (RuO_2) and MXene. The electrochemical performance of the ternary composite electrode is investigated. The second aim involves synthesizing a polyaniline (PANI)/MXene/CNF core and shell ternary nanofibrous electrode. The core consists of MXene-embedded carbon nanofiber, while the shell is formed by PANI through the in-situ polymerization method. The electrochemical performance of electrodes with PANI coating for various times is investigated. The third attempt demonstrates the cobalt oxide (Co_3O_4) /MXene/CNF hollow nanofiber composite using core and shell electrospinning technique. Carbon nanofibers with embedded MXene and coated with cobalt oxide are used as high-performance electrodes for symmetrical supercapacitors.

The fourth objective demonstrates a facile technique to synthesize Co-based metal-organic framework MOFs and MXene embedded in CNFs. The electrochemical performance of electrodes with and without MOF was investigated and compared. The fifth objective deals with the development of an artificial neural network model for the prediction of carbon nanofibrous supercapacitors' performance. We have used a data-driven Artificial Neural Network (ANN) model to predict the performance of CNF electrodes based on the material microstructural properties and electrochemical operational parameters.

In summary, the outcomes from various systems of MXene and CNF-based nanocomposites demonstrate efficiency across different synthesis methods. We have explored diverse pathways for synthesizing nanostructured composite materials tailored for symmetrical supercapacitor applications. Notably, the MXene-assisted synthesis proved to be energy-efficient, exhibiting high performance and robust cycling stability. The combination of carbon nanofibers, MXenes, and metal oxides yielded a synergistic effect, leading to elevated specific capacitance, improved energy density, power density, and cycling stability.

Table of Contents

Declaration	ii
Certificate	iii
Acknowledgments	iv-v
Abstract	vi-vii
Table of contents	viii-xii
List of Figures	xiii-xvi
List of Tables	xvii
List of Abbreviations/symbols	xviii
Chapter-I: Introduction	1-32
1.1 Supercapacitor as an energy storage system	1
1.2 Historical background for the supercapacitors	2
1.3 Classification of supercapacitors based on the materials used and working principle	3
1.3.1 Classification based on the electrolyte used	6
1.4 Literature review	7
1.4.1 Electrode materials in EDLC	7
1.4.2 Pseudocapacitive materials	9
1.4.3 Hybrid composite materials for supercapacitors	11
1.4.4 Two Dimensional MXene based electrode materials for supercapacitors	12
1.4.5 Synthesis of MXene and Delaminating	13
1.4.6 Physicochemical properties of MXene and surface chemistry of MXene	14
1.4.7 MXene composite as supercapacitor electrodes	15
1.5 Motivation for the study and objective	17
1.6 Layout of the thesis	18
1.7 References	19
Chapter-II: Binder-free Ruthenium Oxide/MXene/Carbon Nanofiber Composite Electrode	33-50
2.1 Literature review	33
2.2 Materials and methods	34
2.2.1 Synthesis of MXene (Ti_3C_2Tx)	35

2.2.2 Preparation of the freestanding binary MXene/CNF composite electrode 35
2.2.3 Preparation of the freestanding ternary RuO_2/MXene/CNF composite 35
2.2.4 Material Characterizations 36
2.2.5 Electrochemical characterizations 37
2.3 Results and Discussion 37
2.3.1 Morphological and structural investigations 37
2.3.1.1. FESEM analysis of RuO_2/MXene/CNF and MXene/CNF nanocomposites 37
2.3.1.2 XRD analysis of RuO_2/MXene/CNF and MXene/CNF nanocomposites 38
2.3.1.3 FTIR analysis of RuO_2/MXene/CNF and MXene/CNF nanocomposites 39
2.3.1.4 HR-TEM analysis of RuO_2/MXene/CNF and MXene/CNF nanocomposites 39
2.3.1.5 Flexibility analysis of RuO_2/MXene/CNF nanocomposite 40
2.3.2 Electrochemical performance 41
2.3.2.1 CV analysis of RuO_2/MXene/CNF and MXene/CNF composite electrodes 41
2.3.2.3 GCD analysis of RuO_2/MXene/CNF and MXene/CNF composite electrodes 42
2.3.2.3 EIS analysis of RuO_2/MXene/CNF and MXene/CNF composite Electrodes 44
2.4 Conclusions 46
2.5 References 46
Chapter-III: Flexible Polyaniline/MXene/CNF Composite Nanofibrous Mats as Electrodes 51-72
3.1 Literature review 51
3.2. Experimental section 53
3.2.1. Chemicals 53
3.2.2. Synthesis of delaminated MXene $Ti_3C_2T_x$ layers 53
3.2.3. Preparation of flexible PANI/MXene/CNF electrode 53
3.2.4. Structural characterization 54

3.3. Results and discussion 55
3.3.1. Structural analysis composite materials 55
3.3.1.1 XRD analysis of PANI/MXene/CNF-1,2,3 and MXene/CNF 55
3.3.1.2 FTIR analysis of PANI/MXene/CNF-1,2,3 and MXene/CNF 55
3.3.1.3 FESEM analysis of PANI/MXene/CNF-1,2,3 and MXene/CNF 55
3.3.1.4 BET analysis of PANI/MXene/CNF-1,2,3 and MXene/CNF 58
3.3.1.5 XPS analysis of PANI/MXene/CNF-1,2,3 and MXene/CNF 59
3.3.1.6 Water contact angle analysis of PANI/MXene/CNF-1,2,3 and MXene/CNF 61
3.3.2. Electrochemical characterization of composite electrodes 62
3.3.2.1. CV analysis of PANI/MXene/CNF-1,2,3 and MXene/CNF nanocomposite electrode 62
3.3.2.2 GCD analysis of PANI/MXene/CNF-1,2,3 and MXene/CNF nanocomposite electrodes 64
3.3.2.3 EIS analysis of PANI/MXene/CNF-1,2,3 and MXene/CNF nanocomposite Electrodes 65
3.4 Conclusion 67
3.5 References 68
Chapter-IV: Hierarchically structured carbon nanofibers with embedded MXene and coated with cobalt oxide composite electrode 73-91
4.1. Literature review 73
4.2. Experimental 74
4.2.1. Materials and Reagents 74
4.2.2.1. Synthesis of Hollow MXene/CNF composite nanofibers 75
4.2.2.2 Synthesis of Co_3O_4 coated HMCNF Co_3O_4/HMCNF composite and characterization 76
4.3. Results and discussion 78
4.3.1 Morphology and structural characterization. 78
4.3.1.1 FESEM analysis of ternary and binary composites 78
4.3.1.2 XRD analysis of ternary and binary composites 80
4.3.1.3 Raman spectroscopy analysis of ternary and binary composites 80
4.3.1.4 XPS analysis of ternary and binary composites 81
4.3.1.5 BET analysis of ternary and binary composites 81
4.3.2 Electrochemical Characterization 82
4.3.2.1 CV analysis of ternary and binary composites 82

4.3.2.2 GCD analysis of ternary and binary composites 85

4.3.2.3 EIS analysis of Co_3O_4/HMCNF and HMCNF composite 86

4.4 Conclusions 87

4.5 References 87

Chapter-V: a Facile synthesis of Cobalt-MOF/MXene/carbon nanofiber composite electrode 92-106

5.1 Literature Review 92

5.2. Experimental 93

5.2.1. Preparation of Co-MOF nanoparticles 94

5.2.2. Synthesis of Co-MOF/MXene/CNF composite electrode 94

5.3. Results and discussion 95

5.3.1 Physicochemical properties of Co-MOF/MXene/CNF and MXene/CNF 95

5.3.1.1 FESEM analysis of Co-MOF/MXene/CNF and MXene/CNF 95

5.3.1.2 HR-TEM analysis of Co-MOF/MXene/CNF and MXene/CNF 96

5.3.1.3 XRD analysis of Co-MOF/MXene/CNF and MXene/CNF 97

5.3.1.4 FTIR analysis of Co-MOF/MXene/CNF and MXene/CNF 97

5.3.1.5 BET analysis of Co-MOF/MXene/CNF and MXene/CNF 98

5.3.2. Electrochemical Characterization 99

5.3.2.1 CV analysis of Co-MOF/MXene/CNF and MXene/CNF 99

5.3.2.2 GCD analysis of Co-MOF/MXene/CNF and MXene/CNF 100

5.3.2.3 EIS analysis of Co-MOF/MXene/CNF and MXene/CNF 101

5.4 Conclusion 103

5.5 References 103

Chapter-VI: Prediction of capacitance using artificial neural networks for carbon nanofiber-based supercapacitors 107-116

6.1. Literature review 106

6.2. Methodology 108

6.2.1 Experimental data collection and preprocessing 108

6.2.2 Artificial neural network 109

6.3. Results and Discussion 111

6.3.1 Result of ANN model 111

6.3.2 Sensitivity analysis 113

6.4. Conclusion 114
6.5 References 114
Chapter-VII: Overall Conclusions 117
Scope for further investigations 118
List of Publications 119

List of Figures

Figure No.	Figure caption	Page No.
Figure 1.1	Classification of supercapacitors based on working mechanism.	3
Figure 1.2	Mechanism of the electrical double layer (EDL) corresponding to (a) the Helmholtz	4
Figure 1.3	Different types of reversible redox mechanisms that give rise to charge storage: (a)redox reaction, and (b) intercalation pseudocapacitance.	5
Figure 2.1.	Schematic illustration of the synthesis of MXene and RuO_2/MXene/CNFs composites.	36
Figure 2.2.	SEM images of (a), (c) binary composite (MXene/CNFs) at low and high magnification and (b), (d). ternary composite (RuO_2/MXene/CNFs)	38
Figure 2.3	(a) XRD of RuO_2/MXene/CNFs composite and (b) FTIR patterns for CNF, MXene/CNF and RuO_2/MXene/CNFs composites.	39
Figure 2.4.	(a) Ternary composite single nanofiber HRTEM image (b) lattice fringes of RuO_2/MXene/CNF composite, (c) High magnification MXene lattice fringes and (d) High magnification RuO_2 lattice fringes images.	40
Figure 2.5.	Digital photographs of RuO_2/MXene/CNF composite twisted, bent of membrane (a-f).	40
Figure 2.6.	Cyclic voltammetry curves of (a) the binary and ternary composite at a scan rate of 5 mV s^{-1} (b) the ternary composite at different scan rates; GCD curves of (c) binary and ternary at 1 A g^{-1} current density, (d) GCD curves of ternary composite at various current densities.	42
Figure 2.7	Comparison of CV curves of (a) the ternary and binary composite at a scan rate of 5 mV s^{-1} (b) the ternary composite at different scan rates. GCD curves of (c) the ternary and binary composite at 1 A g^{-1} current density, (d) the ternary composite at various current densities.	43
Figure 2.8.	(a) Comparison of specific capacitances from GCD curves for binary and ternary composite electrodes; (b) EIS spectra of binary and ternary composite electrodes; (c) Ternary composite electrode cyclic performance at 1 A g^{-1} and (d) Ragone plot for binary and ternary composites.	45

Figure 3.1	Schematic representation of the synthesis of ternary composites based on PANI, MXene, and CNF	56
Figure 3.2	(a) XRD spectra of MXene/CNF and PANI/MXene/CNF composites, and (b) FTIR absorption spectrum of MXene/CNF and PANI/MXene/CNF composites	57
Figure 3.3	(a) FESEM images of (a) MXene/CNF composite at lower magnification and (b) at higher magnification; (c) EDX of MXene/CNF composite and corresponding element mapping images for the carbon, nitrogen, and titanium	57
Figure 3.4	FESEM images of (a, c, e) PANI/MXene/CNF ternary composite at low magnification and (b,d ,f) PANI/MXene/CNF ternary composite at high magnification. (g) HRTEM of Core and Shell structure of PANI and MXene/CNF (h) HRTEM image of Delaminated MXene layers in Ternary composite	59
Figure 3.5	(a) Average fiber diameter of binary and ternary composites with varying polymerization time; (b) Nitrogen adsorption/desorption isotherms of ternary and binary composites; (c) Pore size distribution of ternary composite and binary composites	60
Figure 3.6	High resolution core level XPS of (a) survey spectra, (b) C 1s, (c) Ti 2p and (d) N 1s of PANI/MXene/CNF-3 composite	61
Figure 3.7	Digital images of contact angle measurements on the surface of (a) PAN derived CNF; (b) MXene/CNF composite and (c-e) dynamic contact angle of PANI/MXene/CNF composite	62
Figure 3.8	Electrochemical performance of composite electrodes (a) CV curves for CNF, MXene/CNF and PANI/MXene/CNF-3 composites at 5 mV s^{-1} scan rate (b) CV curves for MXene/CNF and PANI/MXene/CNF-1,2,3 composites at 5 mV s^{-1} scan rate (c) CV curves at different current density for PANI/MXene/CNF-3 composite (d) GCD curves of CNF, MXene/CNF and PANI/MXene/CNF-1 composites at 0.5 A g^{-1} (e) GCD curves of MXene/CNF and PANI/MXene/CNF-1, 2, 3 composites at 0.5 A g^{-1} (f) GCD curves at different current density for PANI/MXene/CNF-3 composite	63

Figure 3.9	(a) Rate performance of binary and ternary composites at different current densities; (b) Nyquist plots of all electrodes-based supercapacitors in between the frequency range of 100 kHz - 0.01 Hz; (c) Cyclic stability (capacitance retention %) and coulombic efficiency of the ternary and binary at 1 A g^{-1}; (d) Ragone plots for the different MXene/CNF and PANI/MXene/CNF-3.	66
Figure 3.10	Digital images PANI/MXene/CNF-3 Composite (a) flat, (b) bent, and (c-d) rolled	67
Figure 4.1	Schematic illustrating the synthesis process of the Co_3O_4/HMCNF composite.	76
Figure 4.2	Typical FESEM images of (a, b) HMCNF (c, d) the FESEM images of Co_3O_4/HMCNF composite superstructures, (e, f) EDS spectrum obtained from HMCNF and Co_3O_4/HMCNF composite.	79
Figure 4.3	(a) comparison of X-Ray diffraction patterns, (b) Raman spectra of HMCNF and Co_3O_4/HMCNF composites.	80
Figure 4.4	(a) XPS full spectra ;(b) Co 2p spectra: (c) C 1s spectra: and (d) O 1s spectra	81
Figure 4.5	(a) BET hysteresis of as-prepared composites b) Pore size distribution curves	82
Figure 4.6	HMCNF and Co_3O_4/HMCNF composites (a) CV curve comparison (b) CV at different current densities (c) GCD comparison (d) GCD at different current densities and (e) Specific capacitance comparison	83
Figure 4.7	(a) CV curve at different series of voltage ranges for Co_3O_4/HMCNF (b) CV curves comparison for Co_3O_4/HMCNF at different scan rates (c) GCD curves comparison for HMCNF and Co_3O_4/HMCNF electrodes (d) GCD curves comparison for Co_3O_4/HMCNF at different current densities	84
Figure. 4.8	(a) Specific capacitance values of Co_3O_4/HMCNF and HMCNF composites at different current densities (b) Nyquist plot for Co_3O_4/HMCNF and HMCNF composites (c) capacitance retention (%) curves comparison for HMCNF and Co_3O_4/HMCNF electrodes (d) Ragone plot comparison for Co_3O_4/HMCNF.	86

Figure 5.1	Schematic for synthesis of Co-MOF and MXene embedded CNF composite	95
Figure. 5.2	FESEM images (a) and (b) with higher magnification and lower images of Co-MOF in DMF as solvent (c) and (d) FESEM images with higher magnification and lower images of Co-MOF in Methanol as solvent	96
Figure. 5.3	FESEM images (a) &(b) of Co-MOF/MXene/CNF at lower and higher magnification	96
Figure. 5.4	(a-d) HR-TEM images of Co-MOF/MXene/CNF	97
Figure. 5.5	(a) XRD comparison of Co-MOF and Ternary composite (b) FTIR spectra comparison for Ternary and binary composite.	98
Figure. 5.6	(a) N_2 absorption-desorption isotherms and (b) pore size distribution of Co-MOF/MXene/CNF and MXene/CNF	99
Figure. 5.7	(a) CV curves comparison for ternary and binary composite (b) CV curve comparison for ternary composite at various scan rates (c)GCD comparison for ternary composite at various current density (d)GCD comparison or binary and ternary composite at current density of 1 A g^{-1}	100
Figure 5.8	(a) Specific capacitance values of Co-MOF/MXene/CNF and MXene/CNF composites at different current densities (b) capacitance retention (%) curves comparison for HMCNF and Co_3O_4/HMCNF electrodes (c) Nyquist plot for Co-MOF/MXene/CNF and MXene/CNF composites (d) Ragone plot comparison for Co-MOF/MXene/CNF and MXene/CNF.	102
Figure 6.1	The neural network model of ANN used in this study.	110
Figure 6.2	Schematic representation of data-driven modeling methodology	111
Figure 6.3	Pearson correlation matrix of the seven input variables and single output variable (specific capacitance).	112
Figure. 6.4	The predicted and actual values of specific capacitance in both test and training, using the ANN.	113

List of Tables

Table No.	Table caption	Page No.
Table 1.1	Electrochemical performance comparison of various carbonaceous materials used as supercapacitor electrodes.	8
Table 1.2	Electrochemical performance comparison for various Conducting polymers used as supercapacitor electrodes.	9
Table 1.3	Different composite electrodes reported for supercapacitor applications.	12
Table 2.1	Specific Capacitance Performance of different Ruthenium Oxide/various Carbon composites	46
Table 3.1	Electrochemical performance comparison for various PANI based composite electrode for supercapacitor	65
Table 5.1	Comparison for various MOF based composites performances	103
Table 6.1	Various machine learning model to predict the performances	107
Table 6.2	Performance of ANN vs. Number of neurons in hidden layer	112
Table 6.3	Sensitivity analysis of the ANN model versus independent variables.	114

List of Abbreviations/Symbols

Abbreviations /Symbol	Description
EDLC	Electrochemical double layer capacitor
CNF	Carbon nanofibers
SSA	Specific surface area
PANI	Polyaniline
PPy	Polypyrrole
CP	Conducting polymer
APS	Ammonium persulfate
XRD	X-ray diffraction
FT-IR	Fourier Transform Infrared Spectroscopy
XPS	X-ray photoelectron spectroscopy
FESEM	Field Emission Scanning electron microscope
HRTEM	Transmission electron microscope
SCE	Standard saturated calomel electrode
PVDF	Polyvinylidene fluoride
NMP	N-methyl-2-pyrrolidinone
CV	Cyclic voltammetry
GCD	Galvanostatic charge/discharge
EIS	Electrochemical impedance spectroscopy

Chapter I

Introduction

1.1 Supercapacitor as an energy storage system

Fossil fuels, the primary global energy source, contribute to approximately 80% of worldwide energy consumption. Despite their crucial role, the availability of fossil fuels is falling over time due to factors such as increasing global population and advancing economies, leading to a rising demand for energy. Furthermore, fossil fuels significantly contribute to climate change by releasing greenhouse gases during combustion. One potential solution is transitioning to renewable energy sources to decrease and mitigate the reliance on fossil fuel resources. The cost-effectiveness and efficiency of renewable energy sources are on the rise, offering a sustainable means to fulfill our energy requirements [1]. However, renewable energy resources like solar and wind systems are intermittent in nature. Given the intermittent nature of this type of energy, finding sustainable energy storage solutions is crucial. There are various forms of energy storage, including thermal energy storage, chemical energy storage, mechanical energy storage, compressed air, and hydro energy storage. Among these options, batteries, and supercapacitors, utilizing electrochemical energy storage, are the most popular due to their rapid response time, long cycle life, and compact design [2,3]. These systems store energy in the form of chemical energy, which is converted into electrical energy when the device is discharged. Electrochemical energy storage offers numerous advantages, including high energy density, fast charging/discharging capabilities (ideal for on-demand power needs), and a long lifespan that makes them a cost-effective investment lasting for many years. Additionally, their recyclability contributes to environmental friendliness. In summary, supercapacitors and batteries prove to be efficient energy storage solutions, reducing environmental impacts [4,5].

Batteries boast impressive energy density, allowing them to store substantial energy, making them ideal for electric cars and portable electronics. Nonetheless, they struggle to deliver a surge of power quickly due to low power density, and safety issues arise when operating at high temperatures. Consequently, they are less suited for applications requiring high power density, and are expensive [6]. On the other hand, supercapacitors possess a high-power density and are suitable for high-performance applications such as high-power tools. However, their energy density is modest, limiting the amount of energy they can store compared to batteries. Consequently, they are less fitting for applications where weight constraints are a significant factor [7,8]. Moreover, supercapacitors possess rapid charge and discharge, prolonged cyclic stability (~10^5 cycles), and noteworthy high-power density [9]. Their exceptional storage

efficiency positions supercapacitors as key players in the realm of energy storage systems. Commonly known as electrochemical capacitors or ultracapacitors, they have been the subject of numerous research studies due to their remarkable properties and potential applications across diverse fields. As advanced energy storage there is a dedicated pursuit to boost their energy density to make them suitable for wide variety of the applications [10].

1.2 Historical background for the supercapacitors

Historically, supercapacitors have undergone extensive investigation owing to their ability to provide exceptional features like high power density, rapid charge/discharge capabilities, long cycle life stability, and high reversibility[11]. The first time, Helmholtz explained the electrochemical double-layer capacitor (EDLC) concept was in 1853. Later, in 1957, the first patent was granted to Becker at General Electric Corporation Limited for the structure of a double layer capacitor with porous carbon material [12]. In 1962, Standard Oil Company, Cleveland, Ohio granted a patent on an energy storage system with the electrode used as a porous carbon material. In this case, the interface of EDLC behaves like an electrochemical capacitor and exhibits maximum specific capacitance. First time in 1971, Nippon Electric Company fabricated a double-layer capacitor commercially in the name of a supercapacitor. Since then, industrialization and modernization of the supercapacitor and its expansion of new technologies have originated. In 1978, Panasonic company has been advanced and used for energy storage applications. In 1982, metal oxide material was used for high energy density capacitor fabrication, and has been advanced by the Pinnacle Research Institute and labeled as PRI Ultracapacitors. Later, Conway et al. developed a RuO_2 electrode material for supercapacitors that exhibited lower internal resistance and maximum specific capacitance and which showed significant contributions in the 1970 and 1980 centuries[13]. In 1992, the Energy Department, US reported hybrid vehicles with great contribution by Maxwell using Ultracapacitors. Nowadays, the manufacturing of supercapacitors has been reported by various number of industries globally. In America and Japan, various types of EDLC and its components have been developed by industries such as Panasonic, NEC, Cooper, ELNA, etc. and commercialization and usage of supercapacitors have been radically increased due to the exceptional properties of supercapacitors and their multiple applications. Supercapacitors are used as electric energy storage resources in the field of transportation such as automobiles, drones, hybrid electric vehicle applications, and energy conversion systems[14–16].

1.3 Classification of supercapacitors based on the materials used and working principle.

The classification of electrode materials in supercapacitors is based on their energy storage mechanisms, dividing them into three types: EDLCs, pseudocapacitive, and hybrid capacitors. In Fig.1.1, we show the different types of supercapacitors, as well as the typical electrode materials used in each of the types.

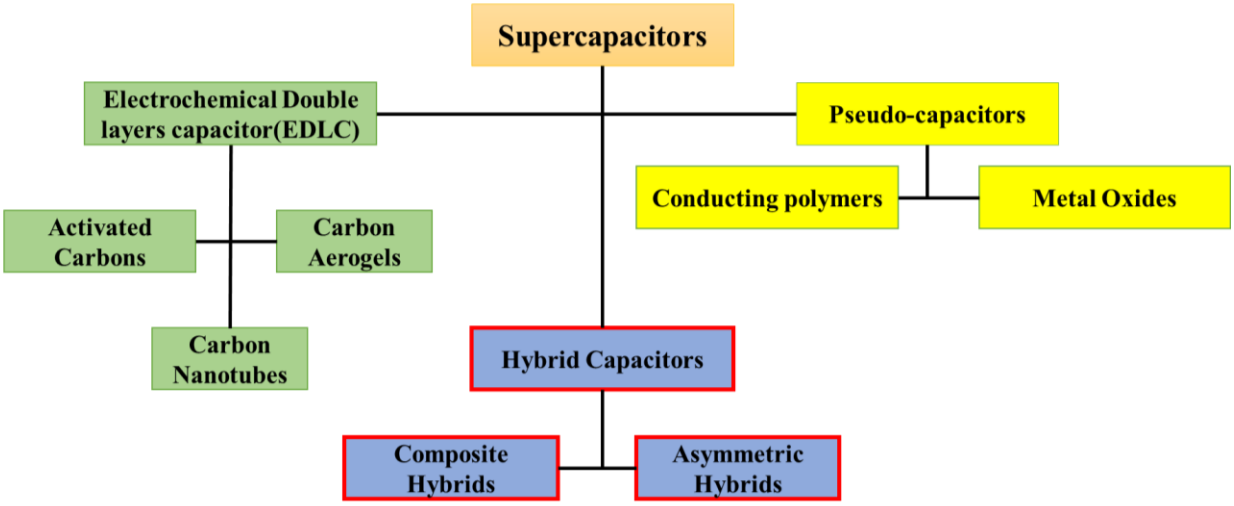

Figure 1.1 Classification of supercapacitors based on working mechanism.

As compared to conventional capacitors, EDLCs can store a hefty quantity of charge due to the large surface area of the electrode, at the electrode-electrolyte interface. The excellent electrical conductivity and the atomic distance between the electrodes of EDLCs reduce the internal resistance. In addition, the electrolyte provides good wettability, which promotes ion mobility, thereby improving specific capacitance[49]. In EDLCs, the charge is stored by forming double layers at the interface, this phenomenon was introduced by Von Helmholtz in the 19th century. During the formation of the EDL, the electrode surface is coated with a layer of ions at the electrode surface and a layer of counter-ions are present in the electrolyte. Helmholtz's EDL formation is shown in Fig.1.2 (a). A conventional capacitor is analogous to this model with the distance between parallel plates referred to as d, which approximates the radius of an ion. Chapman and Gouy modified the Helmholtz model by assuming a continuous distribution of ions in the electrolyte(collective effects of ion diffusion and electromigration) [50]. This is referred to as the 'diffuse layer' as shown in Fig.1.2 (b). A new model that combined Helmholtz's and Gouy-Chapman's models was proposed by Stern in 1924. An inner region layer is formed called a stern layer and the outer region is called a diffuse layer, as shown in Fig.1.2(c). In the inner region of the electrode, there is a layer of very strong adsorbed ions, which is why it is called a compact layer. There are two types of ions in the stern layer: those that are specifically adsorbed and those that are not specifically adsorbed. There are two types

of adsorbed ions, namely outer Helmholtz planes (OHP) and inner Helmholtz planes (IHP). Defining the Gouy-Chapman model is the second region known as the diffuse region [51]. In EDLC, electrode materials are usually porous carbon, and the electrochemical behavior is more complex at the surface of porous electrodes than at planar surfaces. There are a few factors that will limit ion transportation in these electrodes, such as rugged mass transfer paths, ohmic resistances of electrodes, space constraints in the pores, and wetting actions on the superficial of the pores [52]. It is possible to achieve high cyclic stability in EDLCs since there is no chemical reaction between electrolyte and electrode.

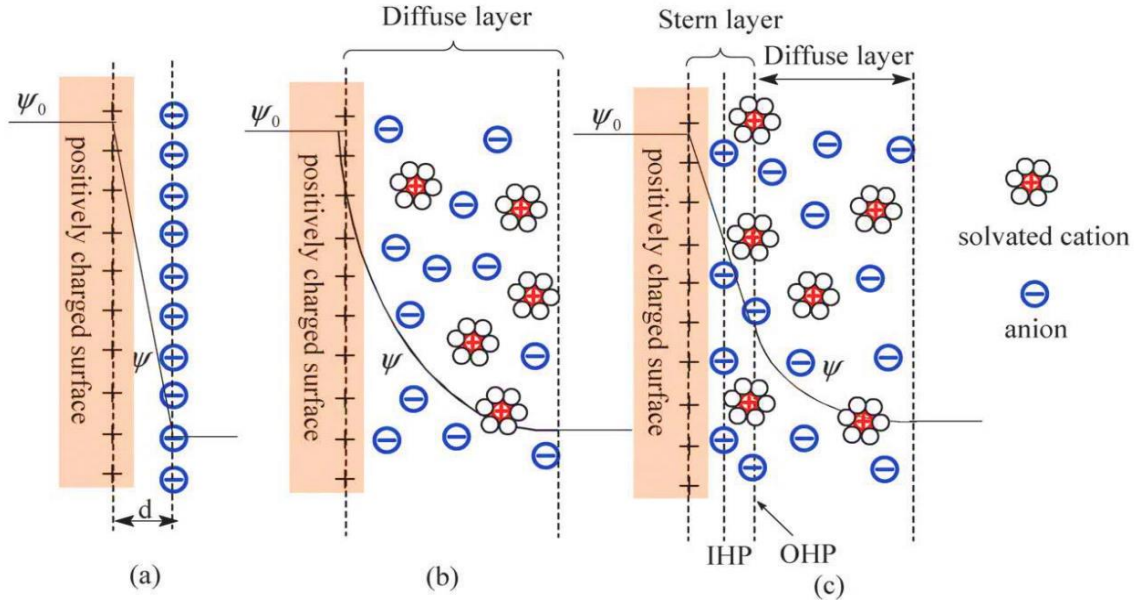

Figure 1.2 Mechanism of the electrical double layer (EDL) corresponding to (a) the Helmholtz model, (b) the modified Gouy-Chapman type, and (c) the Stern model.

The second category of capacitors, relying on an electrochemical storage mechanism, involves pseudocapacitive materials. These materials store charge through oxidation/reduction reactions occurring at the interface between the electrode and electrolyte. Ions from the electrolyte actively participate in these faradic reactions, facilitating the storage of charge on the electrolyte's surface[19]. The combination of surface absorption and faradic reactions enhances the overall charge storage capacity. Notably, conductive polymers and metal oxides within this category have attracted considerable attention due to their heightened specific capacitance. Conductive polymers stand out as a budget-friendly alternative boasting heightened specific capacitance, flexibility, improved electrical conductivity, and eco-friendliness. These characteristics render electrodes built with conductive polymers highly suitable for crafting lightweight, flexible, and environmentally friendly supercapacitors. Several conducting polymers have attracted substantial interest as electrodes for supercapacitors, including

polypyrrole (PPy), polyaniline (PANI), and poly 3,4-ethylenedioxythiophene, distinguish themselves for their notable characteristics, such as high specific capacitance, excellent electrical conductivity, and cost-effectiveness in comparison to other conducting polymers [29,30]. Another frequently utilized class of pseudocapacitive materials includes electrodes comprised of metal oxides. Thorough research is dedicated to these materials due to their notable features, encompassing high specific capacitance, compatibility with aqueous electrolytes, a wide range of available materials, and chemical stability. Ruthenium oxide (RuO_2), Manganese oxide (MnO_2), Cobalt oxide (Co_3O_4), and Nickel oxide (NiO) stand out as frequently utilized metal oxides in supercapacitors [31]. Researchers have been working on improving metal oxide electrodes for the last few years by selecting materials with a higher specific capacitance, a longer cycle life, and greater electrochemical stability [33]. Metal oxides show superior potential, primarily attributed to their hydrous form, resulting in higher capacitance compared to conducting polymers or carbon-based materials, as illustrated in Fig.1.3. Interactions between electrodes and electrolytes are affected by reversible redox reactions. Nevertheless, in order to overcome the inadequate electrical conductivity of these materials, they are frequently amalgamated with carbon materials. When electrodes made from carbon and pseudocapacitive materials are utilized, both EDLC and pseudocapacitor behavior can be observed. The resulting composites not only exhibit enhanced specific capacitance but also demonstrate improved kinetics at higher currents.[37,38].

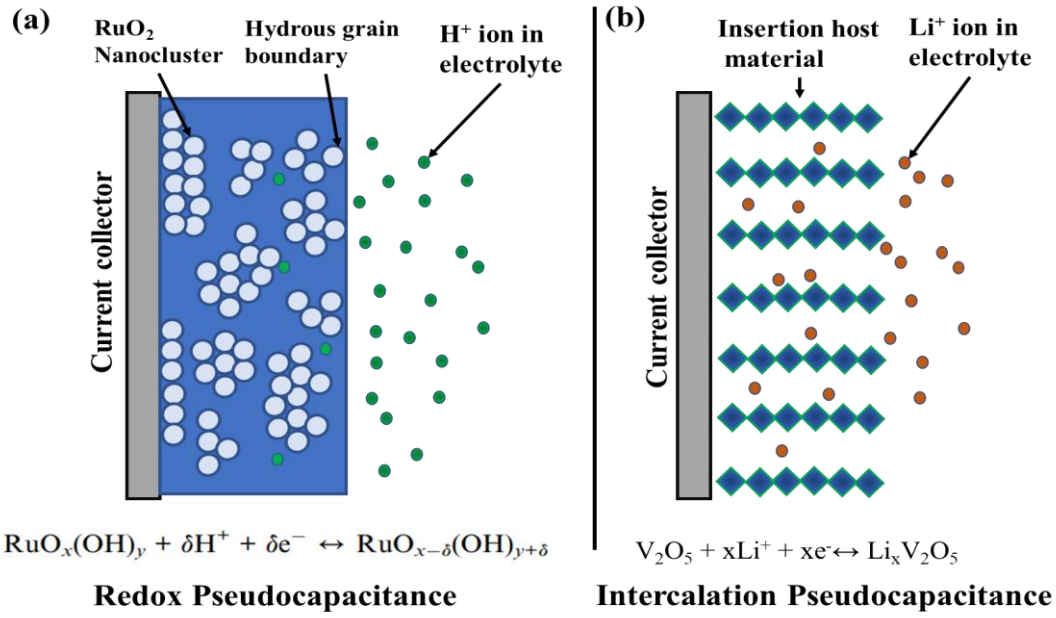

Figure 1.3. Different types of reversible redox mechanisms that give rise to charge storage: (a)redox reaction, and (b) intercalation pseudocapacitance.

The third category of capacitors is known as hybrid capacitors. True to their name, they employ both EDLC-type and pseudocapacitive electrode materials. In hybrid capacitors, charge storage occurs through a combination of electrostatic and electrochemical processes, merging the characteristics of EDLCs and pseudocapacitive charge storage [20].These capacitors achieve a harmonious equilibrium between high energy density and power density. Moreover, hybrid capacitors demonstrate extended cyclic life and enhanced temperature stability.

1.3.1 Classification based on the electrolyte used

Supercapacitors are categorized into three groups depending on the electrolyte utilized. Aqueous and organic electrolyte-based supercapacitors have garnered more extensive research attention compared to solid-state electrolyte supercapacitors, primarily due to cost considerations and challenges associated with ion mobility. Within these electrolyte options, aqueous electrolytes stand out for their cost-effectiveness, environmental friendliness and ease of handling. This uncomplicatedness streamlines the fabrication and assembly processes when compared to the use of organic electrolytes. Additionally, aqueous electrolytes exhibit a conductivity that is at least one order of magnitude higher than that of organic and ionic liquid electrolytes. Broadly, aqueous electrolytes are classified into acid, alkaline, and neutral solutions. In acidic electrolytes, the most extensively used electrolyte is H_2SO_4 due to its higher ionic conductivity (0.8 S cm^{-1}). On the other hand, alkaline electrolytes are also frequently used for supercapacitor investigation. Among several alkaline solutions, KOH is the most frequently used electrolyte in supercapacitors due to its high ionic conductivity (0.6 S cm^{-1} of 6 M NaOH at 25 ºC). Besides acidic and alkaline, neutral electrolytes containing salts such as NaCl, LiCl, and KCl, have also been investigated for SCs in the past decades due to less corrosion [21–23]. The second category, organic electrolytes is currently conquering the commercial market due to their high electrochemical potential window (EPW) (2.5 to 2.8 V). This will significantly enhance both energy and power densities compared to aqueous electrolytes. Nevertheless, certain concerns must be considered when employing organic electrolytes in supercapacitors. In comparison with aqueous electrolytes, they are generally more expensive, have lower ionic conductivity, are more volatile and flammable, and are more toxic [24,25]. In addition, organic electrolytes possess larger solvated ions, resulting in lower capacitance compared to aqueous electrolytes in supercapacitors [26]. The third type of supercapacitor based on the electrolyte used is a solid-state supercapacitor, which employs a solid-state electrolyte, typically made of polymers, ceramics, or a combination thereof. Ion movement occurs through a solid crystal lattice or a solid polymer matrix, mitigating the risks associated with electrolyte leakage and

flammability [45]. These supercapacitors showcase remarkable safety, elevated energy density, and prolonged cyclic life. However, their fabrication process is intricate, and improvements in ionic conductivity and cost are necessary to position them as a viable next-generation electrolyte material for energy storage devices [46-48].

1.4 Literature review

1.4.1 Electrode materials in EDLC

In EDLCs, electrodes are made up of a variety of carbonaceous materials, and a brief discussion of some of the materials is presented here. Various allotropes of carbon are promising materials for electrochemical double-layer capacitors (EDLCs) because of their high surface area, excellent electrical conductivity, and chemical stability. Among these carbon materials, activated carbon materials are widely studied as electrodes in the literature for EDLC-type supercapacitors due to their highly impressive specific surface area, well-established synthesis process, cost-effectiveness, customizable porosity, excellent polarization, high chemical stability, good electrical conductivity, environmental friendliness, and robust thermal and mechanical stabilities. The properties of activated carbon materials can be fine-tuned through synthesis methods, the choice of precursors, and the incorporation of heteroatoms into the porous carbon structure. Hence, the selection of suitable precursors and the application of the right synthesis method provide opportunities to customize and regulate both pore properties and material morphologies [28].

In addition to activated carbon, Carbon nanofibers (CNFs) have emerged as promising electrode materials for supercapacitors, owing to their unique combination of properties such as high surface area, flexibility, excellent electrical conductivity, and robust mechanical and thermal stabilities. CNFs offer numerous advantages, including large specific surface area, chemical stability, lightweight nature, good electrical conductivity, and environmental friendliness. Beyond their affordability and ease of manufacturing, CNFs exhibit several other benefits over alternative carbon materials. The electrospinning technique allows for the fabrication of carbon nanofibers with exceptional porosity, large specific surface areas, and a diverse range of functionalities by modifying the precursor composition [47, 48]. Furthermore, CNFs are capable of serving as free-standing electrodes without any conductive additives, binders, or current collectors. The presence of binders and additives tends to reduce the effective surface area and conductivity of the electrode, consequently diminishing its overall performance [53]. Owing to their impressive energy storage capabilities, electrospun carbon nanofiber membranes have garnered significant interest in energy storage applications [98,99].

Carbon nanomaterials graphene and carbon nanotubes has revolutionized the realm of nanomaterials for energy storage. Graphene, a two-dimensional material, features a porous structure that facilitates the intercalation of electrolyte ions with tunable interlayer spacing [57]. However, practical challenges arise, as the sheets tend to agglomerate due to weak Vander Waal forces, limiting electrolyte ion access to pores [63]. Various strategies, such as mechanical and electrochemical exfoliation, chemical vapor deposition, and the arc discharge methods were employed for graphene production [58]. Other carbon nanomaterials single-walled carbon nanotubes (SWCNT) made up of an individual graphene sheet with sp^2 hybridization, while multi-walled carbon nanotubes result from rolling up several sheets [64]. Carbon nanotubes (CNT) possess inherent properties that make them supreme materials for energy storage applications, including high ionic conductivity, lightweight nature, excellent electrical conductivity, chemical stability, and high aspect ratios [65].

Three-dimensional porous structures like carbon hydrogels and aerogels facilitate the diffusion of electrolyte ions, making them suitable electrodes for supercapacitors [67,68]. Hydroxy gels are essentially 3D structures that are cross-linked physically or chemically and have water adsorbent on them. While aerogels have a similar structure to hydrogels, they have an air-adsorbed network rather than water. Due to their porous network, aerogels exhibit low density (0.004–0.500 g cm^{-3}) and high surface area. Carbon gels can be categorized according to their source of carbon: polymer-derived carbon gels, carbon nanotube-based gels, graphene-based gels, and biomass-derived gels[69]. Although carbonaceous electrode materials have a higher energy density than other electrode materials used in supercapacitors, they exhibit low specific capacitance due to the lack of faradaic reactions. In Table 1.1, we present a comparison of the electrochemical performances of different carbonaceous electrodes used in supercapacitors.

Table 1.1 Electrochemical performance comparison of various carbonaceous materials used as supercapacitor electrodes.

Material	Specific capacitance	Electrolyte	Reference
Activated carbon	368 F g^{-1} at 0.05 A g^{-1}	1 M H_2SO_4	Rufford et al. [71]
CNF	156 F g^{-1} at 0.5 A g^{-1}	6 M KOH	Mingjia et al [72]
ACNF	256 F g^{-1} at 0.2 A g^{-1}	6 M KOH	Chang et al [73]
Graphene aerogel	220 F g^{-1} at 1 A g^{-1}	6 M KOH	Tang et al. [72]
Carbon aerogel	110 F g^{-1} at 1 mV s^{-1}	6 M KOH	Li et al. [73]
Graphene	135 F g^{-1} at 20 mV s^{-1}	5.5 M KOH	Stoller et al. [74]
Activated carbon	330 F g^{-1} at 1 A g^{-1}	2 M KOH	Peng et al. [75]

1.4.2 Pseudocapacitive materials

Pseudocapacitive materials store charges through the exchange of ions between the electrolyte and electrode. The processes involved in charge storage include electron absorption, reduction-oxidation, and intercalation of ions. When a potential is applied to a pseudocapacitor, Faradaic reactions occur at the electrode-electrolyte interface, generating a current in the cell [78]. Due to Faradaic reactions, pseudocapacitors exhibit higher capacitance and energy density compared to EDLCs. Pseudocapacitive materials fall into categories such as conducting polymers and metal oxides. Conducting polymers (CPs) are commonly utilized as supercapacitor electrodes due to their advantages, including low electro-resistance (ER), cost-effectiveness, ease of synthesis, and superior capacitance and conductivity compared to carbonaceous electrode materials. In contrast to EDLCs, CPs have a larger surface area and store charges through redox reactions. As the polymer is oxidized, ions are transferred from the solution to the polymer support, and as the ions are resumed to the solution the polymer is reduced [78]. Compared to carbon materials, conducting polymers charge throughout the entire material rather than just on the surface. There is no efficient n-doped material for CPs, which has hindered them from reaching their potential. Furthermore, the oxidation and reduction reactions that occur in CPs lead to poor cyclic stability [79]. It is possible to overcome these drawbacks by making electrode composites with other materials. Common conducting polymers used in supercapacitors are polypyrrole(PPy), polyaniline (PANI), and poly-(3,4-ethylenedioxythiophene(PEDOT) [79]. Using electrodeposition techniques, produced nanowires of PANI with a specific capacitance of 775 F g^{-1} at 10 mV s^{-1} in 1 M H_2SO_4 [80]. In Table 1.2, different conducting polymer electrodes are compared in terms of their electrochemical performance.

Table 1.2 Electrochemical performance comparison for various Conducting polymers used as supercapacitor electrodes.

Material	Synthesis method	Specific capacitance	Reference
Polypyrrole	Electrodeposition	480 F g^{-1} at 10 mV s^{-1}	Fan et al. [81]
PANI fibers	Polymerization	160 F g^{-1} at 0.4 A g^{-1}	Zhang et al. [82]
PEDOT nanowires	Self-assembled micellar	667 mF cm^{-2} at 1 mA cm^{-2}	Dan et al. [83]
PANI nanowires	Polymerization	950 F g^{-1} at 1 A g^{-1}	Wang et al. [84]
RuO_2	Electrodeposited	650 F g^{-1} at 0.5 A g^{-1}	Patake et al.[89]
Co_3O_4 Xerogels	Sol-Gel	291 F g^{-1} at 1 A g^{-1}	Lin et al. [90]
NiOx	Electrochemical	277 F g^{-1} at 1 A g^{-1}	Nam et al. [91]

RuO_2	Spray pyrolysis	551 F g^{-1} at 5 mV s^{-1}	Gujar et al. [92]
Fe_2O_3 thin films	Chemical	178 F g^{-1} at 5 mV s^{-1}	Kula et al. [93]
V_2O_5 nano chains	Hydrothermal	631 F g^{-1} at 0.5 A g^{-1}	Umesh et al. [94]
Tin oxide	Electro-deposition	285 F g^{-1} at 10 mV s^{-1}	Rajendra et al. [95]
Manganese oxide	Chemical Route	145 F g^{-1} at 2 mV s^{-1}	Jiang et al. [96]
CoS_x	Chemical precipitation	475 F g^{-1} at 5 mA cm^{-2}	Tao et al. [104]
MoS_2	Hydrothermal	403 F g^{-1} at 1 mV s^{-1}	Ramad et al. [105]
Cobalt selenide	Solvothermal	238 F g^{-1} at 1A g^{-1}	Wang et al. [106]
VN	Ammonolysis	850 F g^{-1} at 1 A g^{-1}	Choi et al. [107]
TiN Microspheres	Ammonia reaction	133 F g^{-1} at 2 mV s^{-1}	Dong et al. [108]

Metal oxide electrodes store energy through redox processes and so have higher capacitance and are abundant in nature, easy to synthesize on a big scale, and inexpensive. When compared to carbonaceous electrodes and conducting polymers, metal oxide has a greater capacitance. Its ESR is also quite low when compared to other electrodes. Thus, research focused on various metal oxides such as RuO_2, MnO_2, V_2O_5, Fe_3O_4, Co_3O_4, SnO, TiO_2, NiOx, ZnO, and many more [85,86]. Thin sheets of RuO_2 electrode were made by cathodic electrodeposition onto a SnO_2 substrate, in 0.5 M H_2SO_4 solution, showed a specific capacitance of 269 F g^{-1} was reported by Pusawale et al[87]. A strong acid, such as sulfuric acid, is known to improve capacitance via increasing proton conductivity. However, most metal oxides other than RuO_2 broke down in acidic electrolytes like H_2SO_4 and were thus employed in milder electrolytes like potassium chloride. Liu et al., demonstrated that the MnO_2 generated mechanochemically displayed a specific capacitance of 416 F g^{-1} in aqueous KOH electrolyte at a scan rate of 1 mV s^{-1}[88]. Apart from manganese oxide, many other metal oxides, as previously noted, were investigated as supercapacitor electrodes, they were found to have low energy density and poor conductivity when compared to RuO_2. Because the majority of the oxides are broad bandgap semiconductors or insulators, they have low conductivity. The low conductivity of different transition metal oxides significantly restricts their practical use, particularly at high scan rates. As a result, research into cheaper and more efficient materials with superior conductivity and capacitance advanced. Other electrode materials, such as metal dichalcogenides, transition metal nitrides, and phosphides, were evaluated as supercapacitor electrodes in this respect, and are briefly described in the following section. Metal oxide synthesis method and the performance comparison are digested in Table 1.2.

Transition metal dichalcogenides (TMDs) are another type of pseudo capacitive electrode materials represented by the generic formulation MX_2, where M is the transition metal (V, Ta, Nb, Mo, W, Ti, Co, and so on) and X is the chalcogenide. Chalcogenides (S, Se, and Te) are frequently employed in a variety of applications because they produce stable binary compounds with transition metals. TMDs can be synthesized using a variety of top-down and bottom-up techniques such as mechanical exfoliation, solid-vapor deposition, thermal breakdown, and other methods [97]. MoS_2, WS_2, $MoSe_2$, WSe_2, and $MoTe_2$ are the most investigated materials among the many TMDs accessible [98]. TMDs have metallic characteristics when their orbitals are partly filled and semiconducting qualities when they are filled. When compared to chalcogen atoms, metal atoms have a significant effect on electronic characteristics [99]. These layered materials have outstanding electrochemical characteristics, allowing them to be employed in a variety of electrochemical applications. The electrical conductivity of transition metal selenides is higher than that of transition metal sulfides. TMDs have a huge surface area, numerous oxidation states, and variable interlayer spacing, making them ideal for supercapacitor applications. Although they have an enormous surface area, they are not as capable as supercapacitors due to weak intrinsic conductivity and TMD sheet self-restacking. [100]. Table 1.2 provides a quick comparison of the performance of several pseudocapacitive materials with metal oxides and conducting polymers. Several issues encountered with pseudocapacitive and carbonaceous electrode materials might be effectively addressed by the third type of supercapacitor.

1.4.3 Hybrid composite materials for supercapacitors

Hybrid capacitors combine the benefits of both EDLC and pseudocapacitors, resulting in better performance. Combining Faradaic and non-Faradaic processes is what makes them more efficient than the other two types. As a result, hybrid capacitors have higher energy density than EDLCs while overcoming the cyclic stability and pricing difficulties that plague pseudocapacitors. Composite electrodes store charges by combining EDLC and pseudocapacitive electrode materials, utilizing both chemical and physical charge storage methods. As a result, the characteristics of both types of electrodes are merged inside a single electrode. By producing a double layer and generating a high SSA backbone to attach the pseudocapacitive materials such as conducting polymers and metal oxides. By integrating pseudocapacitive materials that undergo redox processes, the whole performance of the composite electrode can be amplified [109]. According to Li et al., graphene-ZnO hybrids outperformed their counterparts in terms of electrochemical performance [110]. The ZnO rods

are placed among the layers of graphene sheets, avoiding sheet restacking. The synergistic impact of ZnO and graphene contributes to better electrochemical performance of the specific capacitance of is 156 F g^{-1} at 5 mV s^{-1}. Similarly, when carbon nanotubes are combined with polypyrrole, the composite outperforms the component materials. This is due to the carbon nanotube's structure, which allows the polymer to be covered evenly, allowing for 3D charge dispersion. Furthermore, the composite structure aids the polymer in overcoming the mechanical stress that occurs during ion entry and removal [111]. Table 1.3 lists a handful of the composites that have been documented in the literature.

Table 1.3 Different composite electrodes reported for supercapacitor applications.

Material	Synthesis method	Specific capacitance	Reference
Graphene-PPy	Polymerization	270 F g^{-1} at 0.5 A g^{-1}	Basnayake et al.[112]
RGO-Au	Electrodeposition	288 F g^{-1} at 0.7 A g^{-1}	Yu et al. [113]
CoS_x /CNT	Hydrothermal	1324 F g^{-1} at 1 A g^{-1}	Mao et al. [114]
SiC/ MnO_2	Chemical route	273 F g^{-1} at 10 mV s^{-1}	Kim et al. [115]
MWCNT@MnO_2@PPy	Chemical route	272.7 F g^{-1} at 1 A g^{-1}	Oliveira et al. [116]

1.4.4 Two Dimensional MXene based electrode materials for supercapacitor

Graphene stands out as the go-to carbon nanomaterial for energy storage, thanks to its remarkable properties. It not only serves independently but is also embedded in various other carbon materials to augment electrochemical performance. Beyond graphene, the emergence of MXene has brought about a transformative shift in the realm of nanomaterials utilized for energy storage. MXene's unique characteristics have contributed to its significant impact in advancing the field. Since Gogotsi and Barsoum discovered MXenes in 2011, they have gained much traction due to their immaculate properties [39]. These are produced by selectively removing 'A' layers from MAX phases that have a general formula of $M_{n+1}AX_n$. M is an early transition metal (Ti, Cr,V, Mn,Nb, and Mo), A is an element of group 13 or 14 (Al, Si, Ga,Ge, Sn and Pb), and X is either nitrogen or carbon[40]. To indicate its graphene-like morphology, the 2D material obtained after etching A layers from MAX phase was referred to as MXene. Two-dimensional MXenes have the formula $M_{n+1}X_nT_x$, where T_x is the functional groups (-O, -OH, -F) attached to M atoms from the etching process[41–43]. It possesses excellent mechanical properties and highly conductive material and incredibly versatile can be used in a diversity of composites and energy storage applications[44].Since then, several 2D materials have been broadly researched, including metal oxides/hydroxides, TMDs, MOFs, and

hexagonal boron nitride. In this regard, MXenes, a novel family of transition metal carbides and/or nitrides, were discovered and investigated for a variety of applications. They have acquired maximum relevance in the realm of energy storage due to the perfect features demonstrated by them due to their 2D form. While a brief introduction to MXenes is provided in Chapter 1, this section focuses on the synthesis methods used to create MXenes, as well as their characteristics and performance as supercapacitor electrodes.

1.4.5 Synthesis of MXenes and Delaminating

MXenes are synthesized from their precursor materials MAX phases, from the MAX phase, the A atom is etched with Hydrofluoric acid (HF) to generate the MXene. Thus, the solid concentrated MAX phase will be transformed into loosely assembled layers, resulting in Multi-layered (ML) MXenes, after exfoliation of ML-MXenes, resulting in few-layered MXenes[117]. X-ray diffraction (XRD) and energy-dispersive spectroscopy (EDS) can be used to validate the conversion of MAX phase to MXene. If MAX is completely converted to MXene, the XRD pattern will feature (000l) peaks and all supplementary peaks will be nonexistent or weak. The (000l) peak will be wide and downshifted to lower 2θ, suggesting that the c lattice parameter has increased. EDS will calculate the A: M ratio; if this ratio is insignificant, it signals full conversion. Only peaks corresponding to (000l) were found in the pattern for $Ti_3C_2T_x$ MXene [118]. Most MAX phase powder (carbide-based) is etched by treating it with HF solution(aqueous) for a specific time period. Further, centrifugation of the above solution followed by washing with DI water is done until the pH spreads a value above 6. MXene, an accordion-like structure akin to exfoliated graphite, is then obtained by filtering the solution. The layered structures are then ultrasonically treated to produce delaminated structures [119]. The development of the $M_{n+1}X_n$ phase from its MAX phase is represented by Equation 2.1.

$$M_{n+1}AX_n + 3HF \rightarrow AF_3 + 3/2H_2 + M_{n+1}X_n \quad \rightarrow 1.1$$

Equations 1.2 and 1.3 portray the surface functionalization of the $M_{n+1}X_n$ during the etching process due to the electrophilic character of the metal with components such as -F and -OH.

$$M_{n+1}X_n + 2H_2O \rightarrow M_{n+1}X_n(OH)_2 + H_2 \quad \rightarrow 1.2$$

$$M_{n+1}X_n + 2HF \rightarrow M_{n+1}X_nF_2 + H_2 \quad \rightarrow 1.3$$

Ball milling can lower the duration and concentrations of HF by reducing the size of MAX stages. The bond energies of M-A also influence the required time duration and concentration of HF [121]. Alhabeb et al. conducted extensive research on the influence of delamination

procedures on the creation of Ti_3C_2Tx. The HF acid reaction timings and concentration were altered, and research was conducted on this, with 10 wt.% HF solution was used for etching aluminum from Ti_3AlC_2 [122].Several methods were found on consume of in situ HF produced when a fluoride-acid salt was engaged as an etchant. To synthesize the etching agents, acids (HCl, H_2SO_4) and fluoride salts ($NaHF_2$, NH_4HF_2, and KHF_2) were combined in the appropriate quantities [123–125]. When NH_4HF_2 was utilized as the etching agent in the study published by Halim et al., the time duration necessary for the etching to complete with HF was less when compared with fluoride-acid salt. Liu et al. published a comprehensive study on the effect of several fluoride salts in HCl, like NaF, LiF, NH_4F, and KF, as etchants for Ti_3AlC_2 and Ti_2AlC. These phenomena of cation intercalation (Na^+, K^+, NH^{4+}, Mg^{2+}, and Al^{3+}) into the layers of MXene not only aid in the delamination of the MXene sheets but also increase the volumetric capacitance in supercapacitors [126]. Ghidiu et al. stated that the etching solution was a fluoride salt, LiF dissolved in 6M HCl. The Ti_3AlC_2 particles were gradually added to the salt-acid combination, and the blend mixture was kept at 40 ℃ for 45 hours then periodically rinsed with DI water and filtered. This residue was a clay form and may be rolled to form free-standing films or molded into diverse forms. It might also be used as an ink when diluted[127]. Further, to create a few-layered MXene sheets, intercalation and exfoliation techniques are required. Surface functionalization, number of layers, and crystallinity are entirely affected by the delaminating and etching processes. Ultrasonic-assisted dealumination is an innovative approach that enhances the synthesis process. When Ti_3C_2Tx is processed through ultrasonic treatment, it exhibits significantly higher charge–discharge capacities and Columbic efficiency. Ultrasonication is a primary tool for delaminating, separating, and exfoliating MXene sheets. It dramatically accelerates the process and produces a larger fraction of high-quality 2D sheets Delamination may be accomplished by ultrasonicating the MXene colloidal, but prolonged sonication will affect the lamellar structures [126]. Mashtalir et al., reported on the intercalation of hydrazine monohydrate (HM) dissolved in DMF into functionalized Ti_3C_2, followed by delamination by DMSO and urea [128]. The intercalating with HM/DMF led to an enhancement in the c-lattice parameter of f-Ti_3C_2.MXenes are negatively charged (hydrophilic) and hence may produce surfactant-free stable colloidal in water when delaminated, according to zeta potential tests. This phenomenon was adequately explained by the efficiency of several organic bases as delaminating agents. Tetramethylammonium hydroxide (TMAOH), dimethyl sulfoxide (DMSO), urea, choline hydroxide, n-butylamine, and hydrazine are common delaminating agents. As soon as the organic molecules have intercalated into the MXene multi-layers, gentle agitation or moderate ultra-sonication will cause delamination [129,130].

1.4.6 Physicochemical Properties of MXenes and Surface Chemistry of MXene

MXenes have proven to be beneficial in a wide range of applications, such as sensors, catalysts, energy storage, electromagnetic shielding, and many more because of their excellent metallic and electrical conductivity. In $Ti_3C_2T_x$ (MXene) T_x refers to surface functionality and x specifies the number of functionalities. As a result, surfaces include species that do not belong to the MAX phase. The negative energy generation of MXenes is caused by the tight connection between T_x groups and the M atoms [131]. Hope et al., proved that the Nuclear Magnetic Resonance (NMR) approach is appropriate for quantifying surface terminations on MXene $Ti_3C_2T_x$ [132]. Surfaces ended with -OH terminations have lowered work function, -O have enhanced work function, and -F terminations have moderate values depending on the type of material. MXenes have uses in a variety of industries due to their remarkable characteristics. MXenes' electrical characteristics are determined by their functional groups as well as composition. Transition metal nitrides and carbides have high chemical and thermal stability [133]. Li et al., first reported on the thermal stability of Ti_3C_2 MXene presented by using thermogravimetry and differential scanning calorimetry analyses to estimate the stability. Ti_3C_2 MXene remained stable up to 800℃ in the presence of Argon, though in the attendance of oxygen atmosphere, sections of the MXene were oxidized around a temperature of 200 ℃, creating nanocrystals equally dispersed on the surface of the sheets, and MXene sheets were oxidized around 1000 ℃[117]. The electrical conductivity of Ti_3C_2Tx was approximately 24000 S m^{-1}, whereas the electrical conductivity of Ti_3C_2Tx /PVA composite film was 22000 S m^{-1}. The incorporation of a polymer matrix into the MXenes layers has been found to improve electrical and mechanical characteristics[134]. Transparent thin films with optoelectronic capabilities were created by spraying colloidal suspensions of delaminated Ti_3C_2Tx. These characteristics were found to fluctuate with ion intercalations between the layers of Ti_3C_2Tx. MXene thin films may also be produced using spin coating or drop casting processes.

1.4.7 MXene composite performance as supercapacitor electrodes

MXenes have brilliant characteristics such as oxidation resistance, extreme hardness, hydrophilicity, a high melting point, the scope to accept a variety of intercalants, and thermal conductivity [135]. MXenes and related composites have been identified as capable aspirants for supercapacitors because of their well-defined geometry, huge surface areas, and layered architectures. There is more influence of electrochemical intercalation of cations like K^+, Na^+, Mg^{2+}, $NH^{4+}$and Al^{3+} on the charge storage ability of MXene (Ti_3C_2Tx) [126]. To achieve

intercalation of cations, MXene (Ti_3C_2Tx) was placed in different salt solutions. The fundamental process occurring in Ti_3C_2Tx with acidic electrolytes was disclosed by Hu et al. [136]. The charge/discharge activities occurring in MXene electrodes in various electrolytes comprising sulphate ion (H_2SO_4) were examined while charging or discharging the behaved like a pseudocapacitive nature in acidic electrolyte, H_2SO_4 hydronium ion reacts with the oxygen atoms existing on the surface of MXene. Li et al. found that Ti_3C_2Tx MXene has an excellent gravimetric capacitance reported as (245 F g^{-1}). A greater energy density of 27.4 Wh Kg^{-1} may be attained by intercalating cations such as K^+, making them the superlative competitor for supercapacitor electrodes. MXene that had been treated with salts was annealed at higher temperatures to alter the surface terminations and intercalate K^+ cations. In this case, increasing the inter-layer distances and the c-lattice parameter increases. Recorded a specific capacitance of 517 F g^{-1} at a current density of 1 A g^{-1}, even after 10000 cycles with a 99% capacitance retention[137]. Ghidiu et al., defined a clay-like MXene (Ti_3C_2Tx) that could be molded in any form. A wet clay-like paste was produced and rolled to produce flexible films. This facilitates intercalation, delamination, and filtering processes. The above tested for supercapacitor application in aqueous H_2SO_4 electrolyte, the electrode showed a specific capacitance of 245 F g^{-1} with 99% capacitance retention even after 10000 charge-discharge cycles. This better electrochemical performance because of clay-like MXene films was attributed to their simpler admission to the interlayer space because of pre-intercalated the small size of H^+ and water compared to other cations. A supercapacitor with a gel (PVA/H_3PO_4) electrolyte demonstrated a specific capacitance of 586.4 F cm^{-3} at a voltage scan rate of 10 mV s^{-1}. The Ti atoms participate in redox processes that account for pseudocapacitance in addition to the EDLC nature caused by the Graphene oxide layers. As a result, these composites have better electrochemical behaviour [127]. Wen et al., observed an upsurge in the c lattice parameter of MXene (Ti_3C_2Tx) nanosheets from 1.9 nm to 2.4 nm. The inclusion of a N(nitrogen) heteroatom into the MXene layers caused an increase in the c-lattice parameter. MXenes were processed in ammonia gas for 2 hours in a tube furnace with temperatures ranging from 200 to 300, 500, and 700 °C. In Ti_3C_2Tx, N atoms replace C atoms, increasing interlayer distances in MXenes layers[138]. The specific capacitance of MXenes improved by about 46% as compared with undoped MXene. In 1 M H_2SO_4 electrolyte, the electrodes showed a specific capacitance of 192 F g^{-1} and 82 F g^{-1} in 1 M $MgSO_4$ electrolyte. Levitt et al. developed an MXene Ti_3C_2/carbon fiber composite using an electrospinning process that demonstrated good supercapacitive behavior [139]. a few loaded MXene single-layered nanosheets were dispersed in N, N-dimethyl formamide (DMF) mixed with polyacrylonitrile

(PAN) and then loaded into a syringe. MXene/PAN nanofibers were synthesized by changing the voltage difference employed between the aluminum plate and the tip of the needle. MXene/CNF were synthesized by carbonizing these nanofibers. Fibers were carbonized at 800 degrees Celsius and showed a specific capacitance of 239 mF cm^{-2}.

Table 1.3 electrochemical performance comparison of various MXenes and its composites as supercapacitor electrodes.

Material	Specific capacitance	Electrolyte	Reference
Ti_3C_2Tx/PVA	528 F cm^{-3} at 2 mV s^{-1}	l M KOH	Ling et al. [134]
Ti_3C_2Tx/Ag	332 mF cm^{-2} at 2 mV s^{-1}	1 M Na_2SO_4	Li et al. [140]
Ti_3C_2T/RGO	154.3 F g^{-1} at 2 A g^{-1}	2 M KOH	Zhao et al. [141]
MnO_2/MXene	242 F g^{-1} at 1 A g^{-1}	1 M H_2SO_4	Wang et al. [142]

1.5 Motivation for the study and objectives

From the existing literature, only a limited of reports delve into the electrochemical properties of i) MXene-based composite electrodes, ii) flexible CNF-based ternary composite electrodes, and iii) nanostructured ternary hybrid electrodes for supercapacitors. Moreover, most composite materials in the literature are in bulk form. In this study, we predominantly utilized composite electrodes in the nanofibrous form. Nanofibrous electrodes exhibit notable features such as high surface area, excellent intra-fiber electrical conductivity, an effective electrode-electrolyte interface, and tunable porosity. The electrospinning technique, a widely adopted method, was employed to prepare nanofibrous composite electrodes in this thesis. The subsequent steps involved electro-deposition and ultrasound-assisted methods for the fabrication of binary and ternary composite electrodes tailored for supercapacitors. Within our investigation, MXene was introduced to well-studied metal oxide and conductive polymer composite electrodes to examine the impact on electrochemical performance, conductivity, flexibility, and wettability of the electrodes. The electrochemical performance of nanofibrous electrodes is contingent upon factors like surface area, micropore volume, mesopore volume, pyrolysis temperature, etc. Surprisingly, existing literature lacks a comprehensive summary detailing the impact of these parameters on the electrochemical performance of such electrodes. Therefore, beyond the preparation of diverse composite materials and evaluating their electrochemical efficacy, we have also developed an artificial neural network (ANN)-based model. The objective of this model is to forecast electrochemical performance by utilizing the inherent properties of the electrode material.

This study aims to synthesize binary and ternary composite materials and evaluate the electrochemical performance of the composite electrodes. The goal is to compare the performance of these composite electrodes with pristine electrodes, elucidating the impact of embedded materials on enhancing electrochemical performance. This will be achieved through a comprehensive investigation involving detailed structural and morphological characterization of the electrode materials. The following objectives have been identified for the present work to fulfill this overarching goal.

- Develop a ternary composite electrode for supercapacitors comprising ruthenium oxide, MXene, and carbon nanofibers as hosts without the use of binders, and evaluate its electrochemical performance.
- Synthesis of a flexible polyaniline (PANI) covered MXene embedded carbon nanofibrous electrode and evaluate its electrochemical performance as an electrode for supercapacitors.
- Fabrication of cobalt oxide coated hollow MXene/CNF (HMCNF) composite nanofibrous electrode for high-performance supercapacitor.
- Synthesis of cobalt-based metal-organic framework (MOF)/MXene/CNF composite and investigating its electrochemical performance as a supercapacitor electrode.
- Developing an ANN model to predict the capacitance of supercapacitors based on carbon nanofibrous membrane physicochemical properties.

1.6 Layout of the thesis

This thesis is organized into eight chapters, each serving a separate purpose.

Chapter 1 offers a concise overview of the thesis and its framework. Chapter 1 covers a brief introduction, the classification of supercapacitors, and a historical background. It delves into defining the scope of the thesis, accompanied by a literature review. The chapter also provides an overview of energy storage mechanisms, charge storage principles, synthesis methods, and material selection for supercapacitors.

In Chapter 2 we described the electrochemical performance of RuO_2/MXene/CNF ternary nanocomposites synthesized by electrospinning followed by carbonization. The electrochemical performance of this ternary electrode was investigated and compared with the binary composite electrode and other binary electrodes reported in the literature.

Chapter 3 demonstrates the preparation of a PANI/MXene/CNF-based electrode and investigates its electrochemical performance. The PANI-coated MXene/CNF nanocomposites

exhibit a core and shell structure with high electrical conductivity, demonstrating a significantly higher specific capacitance compared to pristine and binary composite electrodes. Moving to Chapter 4, it details the synthesis of Cobalt oxide on hollow MXene/CNF using electrodeposited methods. The ultrasound-assisted hydrolysis approach proves to be highly efficient in preparing hollow MXene/CNFs. This method shows promise for symmetrical supercapacitor applications, displaying excellent electrochemical performance.

Chapter 5 focuses on the synthesis and characterizations of Co-MOF/MXene/CNF nanocomposites using an electrospinning approach for supercapacitors. The combination of Co-MOF/MXene/CNF nanocomposite electrodes enhances the overall performance of supercapacitors, leveraging the high surface area and improved electrical conductivity of MOFs.

Chapter 6 introduces the development of an Artificial Neural Network (ANN) model tailored to predict the capacitance of supercapacitors by leveraging the physicochemical properties of carbon nanofibrous membranes. The resulting model demonstrates a close and accurate prediction of the electrochemical performance of carbon nanofibrous membranes.

Chapter 7 presents the overall conclusions drawn from the thesis's findings.

Finally, Chapter 8 explores future perspectives on supercapacitors, offering insights into potential advancements and developments in this field.

1.7 References

[1] P. Moriarty, D. Honnery, Review: Renewable Energy in an Increasingly Uncertain Future, Appl. Sci. 13 (2023). https://doi.org/10.3390/app13010388.

[2] M.R. Chakraborty, S. Dawn, P.K. Saha, J.B. Basu, T.S. Ustun, A Comparative Review on Energy Storage Systems and Their Application in Deregulated Systems, Batteries. 8 (2022). https://doi.org/10.3390/batteries8090124.

[3] J. Mitali, S. Dhinakaran, A.A. Mohamad, Energy storage systems: a review, Energy Storage Sav. 1 (2022) 166–216. https://doi.org/10.1016/j.enss.2022.07.002.

[4] T.M. Gür, Review of electrical energy storage technologies, materials and systems: Challenges and prospects for large-scale grid storage, Energy Environ. Sci. 11 (2018) 2696–2767. https://doi.org/10.1039/c8ee01419a.

[5] D. Lemian, F. Bode, Battery-Supercapacitor Energy Storage Systems for Electrical Vehicles: A Review, Energies. 15 (2022). https://doi.org/10.3390/en15155683.

[6] Y. Chen, Y. Kang, Y. Zhao, L. Wang, J. Liu, Y. Li, Z. Liang, X. He, X. Li, N. Tavajohi, B. Li, A review of lithium-ion battery safety concerns: The issues, strategies, and testing

standards, J. Energy Chem. 59 (2021) 83–99. https://doi.org/10.1016/j.jechem.2020.10.017.

[7] S. Chakraborty, M. N. L., Review—An Overview on Supercapacitors and Its Applications, J. Electrochem. Soc. 169 (2022) 020552. https://doi.org/10.1149/1945-7111/ac5306.

[8] K.C.S. Lakshmi, B. Vedhanarayanan, High-Performance Supercapacitors: A Comprehensive Review on Paradigm Shift of Conventional Energy Storage Devices, Batteries. 9 (2023). https://doi.org/10.3390/batteries9040202.

[9] A. Afif, S.M. Rahman, A. Tasfiah Azad, J. Zaini, M.A. Islam, A.K. Azad, Advanced materials and technologies for hybrid supercapacitors for energy storage – A review, J. Energy Storage. 25 (2019) 100852. https://doi.org/10.1016/j.est.2019.100852.

[10] G. Wang, L. Zhang, J. Zhang, A review of electrode materials for electrochemical supercapacitors, Chem. Soc. Rev. 41 (2012) 797–828. https://doi.org/10.1039/c1cs15060j.

[11] M.C. R. Ko¨tz, Principles and applications of electrochemical capacitors, Electrochim. Acta. 45 (2010) 2483–2498. https://doi.org/10.1057/9780230503014.

[12] H.I. Becker, Low voltage electrolytic capacitor patent, United State Pat. Off. (1954).

[13] B.E. Conway, Transition from "supercapacitor" to "battery" behavior in electrochemical energy storage, Proc. Int. Power Sources Symp. 138 (1991) 319–327. https://doi.org/10.1149/1.2085829.

[14] P. Sharma, T.S. Bhatti, A review on electrochemical double-layer capacitors, Energy Convers.Manag.51(2010)2901–2912. https://doi.org/10.1016/j.enconman.2010.06.031.

[15] J.R. Miller, Electrochemical capacitor thermal management issues at high-rate cycling, Electrochim.Acta.52(2006)1703–1708. https://doi.org/10.1016/j.electacta.2006.02.056.

[16] C.Z. Yuan, B. Gao, X.G. Zhang, Electrochemical capacitance of NiO/$Ru_{0.35}V_{0.65}O_2$ asymmetric electrochemical capacitor, J. Power Sources. 173 (2007) 606–612. https://doi.org/10.1016/j.jpowsour.2007.04.034.

[17] V.V.N. Obreja, On the performance of supercapacitors with electrodes based on carbon nanotubes and carbon activated material-A review, Phys. E Low-Dimensional Syst. Nanostructures. 40 (2008) 2596–2605. https://doi.org/10.1016/j.physe.2007.09.044.

[18] L. Luo, Y. Lan, Q. Zhang, J. Deng, L. Luo, Q. Zeng, H. Gao, W. Zhao, A review on biomass-derived activated carbon as electrode materials for energy storage supercapacitors,J.EnergyStorage.55(2022)105839. https://doi.org/10.1016/j.est.2022.105839.

[19] H.W. Park, K.C. Roh, Recent advances in and perspectives on pseudocapacitive materials for Supercapacitors–A review, J. Power Sources. 557 (2023) 232558. https://doi.org/10.1016/j.jpowsour.2022.232558.

[20] D.P. Chatterjee, A.K. Nandi, A review on the recent advances in hybrid supercapacitors, J. Mater. Chem. A. 9 (2021) 15880–15918. https://doi.org/10.1039/d1ta02505h.

[21] C. Zhao, W. Zheng, A review for aqueous electrochemical supercapacitors, Front. Energy Res. 3 (2015) 1–11. https://doi.org/10.3389/fenrg.2015.00023.

[22] X. Wu, H. Yang, M. Yu, J. Liu, S. Li, Design principles of high-voltage aqueous supercapacitors,Mater.TodayEnergy.21(2021). https://doi.org/10.1016/j.mtener.2021.100739.

[23] M.Z. Iqbal, S. Zakar, S.S. Haider, Role of aqueous electrolytes on the performance of electrochemical energy storage device, J. Electroanal. Chem. 858 (2020) 113793. https://doi.org/10.1016/j.jelechem.2019.113793.

[24] T.S. Bhat, P.S. Patil, R.B. Rakhi, Recent trends in electrolytes for supercapacitors, J. Energy Storage. 50 (2022) 104222. https://doi.org/10.1016/j.est.2022.104222.

[25] C. Zhong, Y. Deng, W. Hu, J. Qiao, L. Zhang, J. Zhang, A review of electrolyte materials and compositions for electrochemical supercapacitors, Chem. Soc. Rev. 44 (2015) 7484–7539. https://doi.org/10.1039/c5cs00303b.

[26] F. Béguin, V. Presser, A. Balducci, E. Frackowiak, Carbons and electrolytes for advancedsupercapacitors,Adv.Mater.26(2014)2219–2251. https://doi.org/10.1002/adma.201304137.

[27] E. Frackowiak, Carbon materials for supercapacitor application, Phys. Chem. Chem. Phys. 9 (2007) 1774–1785. https://doi.org/10.1039/b618139m.

[28] L. Borchardt, M. Oschatz, S. Kaskel, Tailoring porosity in carbon materials for supercapacitorapplications,Mater.Horizons.1(2014)157–168. https://doi.org/10.1039/c3mh00112a.

[29] R. Ramya, R. Sivasubramanian, M. V. Sangaranarayanan, Conducting polymers-based electrochemical supercapacitors - Progress and prospects, Electrochim. Acta. 101 (2013) 109–129. https://doi.org/10.1016/j.electacta.2012.09.116.

[30] Q. Meng, K. Cai, Y. Chen, L. Chen, Research progress on conducting polymer based supercapacitor electrode materials, Nano Energy. 36 (2017) 268–285. https://doi.org/10.1016/j.nanoen.2017.04.040.

[31] M.S. Yadav, Metal oxides nanostructure-based electrode materials for supercapacitor application, J. Nanoparticle Res. 22 (2020).https://doi.org/10.1007/s11051-020-051032.

[32] D. Nandi, V.B. Mohan, A.K. Bhowmick, D. Bhattacharyya, Metal/metal oxide decorated graphene synthesis and application as supercapacitor: a review, J. Mater. Sci. 55 (2020) 6375–6400. https://doi.org/10.1007/s10853-020-04475-z.

[33] Lichchhavi, A. Kanwade, P.M. Shirage, A review on synergy of transition metal oxide nanostructured materials: Effective and coherent choice for supercapacitor electrodes, J. Energy Storage. 55 (2022) 105692. https://doi.org/10.1016/j.est.2022.105692.

[34] J. Mei, T. Liao, G.A. Ayoko, J. Bell, Z. Sun, Cobalt oxide-based nanoarchitectures for electrochemical energy applications, Prog. Mater. Sci. 103 (2019) 596–677. https://doi.org/10.1016/j.pmatsci.2019.03.001.

[35] X. Hu, Y. Wang, Q. Wu, J. Li, Review of cobalt-based nanocomposites as electrode for supercapacitor application, Ionics (Kiel). 28 (2022) 989–1015. https://doi.org/10.1007/s11581-021-04319-z.

[36] M.Z. Iqbal, S.S. Haider, S. Zakar, M. Alzaid, A.M. Afzal, S. Aftab, Cobalt-oxide/carbon composites for asymmetric solid-state supercapacitors, Mater. Res. Bull. 131 (2020) 110974. https://doi.org/10.1016/j.materresbull.2020.110974.

[37] V.C. Lokhande, A.C. Lokhande, C.D. Lokhande, J.H. Kim, T. Ji, Supercapacitive composite metal oxide electrodes formed with carbon, metal oxides and conducting polymers,J.AlloysCompd.682(2016)381–403. https://doi.org/10.1016/j.jallcom.2016.04.242.

[38] P. Bijesh, V. Selvaraj, V. Andal, A review on synthesis and applications of nano metal Oxide/porous carbon composite, Mater. Today Proc. 55 (2021) 212–219. https://doi.org/10.1016/j.matpr.2021.06.163.

[39] Y. Gogotsi, P. Simon, True performance metrics in electrochemical energy storage, Science (80-.). 334 (2011) 917–918. https://doi.org/10.1126/science.1213003.

[40] Z.M. Sun, Progress in research and development on MAX phases: A family of layered ternary compounds, Int. Mater. Rev. 56 (2011) 143–166. https://doi.org/10.1179/1743280410Y.0000000001.

[41] A. Sohan, P. Banoth, M. Aleksandrova, A. Nirmala Grace, P. Kollu, Review on MXene synthesis, properties, and recent research exploring electrode architecture for supercapacitor applications, Int. J. Energy Res. 45 (2021) 19746–19771. https://doi.org/10.1002/er.7068.

[42] S. Panda, K. Deshmukh, S.K. Khadheer Pasha, J. Theerthagiri, S. Manickam, M.Y. Choi, MXene based emerging materials for supercapacitor applications: Recent advances, challenges, and future perspectives, Coord. Chem. Rev. 462 (2022) 214518.

https://doi.org/10.1016/j.ccr.2022.214518.

[43] M. Hu, H. Zhang, T. Hu, B. Fan, X. Wang, Z. Li, Emerging 2D MXenes for supercapacitors: Status, challenges and prospects, Chem. Soc. Rev. 49 (2020) 6666–6693. https://doi.org/10.1039/d0cs00175a.

[44] S. Venkateshalu, A.N. Grace, MXenes—A new class of 2D layered materials: Synthesis, properties, applications as supercapacitor electrode and beyond, Appl. Mater. Today. 18 (2020) 100509. https://doi.org/10.1016/j.apmt.2019.100509.

[45] X. Li, C. Wang, Y. Cao, G. Wang, Functional MXene Materials: Progress of Their Applications,Chem.-AnAsianJ.13(2018)2742–2757. https://doi.org/10.1002/asia.201800543.

[46] P. Lamba, P. Singh, P. Singh, P. Singh, Bharti, A. Kumar, M. Gupta, Y. Kumar, Recent advancements in supercapacitors based on different electrode materials: Classifications, synthesis methods and comparative performance, J. Energy Storage. 48 (2022) 103871. https://doi.org/10.1016/j.est.2021.103871.

[47] M.E. Sahin, F.; Blaabjerg, A. Sangwongwanich, A Review on Supercapacitor Materials and Developments,TurkishJ.Mater.5(2020)10–24. https://www.scienceliterature.com/index.php/tjom/article/view/10-24.

[48] J.C. Ellenbogen, Supercapacitors : A Brief Overview, (2006).

[49] L. Zhang, X.S. Zhao, Carbon-based materials as supercapacitor electrodes, Chem. Soc. Rev. 38 (2009) 2520–2531. https://doi.org/10.1039/b813846j.

[50] L. Pilon, H. Wang, A. d'Entremont, Recent Advances in Continuum Modeling of Interfacial and Transport Phenomena in Electric Double Layer Capacitors, J. Electrochem. Soc. 162 (2015) A5158–A5178. https://doi.org/10.1149/2.0211505jes.

[51] M.S. Uddin, H. Tanaya Das, T. Maiyalagan, P. Elumalai, Influence of designed electrode surfaces on double layer capacitance in aqueous electrolyte: Insights from standard models, Appl. Surf. Sci. 449 (2018) 445–453. https://doi.org/10.1016/j.apsusc.2017.12.088.

[52] P. Sharma, V. Kumar, Investigation of the behaviour of supercapacitors using theoretical models, Phys. B Condens. Matter. 619 (2021) 413212. https://doi.org/10.1016/j.physb.2021.413212.

[53] A. González, E. Goikolea, J.A. Barrena, R. Mysyk, Review on supercapacitors: Technologies and materials, Renew. Sustain. Energy Rev. 58 (2016) 1189–1206. https://doi.org/10.1016/j.rser.2015.12.249.

[54] C. Young, H.T. Chen, Supercapacitor application of a three-dimensional carbon sphere–

intercalated porous carbon fabricated using a hard template and a biomass material, Diam. Relat. Mater. 130 (2022) 109528. https://doi.org/10.1016/j.diamond.2022.109528.

[55] M. Karnan, K. Subramani, N. Sudhan, N. Ilayaraja, M. Sathish, Aloe vera Derived Activated High-Surface-Area Carbon for Flexible and High-Energy Supercapacitors, ACSAppl.Mater.Interfaces.8(2016)35191–35202. https://doi.org/10.1021/acsami.6b10704.

[56] J. Gamby, P.L. Taberna, P. Simon, J.F. Fauvarque, M. Chesneau, Studies and characterisations of various activated carbons used for carbon/carbon supercapacitors, J. Power Sources. 101 (2001) 109–116.https://doi.org/10.1016/S0378-7753(01)007078.

[57] K. S. Novoselov et al, Electric Field Effect in Atomically Thin Carbon Films, 306 (2016) 666–669.

[58] M.S.A. Bhuyan, M.N. Uddin, M.M. Islam, F.A. Bipasha, S.S. Hossain, Synthesis of graphene, Int. Nano Lett. 6 (2016) 65–83. https://doi.org/10.1007/s40089-015-0176-1.

[59] Q. Ke, Y. Liu, H. Liu, Y. Zhang, Y. Hu, J. Wang, Surfactant-modified chemically reduced graphene oxide for electrochemical supercapacitors, RSC Adv. 4 (2014) 26398–26406. https://doi.org/10.1039/c4ra03826f.

[60] A.A. Balandin, S. Ghosh, W. Bao, I. Calizo, D. Teweldebrhan, F. Miao, C.N. Lau, Superior thermal conductivity of single-layer graphene, Nano Lett. 8 (2008) 902–907. https://doi.org/10.1021/nl0731872.

[61] K.I. Bolotin, K.J. Sikes, Z. Jiang, M. Klima, G. Fudenberg, J. Hone, P. Kim, H.L. Stormer, Ultrahigh electron mobility in suspended graphene, Solid State Commun. 146 (2008) 351–355. https://doi.org/10.1016/j.ssc.2008.02.024.

[62] Y. Obeng, P. Srinivasan, Graphene: Is it the future for semiconductors? An overview of the material, devices, and applications, Electrochem. Soc. Interface. 20 (2011) 47–52. https://doi.org/10.1149/2.F05111if.

[63] R.S. Dey, H.A. Hjuler, Q. Chi, Approaching the theoretical capacitance of graphene through copper foam integrated three-dimensional graphene networks, J. Mater. Chem. A. 3 (2015) 6324–6329. https://doi.org/10.1039/c5ta01112d.

[64] A. Aqel, K.M.M.A. El-Nour, R.A.A. Ammar, A. Al-Warthan, Carbon nanotubes, science and technology part (I) structure, synthesis and characterisation, Arab. J. Chem. 5 (2012) 1–23. https://doi.org/10.1016/j.arabjc.2010.08.022.

[65] G. Lota, K. Fic, E. Frackowiak, Carbon nanotubes and their composites in electrochemical applications, Energy Environ. Sci. 4 (2011) 1592–1605.

https://doi.org/10.1039/c0ee00470g.

[66] M. Jayalakshmi, K. Balasubramanian, Simple capacitors to supercapacitors - An overview, Int. J. Electrochem. Sci. 3 (2008) 1196–1217. https://doi.org/10.1016/s1452-3981(23)15517-9.

[67] P.R. Burkholder, Microbiological studies on materials which potentiate oral vitamin B12 therapy in addisonian anemia, Arch. Biochem. Biophys. 39 (1952) 322–332. https://doi.org/10.1016/0003-9861(52)90343-3.

[68] X. Yan, X. Li, Z. Yan, S. Komarneni, for Supercapacitors, Appl. Surf. Sci. 21 (2014) 1933–1938. http://dx.doi.org/10.1016/j.apsusc.2014.04.160.

[69] X.L. Wu, A.W. Xu, Carbonaceous hydrogels and aerogels for supercapacitors, J. Mater. Chem. A. 2 (2014) 4852–4864. https://doi.org/10.1039/c3ta13929h.

[70] M.A. Riaz, P. Hadi, I.H. Abidi, A. Tyagi, X. Ou, Z. Luo, Recyclable 3D graphene aerogel with bimodal pore structure for ultrafast and selective oil sorption from water, RSC Adv. 7 (2017) 29722–29731. https://doi.org/10.1039/c7ra02886e.

[71] T.E. Rufford, D. Hulicova-Jurcakova, Z. Zhu, G.Q. Lu, Nanoporous carbon electrode from waste coffee beans for high performance supercapacitors, Electrochem. Commun. 10 (2008) 1594–1597. https://doi.org/10.1016/j.elecom.2008.08.022.

[72] X.N. Tang, C.Z. Liu, X.R. Chen, Y.Q. Deng, X.H. Chen, J.J. Shao, Q.H. Yang, Graphene aerogel derived by purification-free graphite oxide for high performance supercapacitor electrodes, Carbon N. Y. 146 (2019) 147–154. https://doi.org/10.1016/j.carbon.2019.01.096.

[73] J. Li, X. Wang, Q. Huang, S. Gamboa, P.J. Sebastian, Studies on preparation and performances of carbon aerogel electrodes for the application of supercapacitor, J. Power Sources. 158 (2006) 784–788. https://doi.org/10.1016/j.jpowsour.2005.09.045.

[74] M.D. Stoller, S. Park, Y. Zhu, J. An, R.S. Ruoff, Graphene-Based Ultracapacitors, Nano Lett. 8 (2008) 3498–3502.

[75] C. Peng, X. Bin Yan, R.T. Wang, J.W. Lang, Y.J. Ou, Q.J. Xue, Promising activated carbons derived from waste tea-leaves and their application in high performance supercapacitors electrodes, Electrochim. Acta. 87 (2013) 401–408. https://doi.org/10.1016/j.electacta.2012.09.082.

[76] M. Zhi, S. Liu, Z. Hong, N. Wu, Electrospun activated carbon nanofibers for supercapacitorelectrodes,RSCAdv.4(2014)43619–43623. https://doi.org/10.1039/c4ra05512h.

[77] Z. Yang, W. Zhao, Y. Niu, Y. Zhang, L. Wang, W. Zhang, X. Xiang, Q. Li, Direct

spinning of high-performance graphene fiber supercapacitor with a three-ply core-sheath structure, Carbon N. Y. 132 (2018) 241–248. https://doi.org/10.1016/j.carbon.2018.02.041.

[78] Z.S. Iro, C. Subramani, S.S. Dash, A brief review on electrode materials for supercapacitor, Int. J. Electrochem. Sci. 11 (2016) 10628–10643. https://doi.org/10.20964/2016.12.50.

[79] E. Frackowiak, V. Khomenko, K. Jurewicz, K. Lota, F. Béguin, Supercapacitors based on conducting polymers/nanotubes composites, J. Power Sources. 153 (2006) 413–418. https://doi.org/10.1016/j.jpowsour.2005.05.030.

[80] V. Gupta, N. Miura, High performance electrochemical supercapacitor from electrochemically synthesized nanostructured polyaniline, Mater. Lett. 60 (2006) 1466–1469. https://doi.org/10.1016/j.matlet.2005.11.047.

[81] L.Z. Fan, J. Maier, High-performance polypyrrole electrode materials for redox supercapacitors, Electrochem. Commun. 8 (2006) 937–940. https://doi.org/10.1016/j.elecom.2006.03.035.

[82] H. Zhang, Q. Zhao, S. Zhou, N. Liu, X. Wang, J. Li, F. Wang, Aqueous dispersed conducting polyaniline nanofibers: Promising high specific capacity electrode materials for supercapacitor, J. Power Sources. 196 (2011) 10484–10489. https://doi.org/10.1016/j.jpowsour.2011.08.066.

[83] D. Ni, Y. Chen, H. Song, C. Liu, X. Yang, K. Cai, Free-standing and highly conductive PEDOT nanowire films for high-performance all-solid-state supercapacitors, J. Mater. Chem. A. 7 (2019) 1323–1333. https://doi.org/10.1039/c8ta08814d.

[84] K. Wang, H. Wu, Y. Meng, Z. Wei, Conducting polymer nanowire arrays for high performance supercapacitors, Small. 10 (2014) 14–31. https://doi.org/10.1002/smll.201301991.

[85] C. An, Y. Zhang, H. Guo, Y. Wang, Metal oxide-based supercapacitors: progress and prospectives,Nanoscale Adv. 1 (2019) 4644–4658. https://doi.org/10.1039/c9na00543a.

[86] M. Guan, Q. Wang, X. Zhang, J. Bao, X. Gong, Y. Liu, Two-Dimensional Transition Metal Oxide and Hydroxide-Based Hierarchical Architectures for Advanced SupercapacitorMaterials,Front.Chem.8(2020)1–14. https://doi.org/10.3389/fchem.2020.00390.

[87] S.N. Pusawale, P.S. Jadhav, Effect of surface treatments on supercapacitive performance Of SnO_2-RuO_2 composite thin films, Mater. Today Proc. 18 (2019) 2848–2858. https://doi.org/10.1016/j.matpr.2019.07.152.

[88] K. yu LIU, Y. ZHANG, W. ZHANG, H. ZHENG, G. SU, Charge-discharge process of MnO2 supercapacitor, Trans. Nonferrous Met. Soc. China (English Ed. 17 (2007) 649–653. https://doi.org/10.1016/S1003-6326(07)60150-2.

[89] V.D. Patake, C.D. Lokhande, O.S. Joo, Electrodeposited ruthenium oxide thin films for supercapacitor: Effect of surface treatments, Appl. Surf. Sci. 255 (2009) 4192–4196. https://doi.org/10.1016/j.apsusc.2008.11.005.

[90] C. Lin, J.A. Ritter, B.N. Popov, Characterization of Sol-Gel-Derived Cobalt Oxide Xerogels as Electrochemical Capacitors, J. Electrochem. Soc. 145 (1998) 4097–4103. https://doi.org/10.1149/1.1838920.

[91] K.-W. Nam, K.-B. Kim, A Study of the Preparation of NiOx Electrode via Electrochemical Route for Supercapacitor Applications and Their Charge Storage Mechanism, J. Electrochem. Soc. 149 (2002) A346. https://doi.org/10.1149/1.1449951.

[92] T.P. Gujar, V.R. Shinde, C.D. Lokhande, W.Y. Kim, K.D. Jung, O.S. Joo, Spray deposited amorphous RuO_2 for an effective use in electrochemical supercapacitor, Electrochem.Commun.9(2007) 504–510. https://doi.org/10.1016/j.elecom.2006.10.017.

[93] P.M. Kulal, D.P. Dubal, C.D. Lokhande, V.J. Fulari, Chemical synthesis of Fe_2O_3 thin films for supercapacitor application, J. Alloys Compd. 509 (2011) 2567–2571. https://doi.org/10.1016/j.jallcom.2010.11.091.

[94] E. Umeshbabu, G. Ranga Rao, Vanadium pentoxide nanochains for high-performance electrochemical supercapacitors, J. Colloid Interface Sci. 472 (2016) 210–219. https://doi.org/10.1016/j.jcis.2016.03.050.

[95] K. Rajendra Prasad, N. Miura, Electrochemical synthesis and characterization of nanostructured tin oxide for electrochemical redox supercapacitors, Electrochem. Commun. 6 (2004) 849–852. https://doi.org/10.1016/j.elecom.2004.06.009.

[96] J. Jiang, A. Kucernak, Electrochemical supercapacitor material based on manganese oxide: Preparation and characterization, Electrochim. Acta. 47 (2002) 2381–2386. https://doi.org/10.1016/S0013-4686(02)00031-2.

[97] M. Pumera, Z. Sofer, A. Ambrosi, Layered transition metal dichalcogenides for electrochemical energy generation and storage, J. Mater. Chem. A. 2 (2014) 8981–8987. https://doi.org/10.1039/c4ta00652f.

[98] X. Chia, A.Y.S. Eng, A. Ambrosi, S.M. Tan, M. Pumera, Electrochemistry of Nanostructured Layered Transition-Metal Dichalcogenides, Chem. Rev. 115 (2015) 11941–11966. https://doi.org/10.1021/acs.chemrev.5b00287.

[99] M. Chhowalla, H.S. Shin, G. Eda, L.J. Li, K.P. Loh, H. Zhang, The chemistry of two-

dimensional layered transition metal dichalcogenide nanosheets, Nat. Chem. 5 (2013) 263–275. https://doi.org/10.1038/nchem.1589.

[100] J. Cherusseri, N. Choudhary, K. Sambath Kumar, Y. Jung, J. Thomas, Recent trends in transition metal dichalcogenide based supercapacitor electrodes, Nanoscale Horizons. 4 (2019) 840–858. https://doi.org/10.1039/c9nh00152b.

[101] K. Krishnamoorthy, G.K. Veerasubramani, P. Pazhamalai, S.J. Kim, Designing two dimensional nanoarchitectured MoS2 sheets grown on Mo foil as a binder free electrode for supercapacitors, Electrochim. Acta. 190 (2016) 305–312. https://doi.org/10.1016/j.electacta.2015.12.148.

[102] D. Chakravarty, D.J. Late, Microwave and hydrothermal syntheses of WSe2 micro/nanorods and their application in supercapacitors, RSC Adv. 5 (2015) 21700–21709. https://doi.org/10.1039/c4ra12599a.

[103] X. Xia, Y. Zhang, D. Chao, Q. Xiong, Z. Fan, X. Tong, J. Tu, H. Zhang, H.J. Fan, Tubular TiC fibre nanostructures as supercapacitor electrode materials with stable cycling life and wide-temperature performance, Energy Environ. Sci. 8 (2015) 1559–1568. https://doi.org/10.1039/c5ee00339c.

[104] F. Tao, Y.Q. Zhao, G.Q. Zhang, H.L. Li, Electrochemical characterization on cobalt sulfide for electrochemical supercapacitors, Electrochem. Commun. 9 (2007) 1282–1287. https://doi.org/10.1016/j.elecom.2006.11.022.

[105] A. Ramadoss, T. Kim, G.S. Kim, S.J. Kim, Enhanced activity of a hydrothermally synthesized mesoporous MoS_2 nanostructure for high performance supercapacitor applications, New J. Chem. 38 (2014) 2379–2385. https://doi.org/10.1039/c3nj01558k.

[106] Z. Wang, Q. Sha, F. Zhang, J. Pu, W. Zhang, Synthesis of polycrystalline cobalt selenide nanotubes and their catalytic and capacitive behaviors, CrystEngComm. 15 (2013) 5928–5934. https://doi.org/10.1039/c3ce40152a.

[107] D. Choi, P.N. Kumta, Chemically synthesized nanostructured VN for pseudocapacitor application,Electrochem.Solid-StateLett.8(2005)2–7. https://doi.org/10.1149/1.1951201.

[108] S. Dong, X. Chen, L. Gu, X. Zhou, H. Xu, H. Wang, Z. Liu, P. Han, J. Yao, L. Wang, G. Cui, L. Chen, Facile preparation of mesoporous titanium nitride microspheres for electrochemical energy storage, ACS Appl. Mater. Interfaces. 3 (2011) 93–98. https://doi.org/10.1021/am100951h.

[109] M. Vangari, T. Pryor, L. Jiang, Supercapacitors: Review of Materials and Fabrication Methods, J. Energy Eng. 139 (2013) 72–79. https://doi.org/10.1061/(asce)ey.1943-

7897.0000102.

[110] Z. Li, Z. Zhou, G. Yun, K. Shi, X. Lv, B. Yang, High-performance solid-state supercapacitors based on graphene-ZnO hybrid nanocomposites, Nanoscale Res. Lett. 8 (2013) 1–9. https://doi.org/10.1186/1556-276X-8-473.

[111] D.D. Potphode, P. Sivaraman, S.P. Mishra, M. Patri, Polyaniline/partially exfoliated multi-walled carbon nanotubes based nanocomposites for supercapacitors, Electrochim. Acta. 155 (2015) 402–410. https://doi.org/10.1016/j.electacta.2014.12.126.

[112] P. A. Basnayaka, M. K. Ram, L. Stefanakos, A. Kumar, Graphene/Polypyrrole Nanocomposite as Electrochemical Supercapacitor Electrode: Electrochemical Impedance Studies, Graphene. 02 (2013) 81–87. https://doi.org/10.4236/graphene.2013.22012.

[113] Z. Yu, S. Sun, M. Huang, Electrodeposition of Gold Nanoparticles on Electrochemically Reduced Graphene Oxide for High Performance Supercapacitor Electrode Materials, Int. J. Electrochem. Sci. 11 (2016) 3643–3650. https://doi.org/10.1016/s1452-3981(23)17426-8.

[114] M. Mao, L. Mei, L. Wu, Q. Li, M. Zhang, Facile synthesis of cobalt sulfide/carbon nanotube shell/core composites for high performance supercapacitors, RSC Adv. 4 (2014) 12050–12056. https://doi.org/10.1039/c4ra00485j.

[115] M. Kim, Y. Yoo, J. Kim, Synthesis of microsphere silicon carbide/nanoneedle manganese oxide composites and their electrochemical properties as supercapacitors, J. Power Sources. 265 (2014) 214–222. https://doi.org/10.1016/j.jpowsour.2014.04.132.

[116] A.H.P. De Oliveira, M.L.F. Nascimento, H.P. De Oliveira, Carbon Nanotube@MnO2@Polypyrrole composites: Chemical synthesis, characterization and application in supercapacitors, Mater. Res. 19 (2016) 1080–1087. https://doi.org/10.1590/1980-5373-MR-2016-0347.

[117] Z. Li, L. Wang, D. Sun, Y. Zhang, B. Liu, Q. Hu, A. Zhou, Synthesis and thermal stability of two-dimensional carbide MXene Ti_3C_2, Mater. Sci. Eng. B. 191 (2015) 33–40. https://doi.org/10.1016/j.mseb.2014.10.009.

[118] A. Vahidmohammadi, A. Hadjikhani, S. Shahbazmohamadi, M. Beidaghi, Two-Dimensional Vanadium Carbide (MXene) as a High-Capacity Cathode Material for Rechargeable Aluminum Batteries, ACS Nano. 11 (2017) 11135–11144. https://doi.org/10.1021/acsnano.7b05350.

[119] N.K. Chaudhari, H. Jin, B. Kim, D. San Baek, S.H. Joo, K. Lee, MXene: An emerging two-dimensional material for future energy conversion and storage applications, J.

Mater. Chem. A. 5 (2017) 24564–24579. https://doi.org/10.1039/c7ta09094c.

[120] M. Naguib, V.N. Mochalin, M.W. Barsoum, Y. Gogotsi, 25th anniversary article: MXenes: A new family of two-dimensional materials, Adv. Mater. 26 (2014) 992–1005. https://doi.org/10.1002/adma.201304138.

[121] F. Chang, C. Li, J. Yang, H. Tang, M. Xue, Synthesis of a new graphene-like transition metal carbide by de-intercalating Ti_3AlC_2, Mater. Lett. 109 (2013) 295–298. https://doi.org/10.1016/j.matlet.2013.07.102.

[122] M. Alhabeb, K. Maleski, B. Anasori, P. Lelyukh, L. Clark, S. Sin, Y. Gogotsi, Guidelines for Synthesis and Processing of Two-Dimensional Titanium Carbide (Ti3C2Tx MXene), Chem. Mater. 29 (2017) 7633–7644. https://doi.org/10.1021/acs.chemmater.7b02847.

[123] J. Halim, M.R. Lukatskaya, K.M. Cook, J. Lu, C.R. Smith, L.Å. Näslund, S.J. May, L. Hultman, Y. Gogotsi, P. Eklund, M.W. Barsoum, Transparent conductive two-dimensional titanium carbide epitaxial thin films, Chem. Mater. 26 (2014) 2374–2381. https://doi.org/10.1021/cm500641a.

[124] C. Shen, L. Wang, A. Zhou, B. Wang, X. Wang, W. Lian, Q. Hu, G. Qin, X. Liu, Synthesis and electrochemical properties of two-dimensional RGO/Ti_3C_2Tx nanocomposites, Nanomaterials. 8 (2018) 1–11. https://doi.org/10.3390/nano8020080.

[125] F. Liu, A. Zhou, J. Chen, J. Jia, W. Zhou, L. Wang, Q. Hu, Preparation of Ti_3C_2 and Ti_2C MXenes by fluoride salts etching and methane adsorptive properties, Appl. Surf. Sci. 416 (2017) 781–789. https://doi.org/10.1016/j.apsusc.2017.04.239.

[126] M.R. Lukatskaya, O. Mashtalir, C.E. Ren, Y. Dall'Agnese, P. Rozier, P.L. Taberna, M. Naguib, P. Simon, M.W. Barsoum, Y. Gogotsi, Cation intercalation and high volumetric capacitance of two-dimensional titanium carbide, Science (80-.). 341 (2013) 1502–1505. https://doi.org/10.1126/science.1241488.

[127] M. Ghidiu, M.R. Lukatskaya, M.Q. Zhao, Y. Gogotsi, M.W. Barsoum, Conductive two-dimensional titanium carbide "clay" with high volumetric capacitance, Nature. 516 (2015) 78–81. https://doi.org/10.1038/nature13970.

[128] O. Mashtalir, M. Naguib, V.N. Mochalin, Y. Dall'Agnese, M. Heon, M.W. Barsoum, Y. Gogotsi, Intercalation and delamination of layered carbides and carbonitrides, Nat. Commun. 4 (2013) 1–7. https://doi.org/10.1038/ncomms2664.

[129] J. Xuan, Z. Wang, Y. Chen, D. Liang, L. Cheng, X. Yang, Z. Liu, R. Ma, T. Sasaki, F. Geng, Organic-Base-Driven Intercalation and Delamination for the Production of Functionalized Titanium Carbide Nanosheets with Superior Photothermal Therapeutic

Performance, Angew. Chemie - Int. Ed. 55 (2016) 14569–14574. https://doi.org/10.1002/anie.201606643.

[130] K. Maleski, V.N. Mochalin, Y. Gogotsi, Dispersions of Two-Dimensional Titanium Carbide MXene in Organic Solvents, Chem. Mater. 29 (2017) 1632–1640. https://doi.org/10.1021/acs.chemmater.6b04830.

[131] M. Ashton, K. Mathew, R.G. Hennig, S.B. Sinnott, Predicted Surface Composition and Thermodynamic Stability of MXenes in Solution, J. Phys. Chem. C. 120 (2016) 3550–3556. https://doi.org/10.1021/acs.jpcc.5b11887.

[132] M.A. Hope, A.C. Forse, K.J. Griffith, M.R. Lukatskaya, M. Ghidiu, Y. Gogotsi, C.P. Grey, NMR reveals the surface functionalisation of Ti_3C_2 MXene, Phys. Chem. Chem. Phys. 18 (2016) 5099–5102. https://doi.org/10.1039/c6cp00330c.

[133] Y. Zhong, X.H. Xia, F. Shi, J.Y. Zhan, J.P. Tu, H.J. Fan, Transition metal carbides and nitrides in energy storage and conversion, Adv. Sci. 3 (2015). https://doi.org/10.1002/advs.201500286.

[134] Z. Ling, C.E. Ren, M.Q. Zhao, J. Yang, J.M. Giammarco, J. Qiu, M.W. Barsoum, Y. Gogotsi, Flexible and conductive MXene films and nanocomposites with high capacitance, Proc. Natl. Acad. Sci. U. S. A. 111 (2014) 16676–16681. https://doi.org/10.1073/pnas.1414215111.

[135] Q. Tang, Z. Zhou, P. Shen, Are MXenes promising anode materials for Li ion batteries? Computational studies on electronic properties and Li storage capability of Ti_3C_2 and $Ti_3C_2X_2$ (X = F, OH) monolayer, J. Am. Chem. Soc. 134 (2012) 16909–16916. https://doi.org/10.1021/ja308463r.

[136] M. Hu, Z. Li, T. Hu, S. Zhu, C. Zhang, X. Wang, High-Capacitance Mechanism for Ti_3C_2Tx MXene by in Situ Electrochemical Raman Spectroscopy Investigation, ACS Nano. 10 (2016) 11344–11350. https://doi.org/10.1021/acsnano.6b06597.

[137] Z. Xu, Y. Zhang, M. Liu, Q. Meng, C. Shen, L. Xu, G. Zhang, C. Gao, Two-dimensional titanium carbide MXene produced by ternary cations intercalation via structural control with angstrom-level precision, IScience. 25 (2022) 105562. https://doi.org/10.1016/j.isci.2022.105562.

[138] Y. Wen, T.E. Rufford, X. Chen, N. Li, M. Lyu, L. Dai, L. Wang, Nitrogen-doped Ti3C2Tx MXene electrodes for high-performance supercapacitors, Nano Energy. 38 (2017) 368–376. https://doi.org/10.1016/j.nanoen.2017.06.009.

[139] A.S. Levitt, M. Alhabeb, C.B. Hatter, A. Sarycheva, G. Dion, Y. Gogotsi, Electrospun MXene/carbon nanofibers as supercapacitor electrodes, J. Mater. Chem. A. 7 (2019)

269–277. https://doi.org/10.1039/c8ta09810g.

[140] L. Li, N. Zhang, M. Zhang, L. Wu, X. Zhang, Z. Zhang, Ag-Nanoparticle-Decorated 2D Titanium Carbide (MXene) with Superior Electrochemical Performance for Supercapacitors, ACS Sustain. Chem. Eng. 6 (2018) 7442–7450. https://doi.org/10.1021/acssuschemeng.8b00047.

[141] C. Zhao, Q. Wang, H. Zhang, S. Passerini, X. Qian, Two-Dimensional Titanium Carbide/RGO Composite for High-Performance Supercapacitors, ACS Appl. Mater. Interfaces. 8 (2016) 15661–15667. https://doi.org/10.1021/acsami.6b04767.

[142] Q. Wang, Z. Zhang, Z. Zhang, X. Zhou, G. Ma, Facile synthesis of MXene/MnO_2 composite with high specific capacitance, J. Solid State Electrochem. 23 (2019) 361–365. https://doi.org/10.1007/s10008-018-4143-4.

[143] W. Luo, Y. Ma, T. Li, H.K. Thabet, C. Hou, M.M. Ibrahim, S.M. El-Bahy, B. Bin Xu, Z. Guo, Overview of MXene/conducting polymer composites for supercapacitors, J. Energy Storage. 52 (2022) 105008. https://doi.org/10.1016/j.est.2022.105008.

[144] J. Yang, W. Bao, P. Jaumaux, S. Zhang, C. Wang, G. Wang, MXene-Based Composites: Synthesis and Applications in Rechargeable Batteries and Supercapacitors, Adv. Mater. Interfaces. 6 (2019) 1–32. https://doi.org/10.1002/admi.201802004.

[145] P. Forouzandeh, S.C. Pillai, MXenes-based nanocomposites for supercapacitor applications,Curr.Opin.Chem.Eng.33(2021)100710. https://doi.org/10.1016/j.coche.2021.100710.

[146] X. Zang, J. Wang, Y. Qin, T. Wang, C. He, Q. Shao, H. Zhu, N. Cao, Enhancing Capacitance Performance of Ti3C2Tx MXene as Electrode Materials of Supercapacitor: From Controlled Preparation to Composite Structure Construction, Nano-Micro Lett. 12 (2020) 1–24. https://doi.org/10.1007/s40820-020-0415-5.

[147] M. Vijayakumar, G. Elsa, A. Nirogi, R. Navaneethan, A.B. Sankar, M. Karthik, MXenes and their composites for hybrid capacitors and supercapacitors: a critical review, Emergent Mater. 4 (2021) 655–672. https://doi.org/10.1007/s42247-021-00204-7.

Chapter-II

Binder-free Ruthenium Oxide/MXene/Carbon Nanofiber Ternary Composite Electrode

2.1. Literature review

After activated carbons, carbon nanofibers (CNFs) have gained traction as electrode materials for supercapacitors due to their large specific surface area, binder-free nature, flexibility, superior electrolyte transport pathway, excellent electrolyte holdup, and high conductivity[1]. These carbon nanofibers, however, have a limited specific capacitance since they store charge by forming an electrical double layer at the electrode/electrolyte interface. To enhance the specific capacitance, CNFs were activated in a few studies; however, activation did not lead to significant improvements in capacitance as activation improves the micropore volume, which cannot be accessed by electrolyte [2,3]. Further tuning the mesopore and micropore volumes using activation is not a standard practice for carbon nanofibers, unlike activated carbon. Hence, porous carbon nanofibers with excellent mesopore volume were prepared using physical etching of selective polymer from polymer-polymer blends of polyacrylonitrile (PAN)/polyvinylpyrrolidone (PVP), PAN/poly methyl methacrylate (PMMA), and PAN/polyacrylic acid (PAA)[4–8]. The enhanced specific capacitance of these porous carbon nanofiber-based electrodes was attributed to the improved surface area and mesopore volume. Alternatively, the specific capacitance of CNFs was also improved by adding high theoretical capacitance metal oxides such as Co_3O_4, MnO_2, RuO_2, V_2O_5 and conductive polymers. These metal oxides and conductive polymers store charge by reversible faradic reactions as well as surface adsorption and desorption of charge at the electrode-electrolyte interface [9–11]. However, these high-capacitance metal oxides struggle with low surface area and low electrical conductivity, which limit their electrochemical performance. In addition, nano structuring to enhance the surface area is not recommended for these metal oxides as they suffer from severe agglomeration. As a result, many studies focused on depositing or incorporating these nano-sized metal oxides in carbon or conductive polymer fiber support [12,13]. These composites exhibited specific capacitance in the range of 220 to 1384 F g^{-1}, with excellent cyclic stability[14,15].

Since the discovery of MXene in 2011, two-dimensional MXenes (transition metal carbides/nitrides/carbonitrides) that resemble graphene have emerged as promising electrode materials for energy storage devices [16]. In MXene ($M_{n+1}X_nT_x$), M represents the transition metal, X represents the element C or N, and Tx represents the surface termination groups like (−OH, −F, −Cl, −O). Usually, these MXenes are produced by selective etching of atomic layers of Al from the MAX phase. These 2D layered materials possess high surface area, hydrophilic

nature (termination groups) and high electric conductivity [17]. $Ti_3C_2T_x$ MXenes exhibit macroscopic hydrophilicity similar to clay materials when etched with a suitable etching agent. It is, therefore, possible to intercalate water molecules and cations between the layers of MXene. During the intercalation of water molecules, different hydration states (hydration heterogeneity) coexist in MXene layers due to the non-uniform intercalation of water molecules. It is important to engineer these interactions in order to optimize their electrochemical performance so that electrolyte ions can diffuse more rapidly [18]. In addition to the charge storage on the surface and charge storage through faradic reactions, these 2D layered materials also allow the intercalation of various electrolyte ions, which further enhances the specific capacitance by increasing the C-lattice parameter [19]. However, the use of these layered materials as an electrode in bulk form is limited because of the self-restacking tendency of the layers [20,21]. Hence, binary composites of MXene with CNFs were studied as electrode material for supercapacitor [22,23]. These studies revealed that the layered structure improved the carbon-based materials' rate performance due to the intercalation of electrolyte ions [24]. In summary, binary composites of CNF and metal oxides or MXenes as electrodes for supercapacitors exhibited superior performance in terms of improved specific capacitance and rate performance. Additionally, when used as it is, these binary composite materials inhibited the issues associated with metal oxides (low electrical conductivity) and MXene (self-restacking). We envisage that the combination of metal oxide, MXene, and CNF as a ternary composite electrode may further improve the overall electrochemical performance of the supercapacitor. However, to the best of our knowledge, no study has been reported on using this ternary composite as an electrode. In this work, a binder-free ternary composite electrode consisting of CNF, MXene and RuO_2 was prepared by electrospinning RuO_2/MXene/PAN precursor solution and carbonizing it. RuO_2 was chosen as metal oxide for its advantages, such as high theoretical capacitance, wide electrochemical window, good thermal stability, and excellent cyclic life [19]. The effect of MXene and metal oxide incorporation on the electrochemical performance was investigated.

2.2 Materials and methods

Polyacrylonitrile (PAN), with a molecular weight of 1,50,000, and Lithium Fluoride (LiF, 99.9%) were procured from Sigma Aldrich (India). N, N-dimethylformamide (DMF), and hydrochloric acid (HCl, 37%) solvents were purchased from SRL Chemicals and Finar Chemicals, India, respectively. Ti_3AlC_2 (MAX phase) powder was obtained from Aritech Chemazone Chemicals, India. Reagents and chemicals were used as received without any further modification.

2.2.1 Synthesis of MXene (Ti_3C_2Tx)

Al layer from the MAX phase powder was selectively etched using LiF/HCl solution to prepare MXene ($Ti_3C_2T_x$) as reported previously by Alhabeb et al.[25] First, 1 g LiF was slowly added to 20 ml of 9 M HCl solution in the Teflon reactor. This LiF/HCl solution was stirred for 5 min, then 1 g of Ti_3AlC_2 powder was added and stirred further for 24 h at 35 °C to obtain multilayered MXene. A multilayered $Ti_3C_2T_x$ suspension with a pH value greater than 6 was obtained after washing the resultant stable suspension in deionized water and centrifuging several times at 3500 rpm for 6 min. Further, the obtained multilayered $Ti_3C_2T_x$ was sonicated in DMF solvent under a nitrogen atmosphere for another 2 h at 450 W with 50 % amplitude and centrifuged for 1 h at 3500 rpm to obtain a colloidal-like supernatant containing delaminated $Ti_3C_2T_x$. Understanding the effects and mechanisms behind the presence of MXene in composite films is crucial for optimizing their properties and expanding their applications, presence of ~40 mg/L can substantially increase the conductivity of the composite.

2.2.2 Preparation of the freestanding binary MXene/CNF composite electrode

PAN (12 wt.%) was slowly added to MXene dispersed colloidal solution and stirred for two hours to obtain the PAN polymer solution. Electrospinning was conducted with a plastic syringe equipped with an 18-gauge needle filled with MXene/PAN solution. To obtain continuous uniform nanofibers by electrospinning polymer precursor, a voltage of 16 kV, a tip-to-collector distance of 12 cm, and a feed flow rate of 1 ml h^{-1} were used. Nanofibers were collected over an Aluminum foil-wrapped rotating drum (400 rpm) for 6 h, and the deposited fiber mat was peeled off from Al foil. This mat was stabilized in the oven at 250 °C for 2 h before it was carbonized inside the tubular furnace (Carbolite-Gero, Germany) at 900 °C. The temperature of the furnace was raised to 900 °C with a ramp rate of 5 °C per min after stabilization, and it was then maintained there for 2 h and cooled to room temperature to produce flexible MXene/CNF composite electrodes.

2.2.3 Preparation of the freestanding ternary RuO_2/MXene/CNF composite

The ternary composite precursor was prepared by dispersing the MXene suspension in DMF solvent and gradually adding 9 wt.% of PAN followed by 2 wt.% of $RuCl_3.6H_2O$. The solution was stirred for 8 h and ultrasonically sonicated for 1 h to obtain an electrospinning precursor with a uniform and well dispersed ternary composition. This uniformly dispersed solution was

placed into a 10 ml syringe fitted with an 18-gauge needle and then attached to a syringe pump. Without changing the solution parameters, the electrospinning operating parameters were optimized. The syringe-to-collector distance, operating voltage, and flow rate were set to 10 cm, 15 kV, and 1 ml h^{-1}, respectively, to obtain continuous nanofiber deposition on an Al-foil-wrapped rotating drum collector rotating at 400 rpm. Then, the fibers were deposited for 8 h and the fiber mat was peeled off from Al-foil. After the ternary polymer nanofibers were obtained, they were stabilized at 250 °C for 2 h and then carbonized using a tubular furnace at 900 °C for 1 h, with a heating ramp of 5 °C for each case. As can be seen in Fig.2.1, a step-by-step synthesis procedure starting from MXene to a ternary electrode is presented.

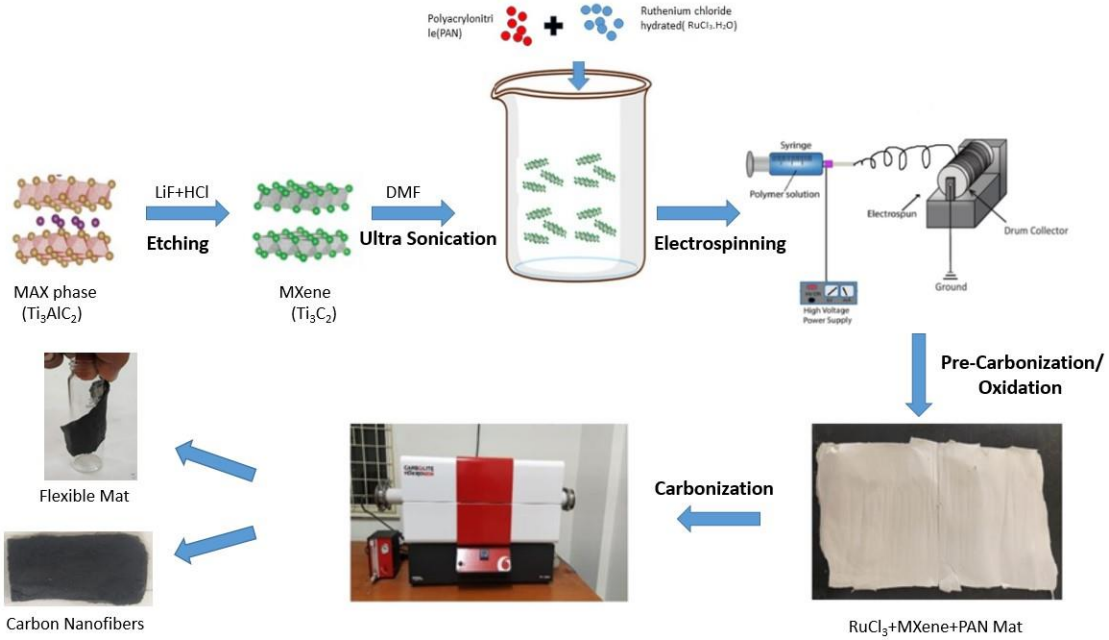

Figure 2.1. Schematic illustration of the synthesis of MXene and RuO_2/MXene/CNFs composites.

2.2.4 Material Characterizations

The morphology of gold-coated ternary and binary CNF composites was examined using a TESCAN VEGA3 scanning electron microscope (SEM). The mean fiber diameter of the sample was obtained by analyzing 100 randomly selected fibers on the SEM micrograph using the ImageJ software. The composite crystallinity was determined using a PANalytical XRD setup with a CuKα (wavelength = 1.5406 Å). Further, the lattice fringes and distribution of the MXene and RuO_2 in the individual CNF were examined using a JEOL JEM-3010 High Resolution Transmission Electron Microscope (HR-TEM), operated at an accelerated voltage

of 200 kV. The chemical composition/ functional groups of the composites were examined by Fourier transform infrared (FTIR) spectroscopy (Perkin Elmer 100).

2.2.5 Electrochemical characterizations

All the electrochemical tests were conducted on a CH instrument (CHI 6002E) electrochemical workstation using a standard three-electrode and two-electrode system configurations using the binary and ternary composite freestanding CNF mats as the working electrodes. In a three-electrode system, Ag/AgCl was used as the reference electrode, and platinum wire as the counter electrode. In addition, two electrode symmetric supercapacitors were fabricated with composite electrodes on both sides and a GF/D microfiber filter filled with electrolyte solution as a separator. A 3 M KOH solution was used as an electrolyte in the 3-electrode and 2-electrode systems. Cyclic voltammograms were recorded using a 3-electrode system to obtain a voltage window and to investigate the charge storage mechanism. Galvanostatic charge-discharge (GCD) curves were recorded on two electrode systems to evaluate the specific capacitance, rate performance, and energy/power densities. Electrochemical impedance spectroscopy (EIS) was also performed within the frequency range of 0.01 Hz–100 kHz to investigate the electrochemical cell internal resistances. Specific capacitances of the two electrode systems were calculated using, $C_{sp} = 2(I. \Delta t) / (V.m)$, where, Csp ($F\ g^{-1}$) is specific capacitance, I = current in amps (A), ΔV = voltage window, t = the discharge time in seconds, and m = mass of the active material.

2.3 Results and Discussion

2.3.1 Morphological and structural investigations

2.3.1.1 FESEM analysis of RuO_2/MXene/CNF and MXene/CNF nanocomposites

Fig.2.2(a) and 2.2(b) depict the lower magnification SEM images of the binary (MXene/CNF) and ternary (RuO_2/MXene/CNF) composites. Higher magnification images Fig.2.2(c) and 2.2(d), revealed that the fibers embedded with metal oxide nanoparticles (Fig.2.2(d)) are rougher, with small pits on their surfaces, compared to the relatively smooth binary composite fibers (Fig.2.2(c)). This variation is usually due to the difference between solvent evaporation during the electrospinning of nanofibers with metal oxide particles and those without [26]. Additionally, the effect of the composition on the distribution of nanofiber diameters was examined. The average fiber diameter of the binary and ternary composite was calculated as 309 ± 20 nm and 369 ± 25 nm, respectively. This increase in diameter of the ternary composite can be attributed to the higher viscosity of the precursor solution containing RuO_2 nanoparticles and the decrease in solvent content.

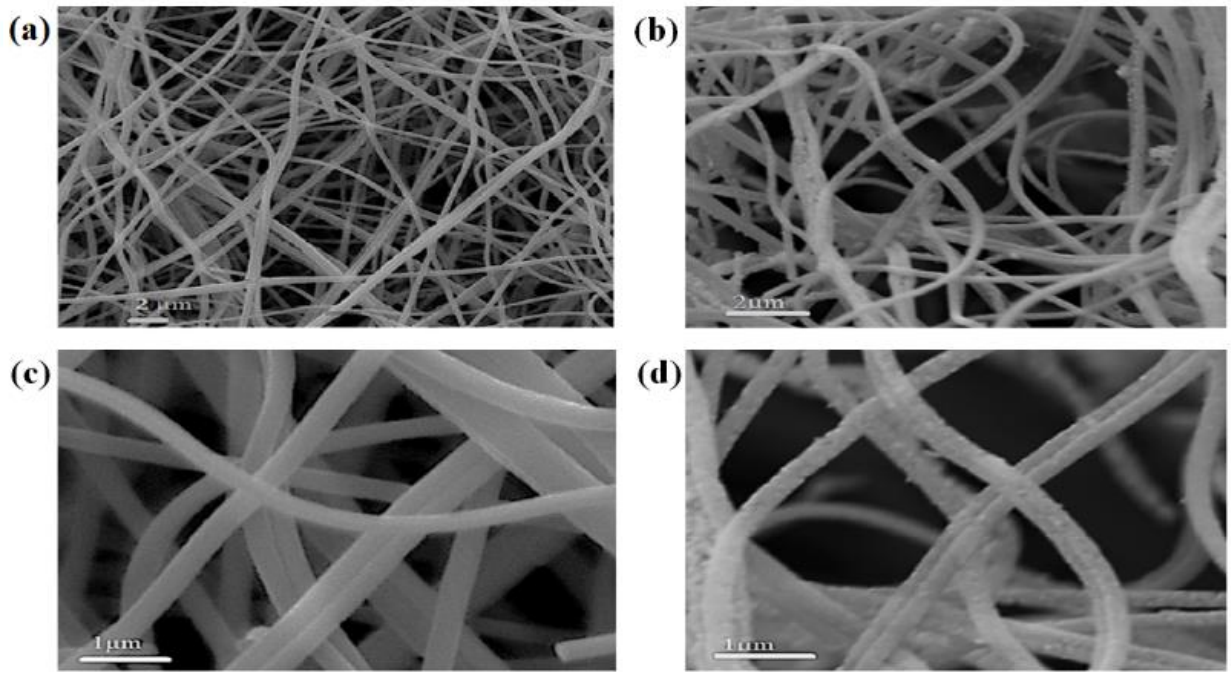

Figure 2.2. SEM images of (a), (c) binary composite (MXene/CNFs) at low and high magnification and (b), (d). ternary composite (RuO_2/MXene/CNFs)

2.3.1.2 XRD analysis of RuO_2/MXene/CNF and MXene/CNF nanocomposites

XRD plots are used to examine the differences in the crystallinity of the ternary, binary composites, and pristine CNFs samples, as shown in Fig.2.3(a). XRD pattern of ternary and binary composite unveils a diffraction peak at 6.4°, which corresponds to the (0 0 2) plane of layered MXene nanosheets, a broadening of the diffraction band at ~6.4° for ternary composite is due to hydration heterogeneity.18 The diffraction peaks at 26.9°, 36.5°, 40.7°, and 56.7° in the ternary composite XRD pattern are indexed to the (1 1 0), (0 0 2), (0 1 0), (1 0 0), (1 1 2) planes of ruthenium oxide respectively [27]. Further, a broad diffraction peak of ~26° corresponding to the (0 0 2) plane can be observed in all three samples' diffraction patterns, which confirms the amorphous nature of the carbon nanofiber. Further, in a ternary composite, the peak shift in this peak is observed because of improved crystallinity with decreasing d spacing of carbon nanofibers due to the addition of RuO_2 [28].

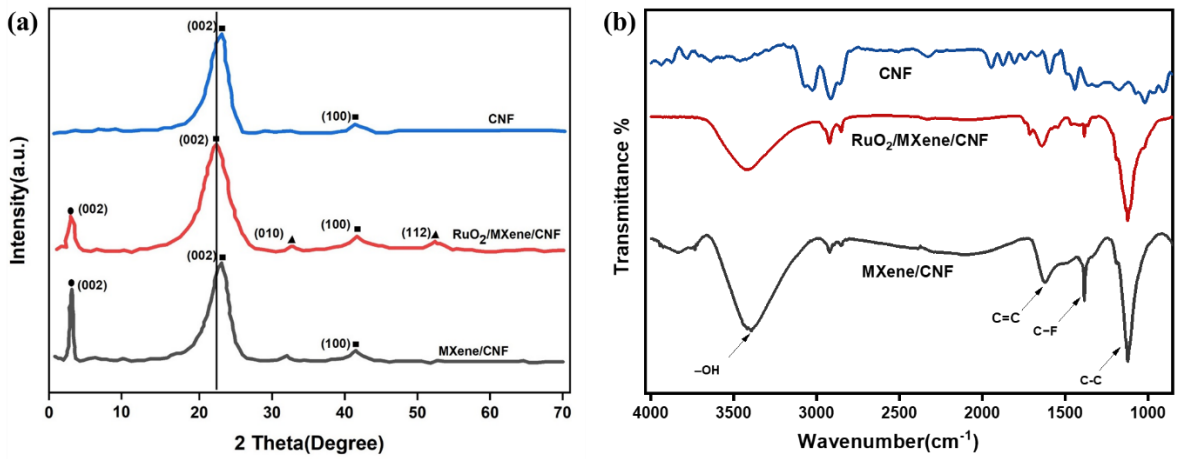

Figure 2.3 (a) XRD of RuO_2/MXene/CNFs composite and (b) FTIR patterns for CNF, MXene/CNF and RuO_2/MXene/CNFs composites.

2.3.1.3 FTIR analysis of RuO_2/MXene/CNF and MXene/CNF nanocomposites

Fig.2.3(b) illustrates the FTIR spectrum of all three electrodes with and without the incorporation of MXene. Peaks at 1384 and 3375 cm^{-1} in binary and ternary composite correspond to C–F and –OH vibrations, which confirms the incorporation of MXene into the carbon nanofiber host [29]. The peak between 1500–1650 cm^{-1} for all pristine and composite nanofiber-based electrodes is due to aromatic carbon (C=C) vibration in the amorphous carbon derived from PAN [30].

2.3.1.4 HR-TEM analysis of RuO_2/MXene/CNF and MXene/CNF nanocomposites

Fig.2.4(a) shows TEM images of a ternary composite single nanofiber, while Fig.2.4(b) shows its high magnification image, which confirms the dispersion of RuO_2 nanoparticles and MXene into carbon nanofiber. Further high-magnification Fig.2.4(c) and 2.4(d) confirm the crystallinity of these incorporated materials with well-defined lattice fringes as indicated in the inset. The interlayer spacing of the MXene (1 0 0) plane and RuO_2 (1 1 2) plane was determined as 0.28 nm and 0.33 nm using high magnification images (Fig.2.4(c) and 2.4(d)). Additionally, the flexibility of the freestanding composite nanofibrous electrode was examined by bending it several times and then restoring it to its flat position.

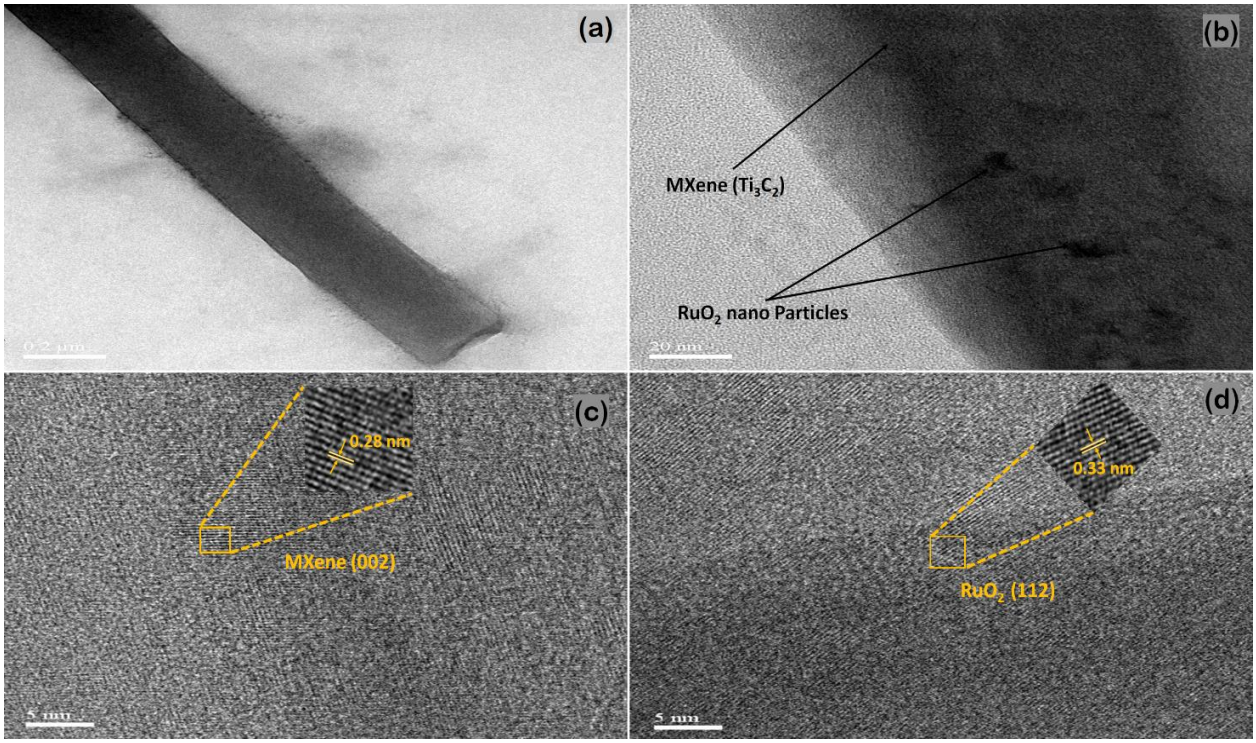

Figure 2.4. (a) Ternary composite single nanofiber HRTEM image (b) lattice fringes of RuO_2/MXene/CNF composite, (c) High magnification MXene lattice fringes and (d) High magnification RuO_2 lattice fringes images.

2.3.1.5 Flexibility analysis of RuO_2/MXene/CNF nanocomposite

Fig.2.5(a–f) illustrates the digital images of a fabric-like ternary composite electrode that can be bent to different angles and then returned to its original shape without causing any damage to the electrode. Further, the fiber mat wrapped on the glass vial in Fig.2.1 confirms the flexibility of the electrodes. These bending and wrapping experiments indicate the high degree of flexibility of the composite electrode, making them suitable for flexible supercapacitors.

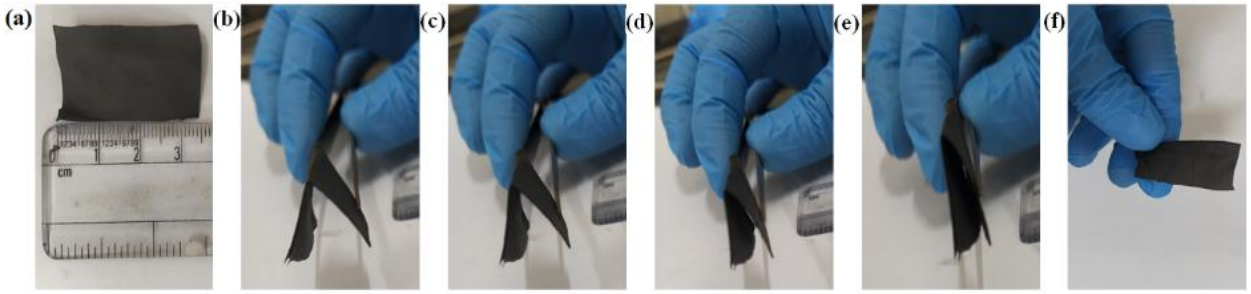

Figure 2.5. (a-f). Digital photographs of RuO_2/MXene/CNF composite twisted, bent of membrane.

2.3.2 Electrochemical performance

2.3.2.1 Cyclic voltammetry analysis of RuO_2/MXene/CNF and MXene/CNF nanocomposite electrodes

Initially, the electrochemical studies of the binary and ternary composites were tested using a three-electrode system, where an aqueous 3 M KOH was used as an electrolyte. Cyclic voltammetry (CV) curves were recorded with a 5 mV s^{-1} scan rate in a voltage range of 0 to 0.7 V for the binary and ternary electrodes, as shown in Fig.2.6(a). It was observed that the ternary composite electrochemical potential window is wider than the binary composite electrochemical potential window. The binary composite cyclic voltammogram is rectangular, indicating that binary composite electrodes charge storage by double-layer formation. In contrast, the ternary composite electrode with RuO_2 displays a quasi-rectangular CV profile with an oxidation peak at 0.5 V and a reduction peak at 0.2 V due to the reversible faradic reactions of metal oxide. Further, the integral area of the ternary composite is significantly larger than that of the binary compound, which is an indication of the higher specific capacitance. The CV curves at varying scan rates (5–100 mV s^{-1}) were also recorded for the ternary composite electrode, as shown in Fig.2.6(b), which confirms the excellent rate performance by maintaining the similar shape of the CV curves even at a higher scan rate (100 mV s^{-1}) with minimum change in the integral area of the CV curve. Increasing the scan rate, however, results in an insignificant change in the oxidation and reduction peak positions, indicating significant reversibility in faradic reactions. The scan rate determines how quickly the potential is swept during cyclic voltammetry (CV) or other electrochemical techniques. At higher scan rate allows faster data acquisition but may miss slow electrochemical processes and at slower scan rate captures more details but requires longer experiment times. Extremely high scan rates can cause capacitive current overshoots or distort the response. Consider the kinetics of redox reactions or charge storage processes in the composite nanofiber. Some materials exhibit different behavior at varying scan rates. The electrolyte concentration affects ion mobility and charge transfer kinetics. Current density reflects the charge/discharge rate during specific capacitance measurements. Higher current densities yield faster charge/discharge but may lead to non-ideal behavior (e.g., IR drop, diffusion limitations). The choice of electrolyte composition significantly affects supercapacitor performance.

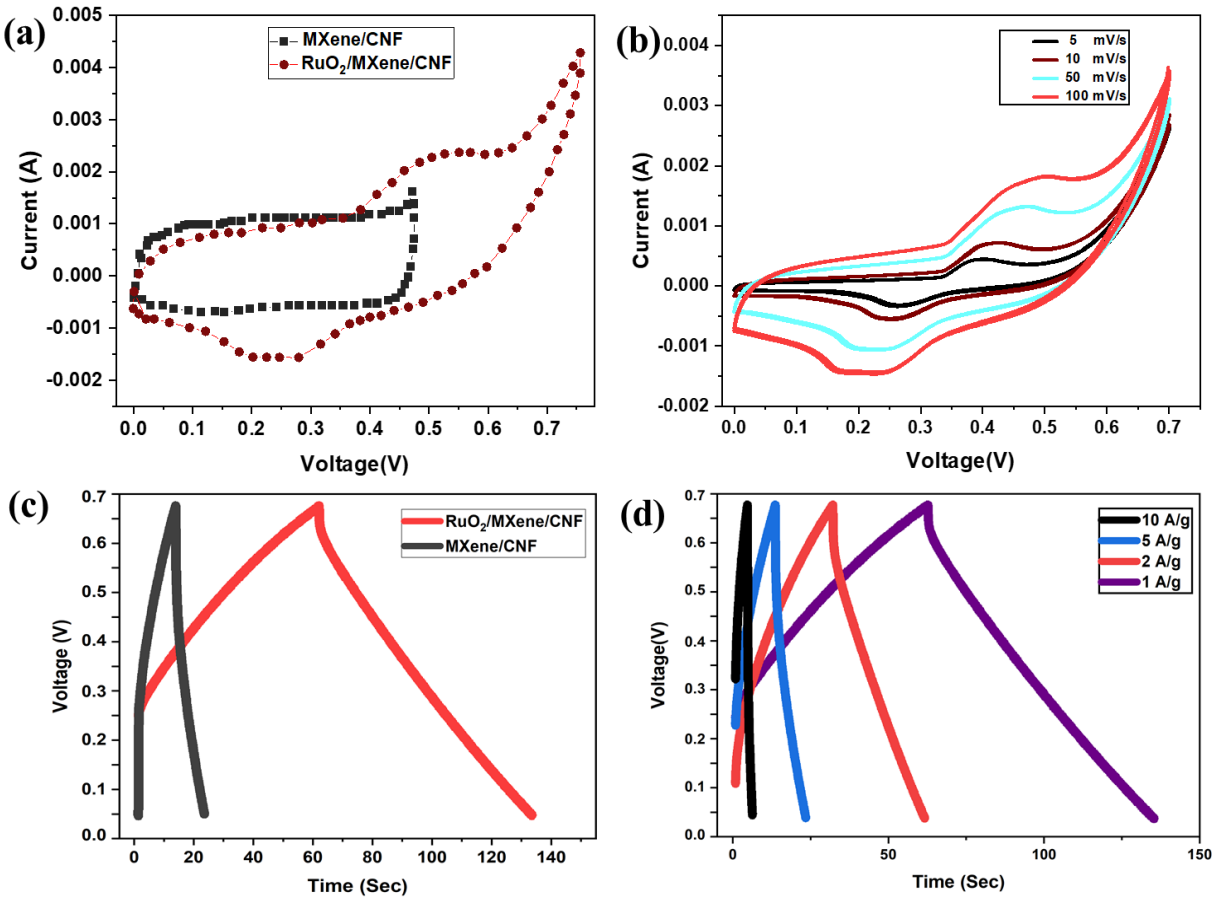

Figure 2.6. Cyclic voltammetry curves of (a) the binary and ternary composite at a scan rate of 5 mV s^{-1} (b) the ternary composite at different scan rates; GCD curves of (c) binary and ternary at 1 A g^{-1} current density, (d) GCD curves of ternary composite at various current densities.

2.3.2.3 GCD analysis of RuO_2/MXene/CNF and MXene/CNF nanocomposite electrodes

The GCD curves were recorded at the different current densities to determine the specific capacitance and cyclic stability. The GCD curve of the binary composite exhibited linear triangle-like behavior due to EDLC-type charge storage, as shown in Fig.2.6(c). On the other hand, the ternary composite shows capacitive behavior with quasi symmetrical curves, in which the bending of the curves is owing to the pseudocapacitive charge storage. The ternary composite also indicates a higher IR drop than the binary composite since less conductive RuO_2 increases the internal resistance. The specific capacitance from the GCD curve was calculated as 339 F g^{-1} for the ternary composite, which is more than double that of the binary composite electrode (149 F g^{-1}) at the current density of 1 A g^{-1}. Additionally, the ternary composite GCD curves were recorded at different current densities to investigate the rate capability, as shown

in Fig.2.6(d). The shape of the GCD curves remains unchanged with increasing current densities, but the specific capacitance decreases with increasing current density. A two-electrode symmetric supercapacitor was assembled using a Swagelok set up to ensure the practical usage of the developed electrode materials. Binary composite electrode CV curves recorded at 5 mV s^{-1} scan rate show a quasi-rectangular CV curve, smaller integrated area, and narrower potential window than ternary composite electrode CV curves, as shown in Fig.2.7(a) [31]. Fig.2.7(b) depicts the CV curves of the ternary composite electrode-based supercapacitor at different scan rates. The CV curves deformed slightly at the higher scan rates, mainly because of decreased reaction time for the faradic reactions of RuO_2 in the ternary composite. The GCD curves shown in Fig.2.7(c) were recorded at a current density of 1A g^{-1} for both electrodes. Based on these curves, ternary composite specific capacitance is significantly higher than binary composite specific capacitance with an isosceles triangular shape and a small IR drop. These GCD curves were also used to determine specific capacitances for the binary and ternary composites as 322 F g^{-1} and 156 F g^{-1}, respectively.

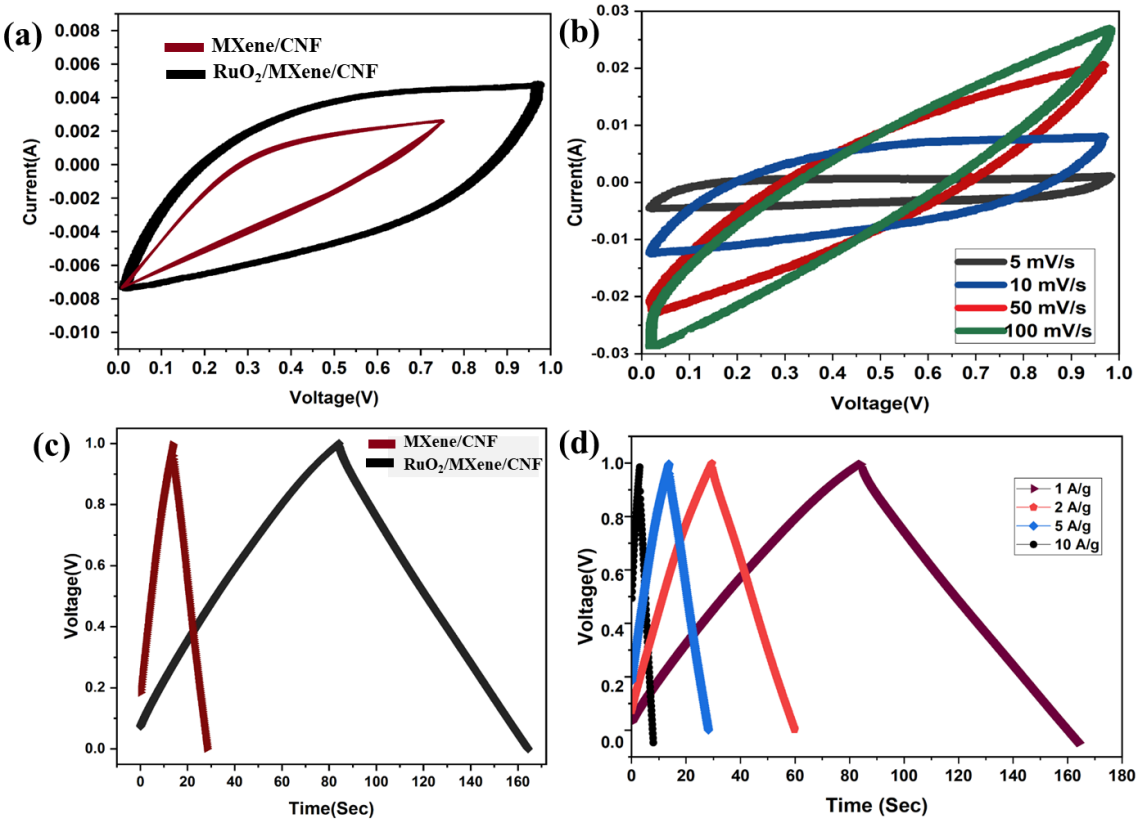

Figure 2.7. Comparison of CV curves of (a) the ternary and binary composite at a scan rate of 5 mV s^{-1} (b) the ternary composite at different scan rates. GCD curves of (c) the ternary and binary composite at 1 A g^{-1} current density, (d) the ternary composite at various current densities.

Additionally, GCD curves of ternary composite electrode-based symmetric supercapacitors were recorded at different current densities (1–10 A g^{-1}), as shown in Fig.2.7(d). The specific capacitance of the cell decreased from 322 F g^{-1} to 203 F g^{-1} with increasing current density from 1 A g^{-1} to 10 A g^{-1}, as depicted in Fig.2.8(a). Fig.2.8(a) shows the rate capability comparison of both the binary and ternary composite. The binary composite showed less capacitance retention (57.9%) than the ternary composite (62.9%) when the current density increased from 1 to 10 A g^{-1}. Further, 2500 galvanostatic charge/discharge cycles at a current density of 1 A g^{-1} were carried out on the binary and ternary composite electrode cell to test their cyclic stability. The specific capacitance fade was observed to be less than 10% for both systems, which is in line with most of the systems reported in the literature. The Ragone plot for the ternary and binary electrode system is presented in Fig.2.8(d). A ternary electrode system's energy density drops moderately when power density increases from 900 to 2000 W kg^{-1}, and then, the drop in energy density is sluggish. Overall, the energy density dropped from 20.17 to 12.7 Wh kg^{-1} when the power density increased from 900 to 9 kW kg^{-1}. Compared with the binary composite electrode system, the ternary composite system showed nearly 2-fold energy density at all power density values reported.

2.3.2.3 Electrochemical Impedance spectroscopy analysis of RuO_2/MXene/CNF and MXene/CNF nanocomposite Electrodes

EIS was used to study the internal resistance of the binary and ternary composites with and without RuO_2. The Nyquist plots of ternary and binary composites obtained between 0.01 and 10^5 Hz are illustrated in Fig.2.8(b), with an expanded view in the inset. The ternary composite shows high equivalent series resistance (ESR) and charge transfer resistance values (0.59 and 0.93 Ω) than the binary composite (0.55 and 0.79 Ω). A ternary electrode system ESR and charge transfer resistance gain can be related to the dispersion of less conductive RuO_2. EIS plots also show a nearly vertical line parallel to the imaginary axis, indicating the ideal capacitive behavior of both systems at low frequencies [32]. pure MXene and CNF resistance values in results in the discussion alongside the composite materials allows us to understand their individual contributions and synergies. EIS of sample have less resistance with distinct Impedance patterns for each sample. Table 3.1 summarizes the electrochemical performance of prepared electrodes compared to RuO_2/carbon composite electrode systems with an aqueous electrolyte. According to most studies, the specific capacitance increased monotonically with increasing RuO_2 content. It was found that the specific capacitance values for various binary composite materials reported in the literature ranged between 151 and 287 F g^{-1}. However,

from this study, the ternary composite with only 11% RuO_2 and MXene delivered a capacitance of 322 F g^{-1} at 1 A g^{-1}. This is significantly higher specific capacitance than most binary composites reported, as shown in Table 3.1. The capacity retention of this composite is in the same range as that of other binary composites, and the capacity to fade over 2500 cycles is approximately 10%.

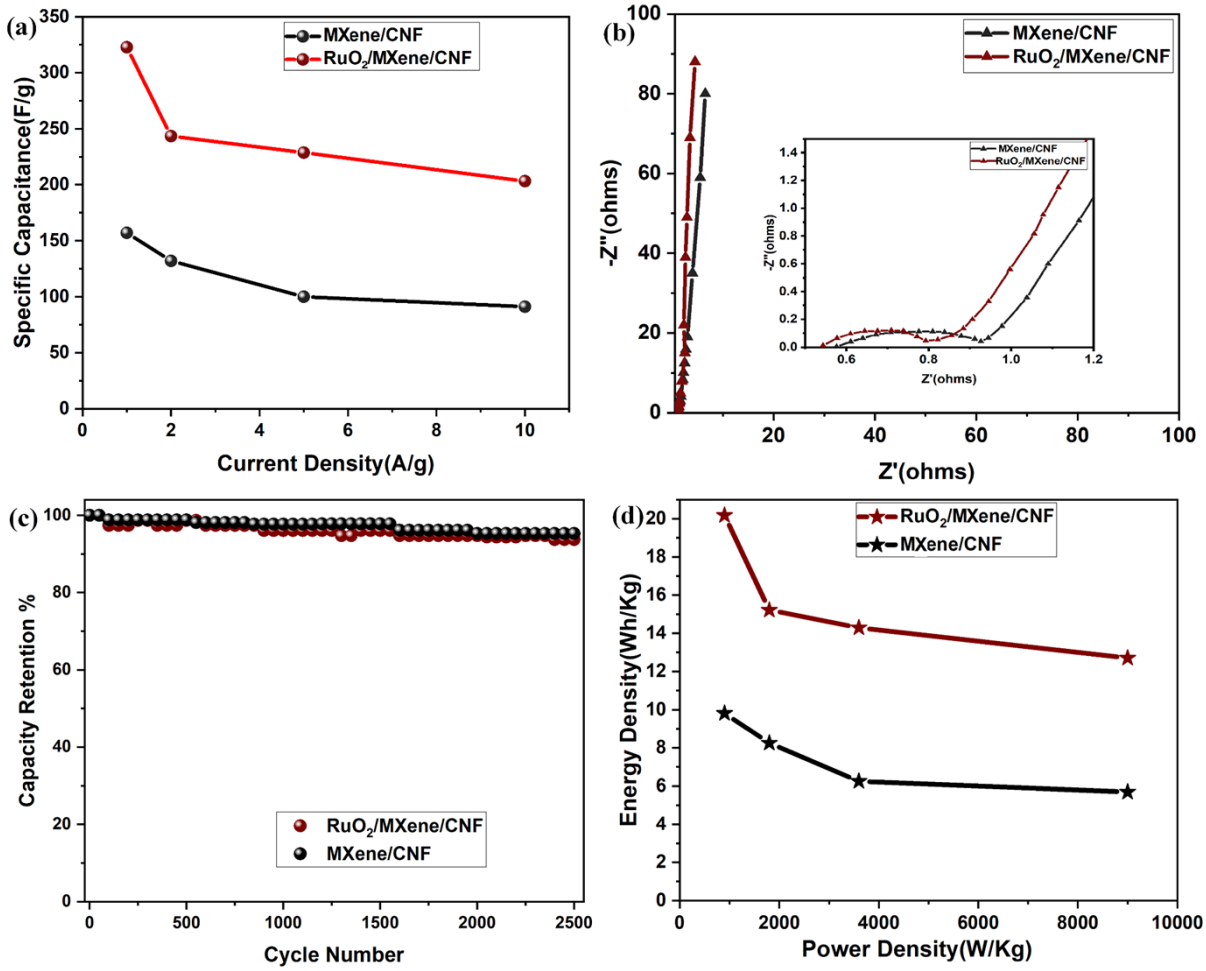

Figure 2.8. (a) Comparison of specific capacitances from GCD curves for binary and ternary composite electrodes; (b) EIS spectra of binary and ternary composite electrodes; (c) Ternary composite electrode cyclic performance at 1 A g^{-1} and (d) Ragone plot for binary and ternary composites.

Table 2.1: Specific Capacitance Performance of different Ruthenium Oxide/various Carbon composites.

Sample	Performance	Content (wt. %)	Retention/Cycles
RuO_2/ACNF [15]	180 F g^{-1} at 1 A g^{-1}	8	-
RuO_2/CNF [33]	188 F g^{-1} at 1 mA cm^{-2}	23	93/3000
RuO_2/CNF [34]	224 F g^{-1} at 0.2 A g^{-1}	20	90/3000
RuO_2/CNF [35]	220 F g^{-1} at 5 mV s^{-1}	20	98/1000
RuO_2/ACNF [36]	190 F g^{-1} at 1 mA cm^{-2}	30	75/3000
RuO_2/CNF [14]	261 F g^{-1} at 1 mA cm^{-2}	20	92/2000
RuO_2/Mesoporous carbon [37]	243 F g^{-1} at 5 mV s^{-1}	54	-
RuO_2/carbon aerogel [38]	206 F g^{-1} at 2 mV s^{-1}	35	-
RuO_2/active carbon [39]	243 F g^{-1} at 1 A g^{-1}	25	-
RuO_2/Carbon Xerogel [40]	256 F g^{-1} at 1 A g^{-1}	14	90/2000
RuO_2/active Carbon [41]	287 F g^{-1} at 2 mV s^{-1}	20	93/1000
RuO_2/Carbon [42]	151 F g^{-1} at 5 mV s^{-1}	10	-
RuO_2/MXene/CNF (This work)	339 F g^{-1} at 5 mV s^{-1} 322 F g^{-1} at 1 A g^{-1}	11	90/2500

2.4 Conclusions

In summary, freestanding flexible RuO_2/MXene/CNFs ternary and binary RuO_2/MXene composite electrodes were synthesized in this study using a one-step electrospinning technique, and their electrochemical performance was investigated. This study revealed that the impregnation of metal oxide into the ternary composite increased its specific capacitance and energy density by providing a wider potential window. A ternary composite electrode delivered nearly twice the specific capacitance (322 F g^{-1}) when compared to a binary composite electrode (156 F g^{-1}). This excellent electrochemical performance of the ternary composite was attributed to its intercalative pseudocapacitive charge storage and enhanced conductivity. This work opens up new directions in developing MXene and other metal oxides-based ternary carbon composite electrodes for supercapacitors with excellent specific capacitance, energy density and rate capability.

2.5 References

[1] B. Joshi, E. Samuel, Y. il Kim, A.L. Yarin, M.T. Swihart, S.S. Yoon, Review of recent progress in electrospinning-derived freestanding and binder-free electrodes for supercapacitors,Coord.Chem.Rev.460(2022)214466. https://doi.org/10.1016/j.ccr.2022.214466.

[2] A. Platek-Mielczarek, J. Conder, K. Fic, C.M. Ghimbeu, Performance evaluation of electrochemical capacitors with activated carbon spheres as electrode material and aqueous electrolyte,J.PowerSources.542(2022)231714. https://doi.org/10.1016/j.jpowsour.2022.231714.

[3] K. Dujearic-Stephane, M. Gupta, A. Kumar, V. Sharma, S. Pandit, P. Bocchetta, Y. Kumar, The effect of modifications of activated carbon materials on the capacitive performance: surface,microstructure,andwettability,J.Compos.Sci.5(2021). https://doi.org/10.3390/jcs5030066.

[4] L. Wang, G. Zhang, X. Zhang, H. Shi, W. Zeng, H. Zhang, Q. Liu, C. Li, Q. Liu, H. Duan, Porous ultrathin carbon nanobubbles formed carbon nanofiber webs for high-performance flexiblesupercapacitors,J.Mater.Chem.A.5(2017)14801–14810. https://doi.org/10.1039/c7ta03445h.

[5] S. Bhoyate, P.K. Kahol, B. Sapkota, S.R. Mishra, F. Perez, R.K. Gupta, Polystyrene activated linear tube carbon nanofiber for durable and high-performance supercapacitors, Surf.CoatingsTechnol.345 (2018) 113–122. https://doi.org/10.1016/j.surfcoat.2018.04.026.

[6] H. Niu, J. Zhang, Z. Xie, X. Wang, T. Lin, Preparation, structure and supercapacitance of bonded carbon nanofiber electrode materials, Carbon N. Y. 49 (2011) 2380–2388. https://doi.org/10.1016/j.carbon.2011.02.005.

[7] B.H. Kim, K.S. Yang, J.P. Ferraris, Highly conductive, mesoporous carbon nanofiber web as electrode material for high-performance supercapacitors, Electrochim. Acta. 75 (2012) 325–331. https://doi.org/10.1016/j.electacta.2012.05.004.

[8] G. Duan, H. Fang, C. Huang, S. Jiang, H. Hou, Microstructures and mechanical properties of aligned electrospun carbon nanofibers from binary composites of polyacrylonitrile and polyamic acid, J. Mater. Sci. 53 (2018) 15096–15106. https://doi.org/10.1007/s10853-018-2700-y.

[9] X. Fan, Y. Lu, H. Xu, X. Kong, J. Wang, Reversible redox reaction on the oxygen-containing functional groups of an electrochemically modified graphite electrode for the pseudo-capacitance,J.Mater.Chem.21(2011)18753–18760. https://doi.org/10.1039/c1jm13214h.

[10] X. Mao, T. Hatton, G. Rutledge, A Review of Electrospun Carbon Fibers as Electrode Materials for Energy Storage, Curr. Org. Chem. 17 (2013) 1390–1401. https://doi.org/10.2174/1385272811317130006.

[11] H. Yang, Recent Advances of Flexible Electrospun Nanofibers-based Electrodes for Electrochemical Supercapacitors: A Minireview, Int. J. Electrochem. Sci. 14 (2019) 7811–7831. https://doi.org/10.20964/2019.08.28.

[12] X.L. Song, J.X. Guo, M.X. Guo, D.Z. Jia, Z.P. Sun, L.X. Wang, Freestanding needle-like polyaniline-coal based carbon nanofibers composites for flexible supercapacitor,

Electrochim.Acta. 206 (2016) 337–345. https://doi.org/10.1016/j.electacta.2016.04.155.

[13] J.G. Wang, Y. Yang, Z.H. Huang, F. Kang, A high-performance asymmetric supercapacitor based on carbon and carbon-MnO_2 nanofiber electrodes, Carbon N. Y. 61 (2013) 190–199. https://doi.org/10.1016/j.carbon.2013.04.084.

[14] Y.-W. Ju, G.-R. Choi, H.-R. Jung, C. Kim, K.-S. Yang, W.-J. Lee, A Hydrous Ruthenium Oxide-Carbon Nanofibers Composite Electrodes Prepared by Electrospinning, J. Electrochem. Soc. 154 (2007) A192. https://doi.org/10.1149/1.2426898.

[15] K.S. Yang, B.H. Kim, Highly conductive, porous RuO_2/activated carbon nanofiber composites containing graphene for electrochemical capacitor electrodes, Electrochim. Acta. 186 (2015) 337–344. https://doi.org/10.1016/j.electacta.2015.11.003.

[16] S. Panda, K. Deshmukh, S.K. Khadheer Pasha, J. Theerthagiri, S. Manickam, M.Y. Choi, MXene based emerging materials for supercapacitor applications: Recent advances, challenges, and future perspectives, Coord. Chem. Rev. 462 (2022) 214518. https://doi.org/10.1016/j.ccr.2022.214518.

[17] R. Peng, K. Han, K. Tang, MXene Surface Functional Groups Regulation: Enhancing Area Capacitance of Divalent Zinc Ion Micro-Supercapacitor, J. Electrochem. Soc. 169 (2022) 060523. https://doi.org/10.1149/1945-7111/ac72ca.

[18] Q. Jiang, N. Kurra, M. Alhabeb, Y. Gogotsi, H.N. Alshareef, All Pseudocapacitive MXene-RuO_2AsymmetricSupercapacitors,Adv.EnergyMater.8(2018). https://doi.org/10.1002/aenm.201703043.

[19] S. Célérier, S. Hurand, C. Garnero, S. Morisset, M. Benchakar, A. Habrioux, P. Chartier, V. Mauchamp, N. Findling, B. Lanson, E. Ferrage, Hydration of Ti_3C_2Tx MXene: An Interstratification Process with Major Implications on Physical Properties, Chem. Mater. 31 (2019) 454–461. https://doi.org/10.1021/acs.chemmater.8b03976.

[20] Z. Zhou, W. Panatdasirisuk, T.S. Mathis, B. Anasori, C. Lu, X. Zhang, Z. Liao, Y. Gogotsi, S. Yang, Layer-by-layer assembly of MXene and carbon nanotubes on electrospun polymer films for flexible energy storage, Nanoscale. 10 (2018) 6005–6013. https://doi.org/10.1039/c8nr00313k.

[21] H. Tang, Q. Hu, M. Zheng, Y. Chi, X. Qin, H. Pang, Q. Xu, MXene–2D layered electrode materials for energy storage, Prog. Nat. Sci. Mater. Int. 28 (2018) 133–147. https://doi.org/10.1016/j.pnsc.2018.03.003.

[22] Y. Chen, H. Yang, Z. Han, Z. Bo, J. Yan, K. Cen, K.K. Ostrikov, MXene-Based Electrodes for Supercapacitor Energy Storage, Energy and Fuels. 36 (2022) 2390–2406.

https://doi.org/10.1021/acs.energyfuels.1c04104.

[23] L. Ma, D. Luo, Y. Li, X. Chen, K. Wu, J. Xu, Y. Cao, M. Luo, I. Manke, F. Lai, C. Yang, Z. Chen, Architecture design of MXene-based materials for sodium-chemistry based batteries, Nano Energy. 101 (2022) 107590. https://doi.org/10.1016/j.nanoen.2022.107590.

[24] M.R. Lukatskaya, O. Mashtalir, C.E. Ren, Y. Dall'Agnese, P. Rozier, P.L. Taberna, M. Naguib, P. Simon, M.W. Barsoum, Y. Gogotsi, Cation intercalation and high volumetric capacitance of two-dimensional titanium carbide, Science (80-.). 341 (2013) 1502–1505. https://doi.org/10.1126/science.1241488.

[25] M. Alhabeb, K. Maleski, B. Anasori, P. Lelyukh, L. Clark, S. Sin, Y. Gogotsi, Guidelines for Synthesis and Processing of Two-Dimensional Titanium Carbide ($Ti_3C_2T_x$ MXene), Chem. Mater. 29 (2017) 7633–7644. https://doi.org/10.1021/acs.chemmater.7b02847.

[26] M.A. Mohammadi, F.A. Tabar, A. Mohammadpour-Haratbar, A.M. Bazargan, S. Mazinani, A.H. Keihan, F. Sharif, Preparation and evaluation of electrospun carbon nanofibers infused by metal nanoparticles for supercapacitor electrodes application, Synth. Met. 274 (2021) 116706. https://doi.org/10.1016/j.synthmet.2021.116706.

[27] R. Vellacheri, V.K. Pillai, S. Kurungot, Hydrous RuO_2-carbon nanofiber electrodes with high mass and electrode-specific capacitance for efficient energy storage, Nanoscale. 4 (2012) 890–896. https://doi.org/10.1039/c2nr11479h.

[28] M.U. Rani, V. Naresh, D. Damodar, S. Muduli, S.K. Martha, A.S. Deshpande, In-situ formation of mesoporous SnO_2@C nanocomposite electrode for supercapacitors, Electrochim. Acta. 365 (2021). https://doi.org/10.1016/j.electacta.2020.137284.

[29] M. Aftabuzzaman, C.K. Kim, T. Kowalewski, K. Matyjaszewski, H.K. Kim, A facile route to well-dispersed Ru nanoparticles embedded in self-templated mesoporous carbons for high-performance supercapacitors, J. Mater. Chem. A. 7 (2019) 20208–20222. https://doi.org/10.1039/c9ta06571g.

[30] W. Xu, B. Xin, X. Yang, Carbonization of electrospun polyacrylonitrile (PAN)/cellulose nanofibril (CNF) hybrid membranes and its mechanism, Cellulose. 27 (2020) 3789–3804. https://doi.org/10.1007/s10570-020-03006-y.

[31] Y. Wang, X. Wu, Y. Han, T. Li, Flexible supercapacitor: Overview and outlooks, J. Energy Storage. 42 (2021) 103053. https://doi.org/10.1016/j.est.2021.103053.

[32] R. Vicentini, L.M. Da Silva, E.P. Cecilio, T.A. Alves, W.G. Nunes, H. Zanin, How to measure and calculate equivalent series resistance of electric double-layer capacitors,

Molecules. 24 (2019). https://doi.org/10.3390/molecules24081452.

[33] S. Jeon, J.H. Jeong, H. Yoo, H.K. Yu, B.H. Kim, M.H. Kim, RuO_2 Nanorods on Electrospun Carbon Nanofibers for Supercapacitors, ACS Appl. Nano Mater. 3 (2020) 3847–3858.

[34] G.H. An, H.J. Ahn, Surface modification of RuO_2 nanoparticles-carbon nanofiber composites for electrochemical capacitors, J. Electroanal. Chem. 744 (2015) 32–36. https://doi.org/10.1016/j.jelechem.2015.03.009.

[35] C.M. Chuang, C.W. Huang, H. Teng, J.M. Ting, Hydrothermally synthesized RuO_2/Carbon nanofibers composites for use in high-rate supercapacitor electrodes, Compos.Sci.Technol.72(2012)1524–1529. https://doi.org/10.1016/j.compscitech.2012.05.024.

[36] B.H. Kim, C.H. Kim, D.G. Lee, Mesopore-enriched activated carbon nanofiber web containing RuO_2 as electrode material for high-performance supercapacitors, J. Electroanal. Chem. 760 (2016) 64–70. https://doi.org/10.1016/j.jelechem.2015.12.001.

[37] J. Zhang, D. Jiang, B. Chen, J. Zhu, L. Jiang, H. Fang, Preparation and Electrochemistry of Hydrous Ruthenium Oxide/Active Carbon Electrode Materials for Supercapacitor, J. Electrochem. Soc. 148 (2001) A1362. https://doi.org/10.1149/1.1417976.

[38] J.M. Miller, B. Dunn, T.D. Tran, R.W. Pekala, Deposition of Ruthenium Nanoparticles on Carbon Aerogels for High Energy Density Supercapacitor Electrodes, J. Electrochem. Soc. 144 (1997) L309–L311. https://doi.org/10.1149/1.1838142.

[39] J.H. Jang, S. Han, T. Hyeon, S.M. Oh, Electrochemical capacitor performance of hydrous ruthenium oxide/mesoporous carbon composite electrodes, J. Power Sources. 123 (2003) 79–85. https://doi.org/10.1016/S0378-7753(03)00459-2.

[40] C. Lin, J.A. Ritter, B.N. Popov, Development of Carbon-Metal Oxide Supercapacitors from Sol-Gel Derived Carbon-Ruthenium Xerogels, J. Electrochem. Soc. 146 (1999) 3155–3160. https://doi.org/10.1149/1.1392448.

[41] X. He, K. Xie, R. Li, M. Wu, Microwave-assisted synthesis of Ru/mesoporous carbon compositesforsupercapacitors,Mater.Lett.115(2014)96–99. https://doi.org/10.1016/j.matlet.2013.10.033.

[42] T.N. Jebakumar Immanuel Edison, R. Atchudan, Y.R. Lee, Facile synthesis of carbon encapsulated RuO_2 nanorods for supercapacitor and electrocatalytic hydrogen evolution reaction,Int.J.HydrogenEnergy.44(2019)2323–2329. https://doi.org/10.1016/j.ijhydene.2018.02.018.

Chapter-III

Flexible Polyaniline/MXene/CNF Composite Nanofibrous Mats as Electrodes

3.1 Literature review

Batteries and supercapacitors offer excellent energy density and power density, respectively, and are widely accepted as energy storage devices for various applications. Although supercapacitors possess excellent power density and cyclic stability, their energy density is limited. Recent efforts have been made to enhance specific capacitance to develop supercapacitors suitable for applications requiring a high energy density. Furthermore, the energy storage devices were made flexible to satisfy the recent demand for flexible and foldable electronic devices. For flexible energy storage devices, symmetric supercapacitors were preferred instead of batteries since they require only one flexible electrode on both sides, whereas batteries require two different flexible electrodes. We need to develop an electrode with excellent specific surface area (SSA), virtuous pore size distribution, and electrical conductivity to develop a flexible supercapacitor suitable for high specific power density applications. For wearable flexible electronics, binders-free CNF-based electrodes are regarded as promising electrode resources due to its very high electrical conductivity, hefty electrode-electrolyte interface, and flexible nature. Additionally, it is less expensive than other carbon-based materials, such as graphene and its composites, allowing it to be produced in large quantities[1,2]. However, these CNF-based electrodes exhibit limited specific capacitance[3,4]. To improve the specific capacitance of these carbon fiber-based supercapacitors, metal (Ru, Mn, Fe, Co, etc.) oxides are often introduced into the carbon skeleton structure, which enhances the specific capacitance by faradic reaction-based charge storage[5–7]. Furthermore, electrospun fiber mats usually exhibit low strength due to their small fiber diameters and high porosity. Nonetheless, one effective approach to enhance their strength is by introducing a reinforcing agent into the mat, such as MXene or graphene. Another feasible strategy involves increasing the fiber diameter, which eventually improves the mechanical strength of the mat. In addition to these metal oxides, two-dimensional graphene and MXenes ($Ti_3C_2T_x$) were also embedded into the carbon fiber host to enhance electrochemical performance. Since 2011, MXene-based materials are extensively explored as electrochemical electrode material due to its hefty electrical conductivity, hydrophilicity, and excellent electrochemical properties. MXenes are usually embedded into carbon-based nanomaterials as they suffer from self-oxidation and layer restacking[8]. CNF electrodes embedded with delaminated MXene layers showed improved specific capacitance; the specific

capacitance increased twice when delaminated MXene layers were embedded into carbon fiber electrodes[9].

It is also possible to increase carbon-based electrodes' specific capacitance (energy density) by depositing conducting polymers (e.g., polyaniline (PANI)[10], polythiophene[11], polypyrrole[12], etc.) on them, with this conductive polymer addition carbon fiber electrodes' specific capacitance is improved by pseudocapacitive charge storage in multiple oxidation states. A variety of methods can be used to deposit conductive polymers, including hydrothermal deposition, self-assembly, electrodeposition, and polymerization[13]. Among these methods, polymerization is an easy one-step procedure for depositing conductive polymer[14]. As a conducting polymer, PANI offers many advantages over other polymers, including high conductivity and ease of processing, good environmental stability, and low cost. However, pristine PANI exhibits fragility behavior related to cross-linked structure, relatively low surface area, and limited stability due to significant volume changes through the moment of ions[15,16]. Due to this limitation, the integration of PANI within nanofibers becomes unfeasible, thereby preventing the occurrence of in-situ polymerization reactions inside the nanofiber. Consequently, the deposition of PANI nanoparticles can only be achieved on the outer surface of the CNF. The PANI-deposited PAN-derived CNFs demonstrated improved stability and electrochemical performance. The specific capacitance of 234 F g^{-1} was achieved plus excellent cyclic stability of 90% specific capacitance retention after 1000 cycles[17].

Essentially, two approaches were employed to enhance the specific capacitance of carbon-based electrodes: the first involves incorporating pseudocapacitive metal oxides, and the second involves conducting polymer layer deposition. About 10 % of pseudocapacitive materials were often incorporated into polymer precursors before carbonization to improve electrochemical performance. This is because embedding excess metal oxide/MXene impedes the electrospinning of polymer composite solution. In a few studies, to further improve the electrochemical performance of these binary composite carbon fibers, a conductive polymer layer was deposited over CNFs, or MXene was grafted over the nanofibers[18,19]. As far as we comprehend, there hasn't been any communicated research work on the synthesis of ternary composites incorporating MXene/metal oxide embedded carbon fiber as a core and an in-situ polymerized PANI layer as a shell.

In this study, we demonstrated a new strategy for synthesizing ternary composite flexible electrodes by choosing MXene with excellent conductivity and improved wettability as embedding material into core side polymer precursor and less expensive PANI as a conductive polymer for shell side layer to synthesize core-shell ternary composite nanofiber. The

synthesized ternary composite electrode unveiled C_{sp} of 356 F g^{-1} at 0.5 A g^{-1} of current density and capacitance retention of 91% after 5000 cycles. Additionally, this ternary composite electrode demonstrated a specific power density of 440 W kg^{-1} performance at a specific energy density of 30.5 W h kg^{-1}.

3.2. Experimental section

3.2.1. Chemicals

MAX phase titanium aluminum carbide (Ti_3AlC_2, 99%) was acquired from Aritech Chemazone Ltd., India. Polyacrylonitrile polymer (PAN) (Mw=150,000), Hydrochloric acid (HCl, 37%), Lithium fluoride (LiF, 98.5% powder), Ammonium persulfate (APS), and Aniline (≥99.5%) were supplied by Sigma Aldrich, India. Sulfuric acid (H_2SO_4, 98%) and N, N-Dimethylformamide (DMF, 99%) were procured from Finar Chemical Co. Ltd., India. Glass microfiber filter (Whatman-0.45 micrometer pore size). There was no purification prior to use of the chemicals, which were analytical grade chemicals.

3.2.2. Synthesis of delaminated MXene $Ti_3C_2T_x$ layers

The delamination of MXene sheets was achieved with selective etching of Al elements from the Ti_3AlC_2 , as reported elsewhere[20]. Initially, 20 mL of 9 molar of HCl solution in a Teflon reagent reactor by following adding 1 g of LiF powder was mixed with safety precautions and stirred for 5 minutes. Later, 1 g of Ti_3AlC_2 was steadily added to the above mixture solution. The resultant blend was maintained at temperature of 35˚C for 24 hours in a closed fume hood. Then, the achieved colloidal MXene solution was centrifuged at 3500 rpm for 5 minutes duration. Then, it was continually splashed with double distilled water 6-7 times until its pH value spread neutral. Further, the neutralized MXene suspension was ultra-sonicated in nitrogen atmosphere for 2 hours, afterwards centrifugation at 3500 rpm for 1 hour to achieve the MXene delaminated layers.

3.2.3. Preparation of flexible PANI/MXene/CNF electrode

PAN solution (9 wt.%) was prepared with delaminated MXene nanosheets (12 mg/mL) dispersed in DMF solution as a solvent. At room temperature, the mixture of PAN and DMF dispersed solvents was stirred overnight until PAN polymer was completely dissolved. An electrospinning apparatus (Physics Equipment Co., Espin Nano) was used to produce the nanofibrous membrane from the precursor solution. The operating parameters optimized in order to obtain uniform long nanofibers as follows: potential difference 15 kV, 12 cm of

distance from the syringe needle tip to collector drum, and the polymer flow rate 1 ml h^{-1}. The obtained nanofibers mat was annealed at 235 °C in air oxidative stabilization atmosphere followed by carbonization at 900 °C at a 4 °C min^{-1} heating ramp in nitrogen atmosphere to form MXene/CNF mat. Annealing at 235 °C in an air-oxidative environment can enhance the flexibility of the final carbon nanofiber composite and also electrical conductivity of the materials. It promotes structural stability and removes any residual stresses within the material and above this value material will decompose into CO2 and carbon monoxide. Carbonizing at 900 °C in a nitrogen atmosphere process can optimize the pore structure, leading to better ion transport and storage capabilities. For MXene/CNF and PANI/MXene/CNF mats, these processes are expected to improve the specific capacitance, energy density, and power density of the supercapacitors. Further, in order to prepare the flexible and binder-free PANI/MXene/CNF composite electrode, MXene/CNF mat was added to 0.5 M aniline/HCl solution and agitated for 60 minutes followed by the slow addition of 0.2 M APS/HCl solution to the above mixture. In polymerization process temperature was fixed at 0 °C and polymerization time duration was varied as 2 hours, 4 hours, and 8 hours to control the shell side conductive polymer layer thickness. As a result of in-situ polymerization of PANI for 2, 4, and 8 hours, samples coated with PANI were found to have a loading of 5 wt.%, 13.3 wt.%, and 24 wt.% PANI and were regarded as PANI/MXene/CNF-1, PANI/MXene/CNF-2, and PANI/MXene/CNF-3, respectively. To prevent excess volume expansions and capacity fade over cycling, we limited PANI loading to 25 wt.%. Prior to their use as electrodes, these composite nanofibers were cleaned with water and ethanol. A schematic depiction of the synthesis procedure for the flexible PANI/MXene/CNF ternary composite electrode is shown in Fig.3.1.

3.2.4. Structural characterization

In order to investigate the surface morphology and elemental composition of the composite nanofibers, field emission scanning electron microscopy (FESEM, Zeiss Gemini SEM) was coupled by energy dispersive X-ray spectroscopy (EDS). To improve the electrical conductivity of the sample, gold was sputtered on it. The molecular vibrations of electrode material were investigated using infrared spectra recorded with support of KBr pellets in between the wavelength range of 350-4000 cm^{-1} with a Fourier transform infrared spectrometer (FTIR, PerkinElmer 100). X-ray diffractometer (PANalytical, X'Pert Powder XRD) was used to measure crystallinity at Cu Kα X-ray radiation in the 2-theta choice of 6-75º at 40 mA and

40 kV with a scan rate of 2° per minute. Chemical composition of samples was characterized using XPS (X-ray photoelectron spectrometer (ESCALAB Thermo-Scientific 250Xi) included with X-ray source of Al Kα. BET pore volume and surface Area analyzer (Quanta chrome Autosorb) is an equipment to measure the SSA of nanofibers, which is expressed in $m^2 g^{-1}$. A contact angle goniometer (Biolin, Attension Theta) was used to measure the static water contact angles (CA) of the composites.

3.3. Results and discussion

3.3.1. Structural analysis composite materials

3.3.1.1 XRD analysis of PANI/MXene/CNF-1,2,3 and MXene/CNF

The XRD patterns of the CNF, MXene/CNF and PANI/MXene/CNF composites depicted in Fig. 3.2(a) exhibit multiple distinctive sharp and clear diffraction peaks at the 2-theta value of 6.6°, 42.7°, and 49.6°, corresponding to the diffraction of MXene planes of (002), (121) and (111) respectively[9]. There is also a broad diffraction peak at 2-theta of 26.3°, which is a common feature of all diffraction patterns, an indication of the amorphous nature of CNF[22]. With excess PANI deposition, however, diffraction peaks become broad and week, indicating PANI has a broad, low-intensity amorphous peak[23]. Further, few peaks disappear in the PANI/MXene/CNF-3 diffraction pattern it could be attributed to the even deposition of PANI over the nanofibers[18].

3.3.1.2 FTIR analysis of PANI/MXene/CNF-1,2,3 and MXene/CNF

A comparison of FTIR spectra of PANI/MXene/CNF-1,2,3 composites and MXene/CNF composite formed over a range of polymerization durations can be seen in Fig.3.2(b). FTIR spectrum of the PANI/MXene/CNF-1,2,3 composites and MXene/CNF composite showed a common remarkable absorption peak at 1690 cm^{-1}, it could be accredited to aromatic stretching of C=C[24]. In addition, all IR spectra show absorption peaks at 3415 cm^{-1} and 1190 cm^{-1} associated with the stretch of the O-H in the water molecule and the C=N (quinoid) stretching vibration[25]. The PANI/MXene/CNF ternary composites exhibited a weak absorption band at 3230 cm^{-1} allocated to $–NH^{2+}$ stretching which occurs due to the protonation of PANI[25]. The ternary composite with PANI also exhibited peaks near 1487 cm^{-1} and 814 cm^{-1} could be ascribed to C=C of benzenoid rings stretching vibrations and out-of-the-plane vibrations of C-H at C1 and C4 in the benzene ring[26–28]. The $–NH^{2+}$ and out-of-the-plane C-H vibrations confirm the grafting of PANI over binary MXene/CNF composites.

3.3.1.3 FESEM analysis of PANI/MXene/CNF-1,2,3 and MXene/CNF

FESEM was used to characterize the microstructures and surface morphologies of electrospun PANI/MXene/CNF-1,2,3 composites and MXene/CNFs composite. Fig.3.3(a) and 4.3(b) be evidence for the FESEM images of the MXene/CNF composite, displaying a homogeneous, continuous and entanglement nanofibrous morphology with a fiber diameter of 200 ±15 nm. The elemental mapping and FESEM images of binary composite are shown in Fig.3.3(c). The EDX analysis of MXene/CNF binary composite sample demonstrate the homogeneous distribution of carbon, nitrogen, and, titanium as shown in Fig.3.3(c). Fig.3.4(a), 3.4(c), and 3.4(e) depict low magnification images of PANI/MXene/CNF-1,2, and 3, respectively. While images displayed in Fig.3.4(b), 3.4(d), and 3.4(f) correspond to the higher magnification of PANI/MXene/CNF composites. All FESEM images of ternary composites reported here reveal in situ polymerization of aniline monomer into dense and uniform thorn-like PANI nanopits on the surface of MXene/CNFs. The higher-resolution FESEM images also reveal that PANI nanopits are sized in the range of 30-60 nm. The diameter of MXene/CNF progressively increased with increase in PANI content, these densely deposited PANI interconnected nanopits increase the surface area, roughness and electrode and electrolyte interface. Observations of the morphology analysis indicate that polymerization of PANI on MXene/CNF increases the average fiber diameter to 510 ± 26 nm. Fig.3.5(a) illustrates the average diameter distribution of fibers for binary composite and ternary composites with PANI deposition for different polymerization durations.

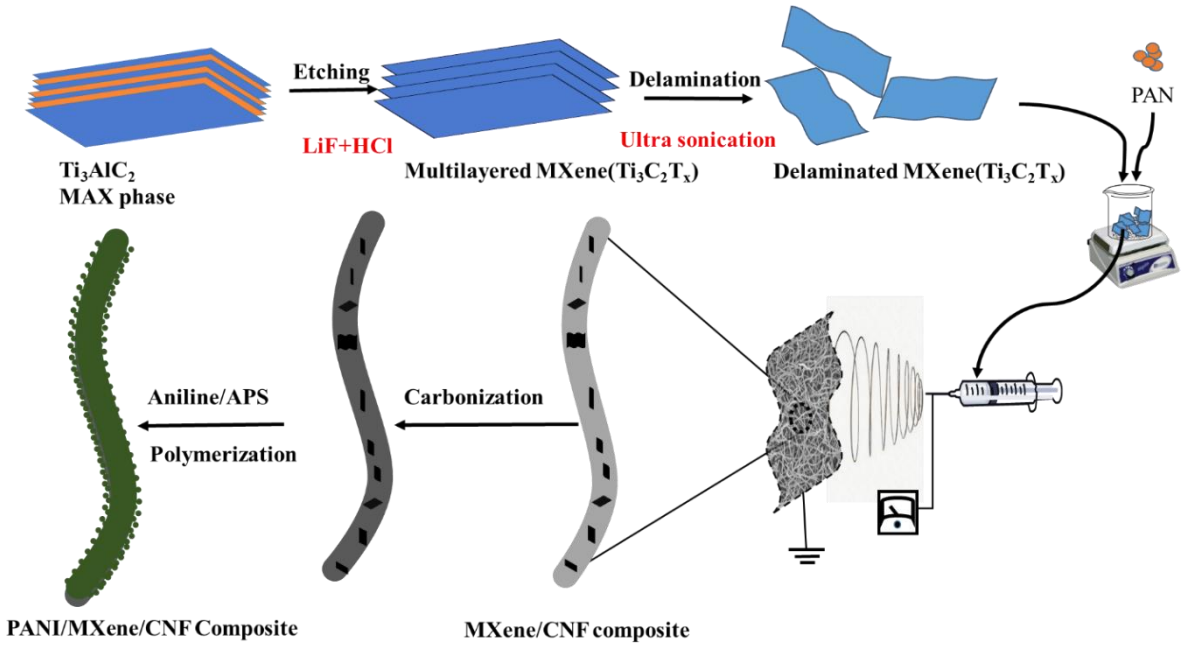

Figure 3.1 Schematic representation of the synthesis of ternary composites based on PANI, MXene, and CNF

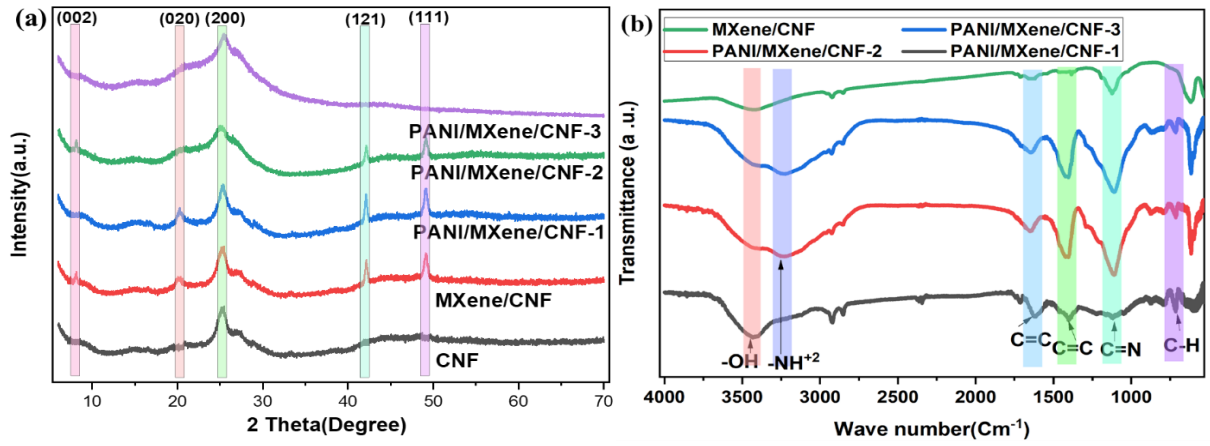

Figure 3.2 (a) XRD spectra of MXene/CNF and PANI/MXene/CNF composites, and (b) FTIR absorption spectrum of MXene/CNF and PANI/MXene/CNF composites

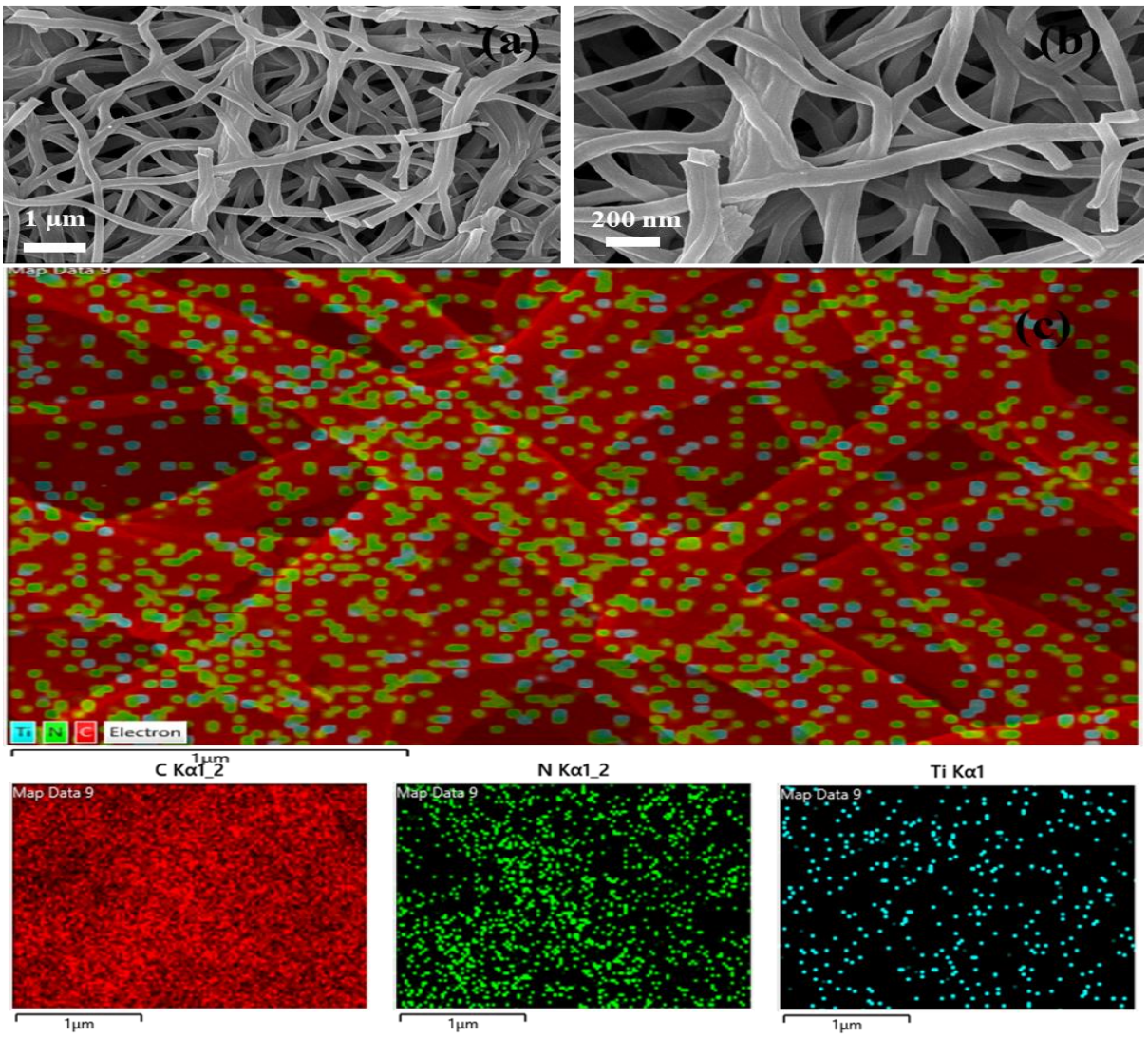

Figure 3.3 (a) FESEM images of (a) MXene/CNF composite at lower magnification and (b) at higher magnification; (c) EDX of MXene/CNF composite and corresponding element mapping images for the carbon, nitrogen, and titanium

3.3.1.4 BET analysis of PANI/MXene/CNF-1,2,3 and MXene/CNF

BET surface analysis was used to assess the SSA of the MXene/CNF composite before and after PANI polymerization deposition, and the corresponding nitrogen adsorption-desorption isotherms were shown in Fig.3.5(b). As P/P_0 values ranging from 0.01-1, the nitrogen adsorption on the PANI/MXene/CNF composite progressively rises with increasing relative pressure (P/P_0). The curve largely resembles an isothermal type II curve. The ternary composite exhibited a greater positive slope when compared with MXene/CNF composite[29]. The binary composite N_2 adsorption curve soon reached saturation levels next to relative pressure (P/P_0) <0.1, showing that the MXene/CNF mat surfaces comprise a considerable amount of micropores. The ternary composite exhibited SSA of 375 $m^2 g^{-1}$, more than double the binary composite electrode surface area (167 $m^2 g^{-1}$) without PANI deposition. This can be attributed to the deposition of fin-like nanopits on the surface of binary composite fibers. This further increases fiber diameter, surface area, and surface roughness[30,31]. The distribution of pore sizes for MXene/CNF composites with and without PANI deposition is shown in Fig.3.5(c). The pores in all samples are mostly micropores with a diameter of ~2 nm, and a minor section of them are mesopores within a diameter of 5 ~ 20 nm. PANI/MXene/CNF-3 has the greatest ample pore volume at diameter of 2 nm, 0.28 $cm^3 g^{-1}$ (vs. 0.20 $cm^3 g^{-1}$ for MXene/CNF). The porous structure may lessen the diffusion distance of ions and upsurges the contact area between the active electrode surface and electrolyte, which will be valuable for electrochemical charge storage[10,32]. The effect of sonication time during the synthesis of PANI/MXene/CNF and PANI nanocrystals plays a crucial role in determining their properties. The impact of sonication time on crystallinity and crystallite size. Sonication involves applying ultrasonic waves to a sample, leading to the crystallinity of PANI/MXene/CNF can be influenced by sonication time. Short sonication e.g., 0.5–2 hours limited impact on crystallinity. Prolonged sonication e.g., >2 hours excessive kinetic energy from collapsing cavitation bubbles can lead to disintegration or deformation of components. Longer sonication times can lead to smaller crystallite sizes due to increased fragmentation. The desired crystallite size depends on the specific application e.g., charge storage capacity. Optimization involves finding the sweet spot where crystallite size is small enough for enhanced properties but not too small to compromise performance, we found the optimum value of sonication time PANI deposition is 8 hours.

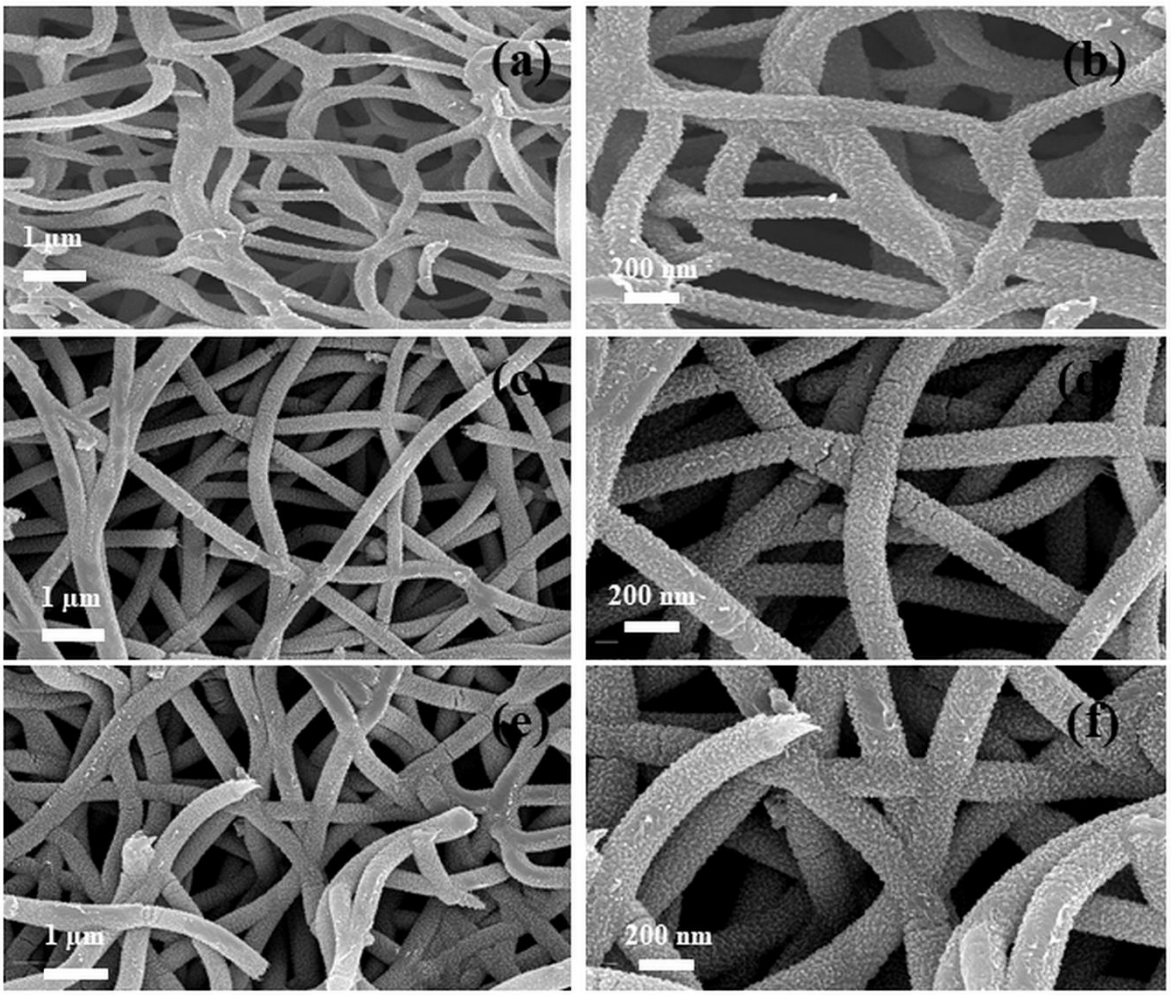

Figure 3.4 SEM images of (a, c, e) PANI/MXene/CNF ternary composite at low magnification and (b,d ,f) PANI/MXene/CNF ternary composite at high magnification. (g) TEM of Core and Shell structure of PANI and MXene/CNF (h) HRTEM image of Delaminated MXene layers in Ternary composite.

3.3.1.5 XPS analysis of PANI/MXene/CNF-1,2,3 and MXene/CNF

We performed XPS analysis to govern the chemical conformation and to confirm the removal of Aluminum element from the Ti_3AlC_2 to form delaminated MXene. Survey spectra analysis of the PANI/MXene/CNF composites confirmed the occurrence of four elements such as N, O, C and Ti, as shown in Fig.3.6(a). The C 1s, N 1s, and Ti 2p peaks were deconvoluted in order to determine the state of oxidation of these compounds. The higher-resolution spectrum of C 1s is deconvoluted into four Gaussian decomposed peaks with binding energies of 287.0 eV (C=O) ,286.9 eV (C-O/C-N) ,285.1 eV (C-C) and 284.8 eV (C=C), and as shown in Fig.3.6(b)[33,34]. The higher-resolution Ti 2p spectrum is shown in Fig. 3.6(c), demonstrating two conspicuous peaks, Ti $2p_{1/2}$ and Ti $2p_{3/2}$, and their analogous satellite peaks which confirm the presence of both Ti^{3+} and Ti^{2+} oxidation states[30,35]. The peaks of 2 $p_{1/2}$ at 455.8 and 462

eV, however, belong to Ti^{3+} and Ti^{2+}, respectively. Further, the N 1s core level spectra was deconvoluted into three distinct peak positions at 383.5 eV (-NH-), 382.8 eV ($-NH_2$), and 382.5 eV (=N-), as shown in Fig.3.6(d) and the appearance of the C–N bond confirms the existence of PANI[32,36,37].

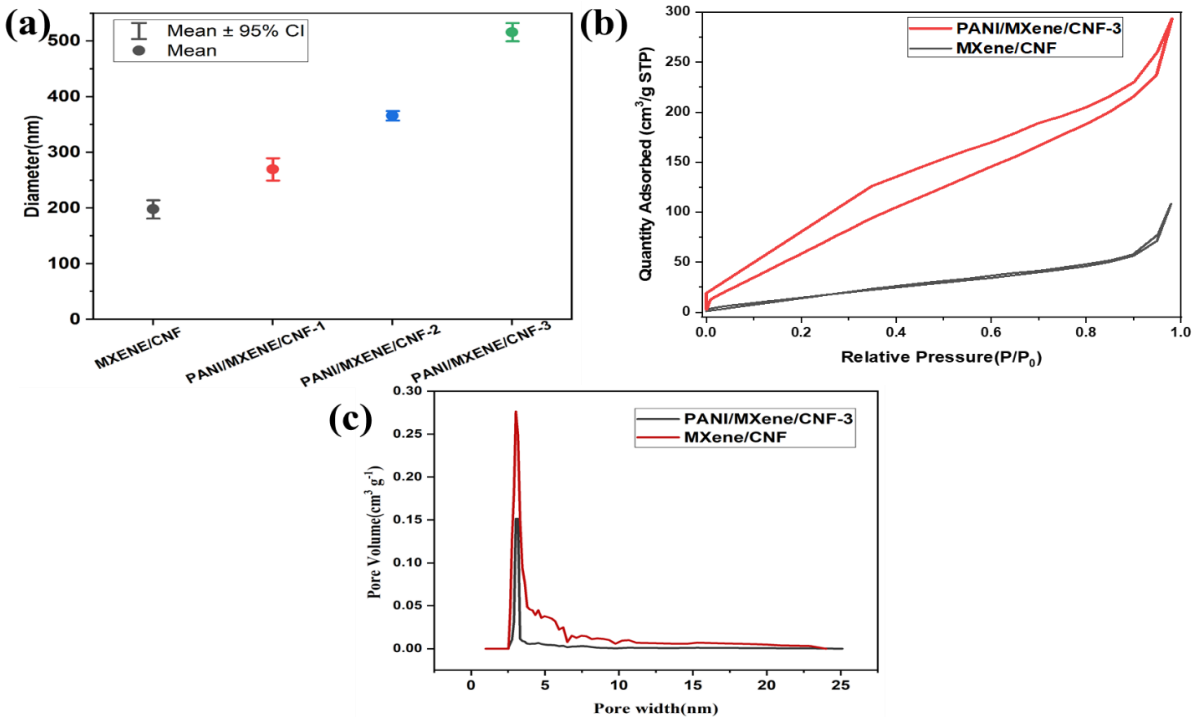

Figure 3.5 (a) Average fiber diameter of binary and ternary composites with varying polymerization time; (b) Nitrogen adsorption/desorption isotherms of ternary and binary composites; (c) Pore size distribution of ternary composite and binary composites.

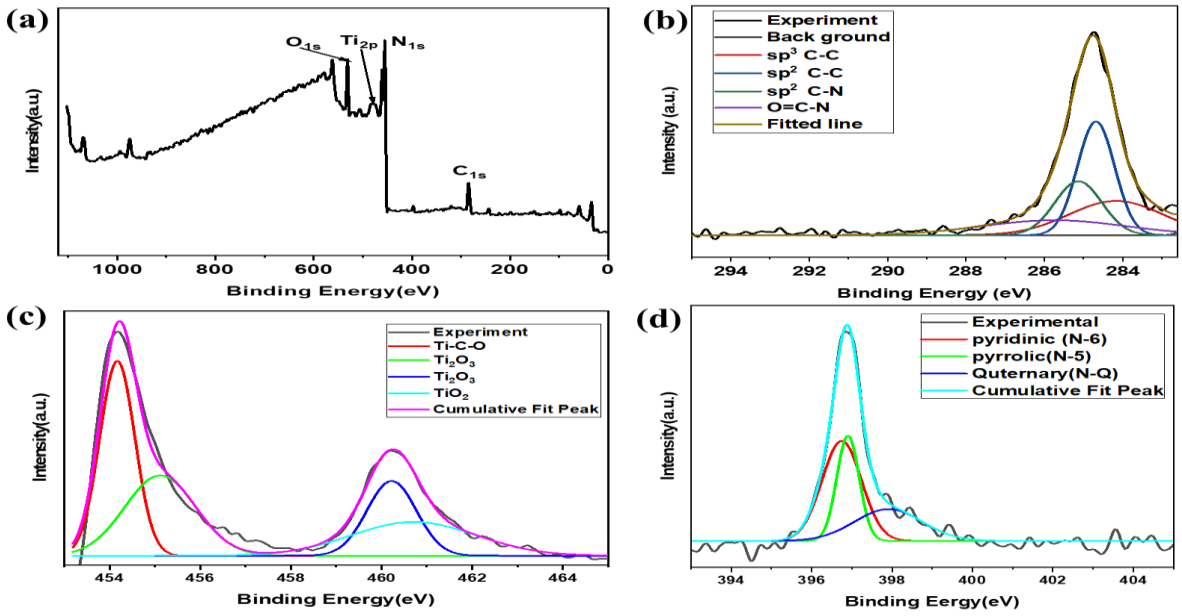

Figure 3.6 High resolution core level XPS of (a) survey spectra, (b) C 1s, (c) Ti 2p and (d) N 1s of PANI/MXene/CNF-3 composite

3.3.1.6 Water contact angle analysis of PANI/MXene/CNF-1,2,3 and MXene/CNF

We investigated the surface-wetting properties of the prepared samples by measuring their water contact angles (CAs). There is generally a strong correlation between the CA of the surface and its chemical nature. Fig.3.7 shows digital images of water CA for PAN derived CNF mat composites of MXene/CNF and PANI/MXene/CNF. A dynamic contact angle was measured in less than 0.2 seconds for PANI/MXene/CNF composites, as shown in Fig.3.7 (c-e). PAN derived CNF and MXene/CNF composite mats showed hydrophobic nature with the water CA of 126˚±1.6˚ and 117˚±2.2˚, respectively, whereas, PANI deposition to prepare PANI/MXene/CNF composites altered the wettability from hydrophobic to hydrophilic and showed a water CA of 0˚. This significant change in wettability is due to the surface functional groups of PANI and surface roughness[24]. Change in wettability from hydrophobic to hydrophilic influences electrochemical performance by increasing aqueous electrolyte uptake.

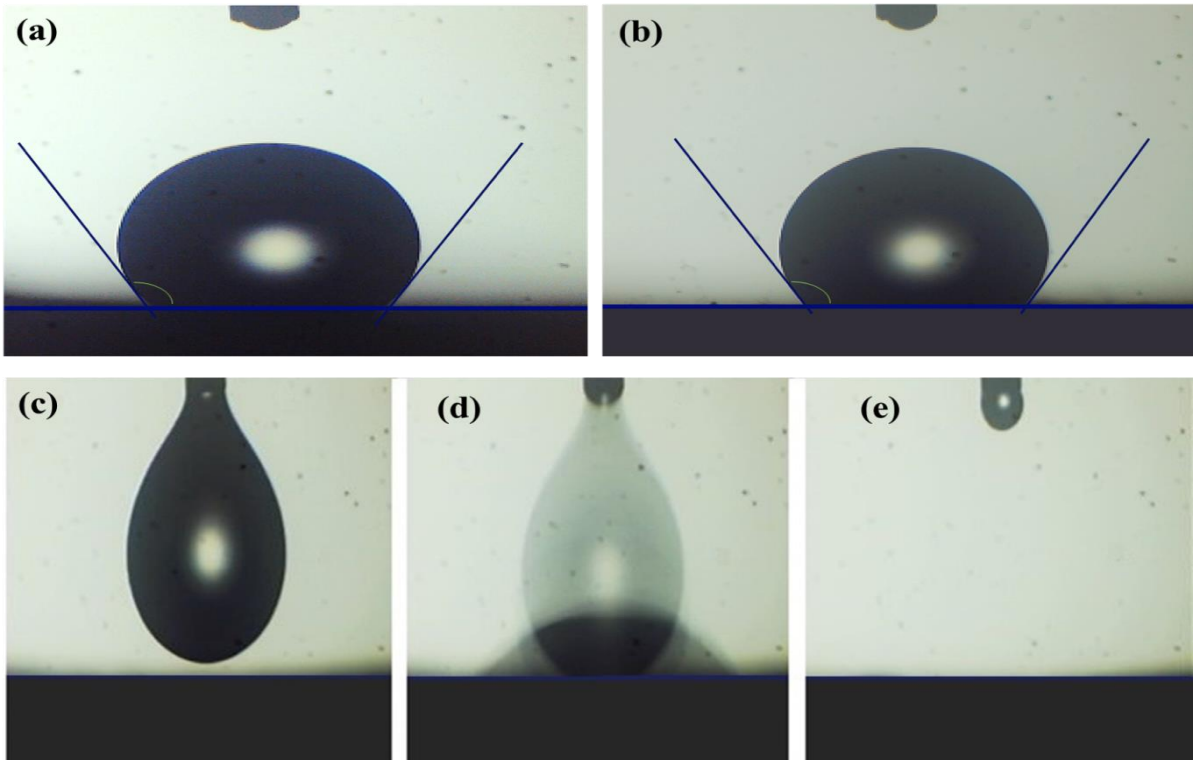

Figure 3.7 Digital images of contact angle measurements on the surface of (a) PAN derived CNF; (b) MXene/CNF composite and (c-e) dynamic contact angle of PANI/MXene/CNF composite

3.3.2. Electrochemical characterization of PANI/MXene/CNF-1,2,3 composite electrodes

3.3.2.1. Cyclic voltammetry analysis of PANI/MXene/CNF-1,2,3 and MXene/CNF nanocomposite electrode: The electrochemical performance of flexible binder-free binary and ternary electrodes for symmetric supercapacitors was examined to determine the influence of surface morphology, surface area, and wettability. Fig.3.8(a) shows the CV curves for CNF and MXene/CNF and PANI/MXene/CNF-3 composites and Fig.3.8(b) depicts the CV curves of the ternary composite and the binary composite electrodes recorded at a scan rate of 5 mV s^{-1}. The pristine CNF and binary composite electrode displayed the typical double-layer capacitive charge storage curve without oxidation or reduction peaks. Then again, the CV curve behavior of the ternary composite electrode showed faradaic reaction peaks, confirming its pseudocapacitive charge storage due to PANI addition. The CV curves of ternary composite electrodes make it clear that they have a higher specific capacitance value than binary composite electrodes. PANI/MXene/CNF-3 electrode with maximum PANI deposition displayed the largest area under the CV curve out of all the synthesized electrodes. In addition to the enhanced surface area, pseudocapacitive charge storage can be attributed to this. The CV of PANI/MXene/CNF-3 electrodes were also recorded at different scan rates, as shown in Fig.3.8(c). In response to the increased scan rate, the anodic (oxidation) and cathodic(reduction) peak points relocated towards higher and lower voltage range, respectively, due to electrode polarization[38]. As the scan rate increases, the capacitive current density increases, indicating a promising reversible behavior of the fast charge-discharge progression. Almost at all scan rates, the CV curves exhibited a quasi-rectangular shape, which indicates an electrode with good capacitive behavior. GCD measures the charge and discharge behavior of an electrochemical system at a constant current. It provides information about energy storage and power delivery.CV provides information about the capacitive behavior over a range of potentials. GCD focuses on the dynamic charge-discharge process. Specific capacitance values from both methods are consistent from that we can say that system behaves ideally. We compared the specific capacitance values at CV at 5 mV/s and GCD at 1 A/g are consistent.

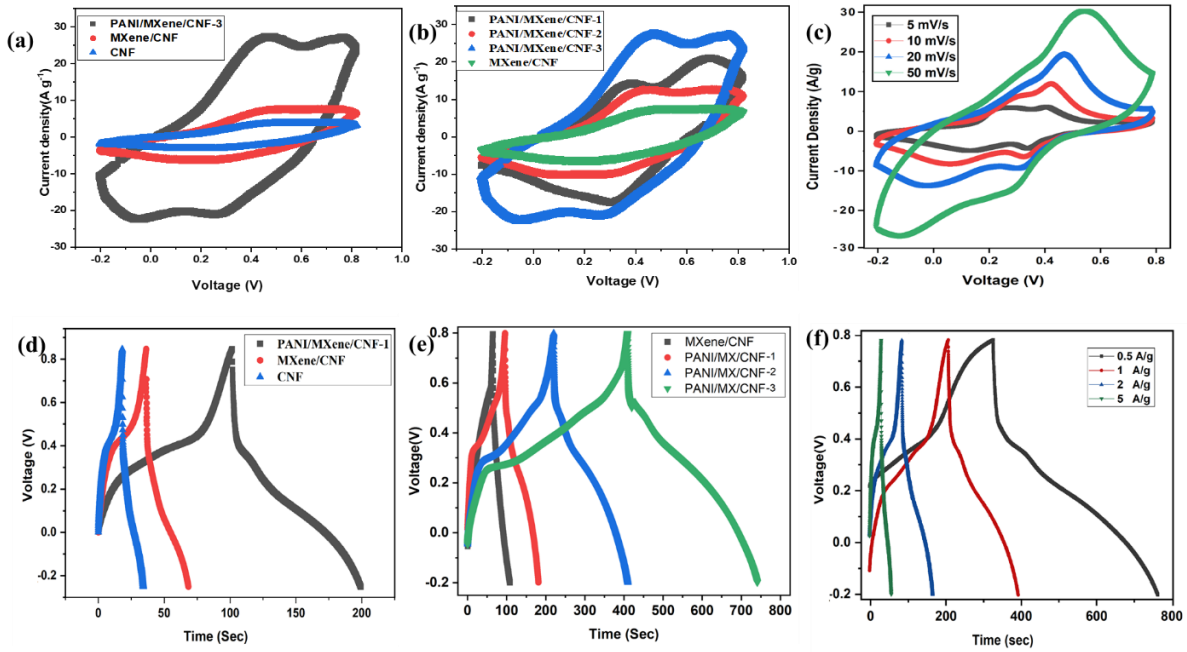

Figure 3.8 Electrochemical performance of composite electrodes (a) CV curves for CNF, MXene/CNF and PANI/MXene/CNF-3 composites at 5 mV s^{-1} scan rate (b) CV curves for MXene/CNF and PANI/MXene/CNF-1,2,3 composites at 5 mV s^{-1} scan rate (c) CV curves at different current density for PANI/MXene/CNF-3 composite (d) GCD curves of CNF, MXene/CNF and PANI/MXene/CNF-1 composites at 0.5 A g^{-1} (e) GCD curves of MXene/CNF and PANI/MXene/CNF-1, 2, 3 composites at 0.5 A g^{-1} (f) GCD curves at different current density for PANI/MXene/CNF-3 composite.

3.3.2.2 GCD analysis of PANI/MXene/CNF-1,2,3 and MXene/CNF nanocomposite electrodes

GCD experiments were performed to evaluate the electrodes' performance by specific capacitance, cyclic stability, and coulombic efficiency. Pristine CNF, MXene/CNF, PANI/MXene/CNF-1,2 and 3 electrodes GCD experiments were conducted at a current density of 0.5 A g^{-1}. Fig.3.8(d) demonstrations the GCD curves of pristine CNF and binary and ternary composite electrodes and Fig.3.8(e) shows the comparison of binary and ternary composites. The pristine CNF, binary electrode showed symmetrical and straight GCD curves, suggesting high reversibility and double-layer capacitive storage. The GCD curve of a ternary composite electrode differs from a traditional triangle shape due to the faradic reaction between PANI and electrolyte (pseudocapacitive storage behavior of PANI). The specific capacitance values of the pristine CNF, binary composite electrode was estimated as 102,144 F g^{-1} and ternary composite electrodes with polymerization time durations of 2 hours, 4 hours, and 8 hours exhibited

enhanced capacitances of 255, 301, and 356 F g^{-1}, respectively. The specific capacitance values of a ternary composite electrode increased with increasing polymerization time (or PANI loading), as shown in Fig. 3.8(f). The cause of this can be attributed to augmented loading of PANI over the binary composite fiber and increased surface area as evaluated using SEM and BET analysis. This improved specific capacitance can also be attributed to the improved wettability between the electrolyte and microporous electrode, lower charge transfer resistance and shorter diffusion length. The rate performance of PANI/MXene/CNF-1,2,3 and MXene/CNF electrodes at various current densities is also presented in Fig.3.9(a). The specific capacitance values for the PANI/MXene/CNF-3 decreased from 356 F g^{-1} to 260 F g^{-1}, as the current density value increased from 0.5 A g^{-1} to 2 A g^{-1}. However, the specific capacitance value of the ternary composite electrode with 8-hour deposition remained maximum at all current densities. Furthermore, the binder free PANI/MXene/CNF-3 composite electrode experiences a relatively low capacitance fade (9%) contrasted to 20%, 17%, and 12% for flexible binder-free MXene/CNF, PANI/MXene/CNF-1,2 electrodes respectively, as the current densities parameter increased from 0.5 to 5 A g^{-1}. The electrochemical performance of the prepared electrodes is compared with the various PANI based carbon nanofiber composite electrode materials from the literature reports are stated in Table.1. The performance of the ternary composite is superior to most of the PANI composite fibers, and at the initial cycle is comparable to the PANI/CNF composite electrode, but cyclic stability is much better as our ternary composite shows 91% retention after 5000 cycles compared to 90% retention after 1000 cycles for PANI/CNF composite.

Table 3.1 Electrochemical performance comparison for various PANI based composite electrode for supercapacitor

Electrode composite material	Electrolyte/ Molarity	Specific capacitance (F g^{-1}) at current density	Energy density (Wh /Power density (W kg^{-1})	Capacitance Retention % (cycles)
PANI@CNF[17]	H_2SO_4 / 1 M	234 @ 1 A g^{-1}	32 @ 500	90% (1000)
PANI@CNF[24]	HClO4/ 1 M	220 @ 2 A g^{-1}	-	83% (1000)
PANI@CNF[39]	Li_2SO_4/ 1 M	320 @ 20 mV s^{-1}	23 @ 5000	74% (4500)
PANI@CNF@CNT[40]	H_2SO_4/ 1 M	315 @ 1 A g^{-1}	5.1 @ 10100	92% (10000)
PANI/MXene/CNF-3	H_2SO_4/ 1 M	356 @ 1 A g^{-1}	30.5 @ 440	91 % (5000 cycles)

3.3.2.3 Electrochemical Impedance spectroscopy analysis of PANI/MXene/CNF-1,2,3 and MXene/CNF nanocomposite Electrodes: An EIS study was conducted on PANI/MXene/CNF composites and MXene/CNF composite electrodes; Nyquist plots were presented in Fig.3.8(b). The inset of the plot Fig.3.9(b), shows the high-frequency region impendence behavior, and the starting point (intersection point) of the semicircle on the real axis corresponds to solution resistance (R_s). The solution resistance (R_s) did not differ notably because of 1 molar H_2SO_4 was exercised as electrolyte in all the electrode cells. Further, in high frequency region, the value of semi-circle diameter links to electrode's charge transfer resistance (R_{ct}). The R_{ct} in a solution medium can affect the mobility of ions in the solution, as it can limit the rate at which ions can be transported to the electrode surface. This can result in slower charge/discharge rates and reduced capacity in electrochemical devices this can be varied with amount of PANI deposition. The ternary composite with maximum PANI deposition showed the lowest charge transfer resistance due to increase in conductivity due to PANI deposition. The charge transfer resistances of MXene/CNF, PANI/MXene/CNF-1, 2, and 3 composite electrodes were 5.8, 4.5, 3.2, and 2.2 ohms, respectively. The significantly smaller R_{ct} of PANI/MXene/CNF-3 than that of other composites can be accredited to its intense meso-porous structure, with a considerable higher SSA and added reactive sites, which is more advantageous for diffusional behavior of electrolyte ions. The PANI/MXene/CNF composite core-shell configuration with linked conductive MXene/CNF intersections (bridge to join distinct nanofibers) enhanced interfacial charge transfer and therefore improved faradaic redox reactions. In the low-frequency zone, the straight line slope for PANI/MXene/CNF-3 composites was considerably steeper, in other words, since steeper the slopes leads to faster ion diffusion, and therefore, PANI contributing to MXene/CNF improving capacitance, indicating ideal capacitor behavior and the low ionic transfer resistance signifying better admittance of electrolyte ions onto the electrode surface[17]. This is in line with the to the PANI graphene/carbon nanoparticle based electrode reported[41]. The cyclic stability of the MXene/CNF composite was evaluated at a current density of 1 A/g from the curve shown in Figure 3.9 c. The cyclic life capacitance retentions of MXene/CNF fabricated electrode showed excellent cyclic stability. Initially, it can be seen that the cyclic coulombic efficiency decreases to 100 % until 4000 cycles. However, coulombic efficiency remains about 115 % after 5000 cycles than the initial cycle. A repeated charge-discharge process will definitely lead to mechanical and electrical faults that diminishing the initial performance attributed to the loss of mass of active material. The reactions are fully reversing then there should not be any drop, however, many factors affecting on reactions and surface stability of electrodes. Hence with cycle, the device is not coming back to initial stage that will lead to increase in performance .

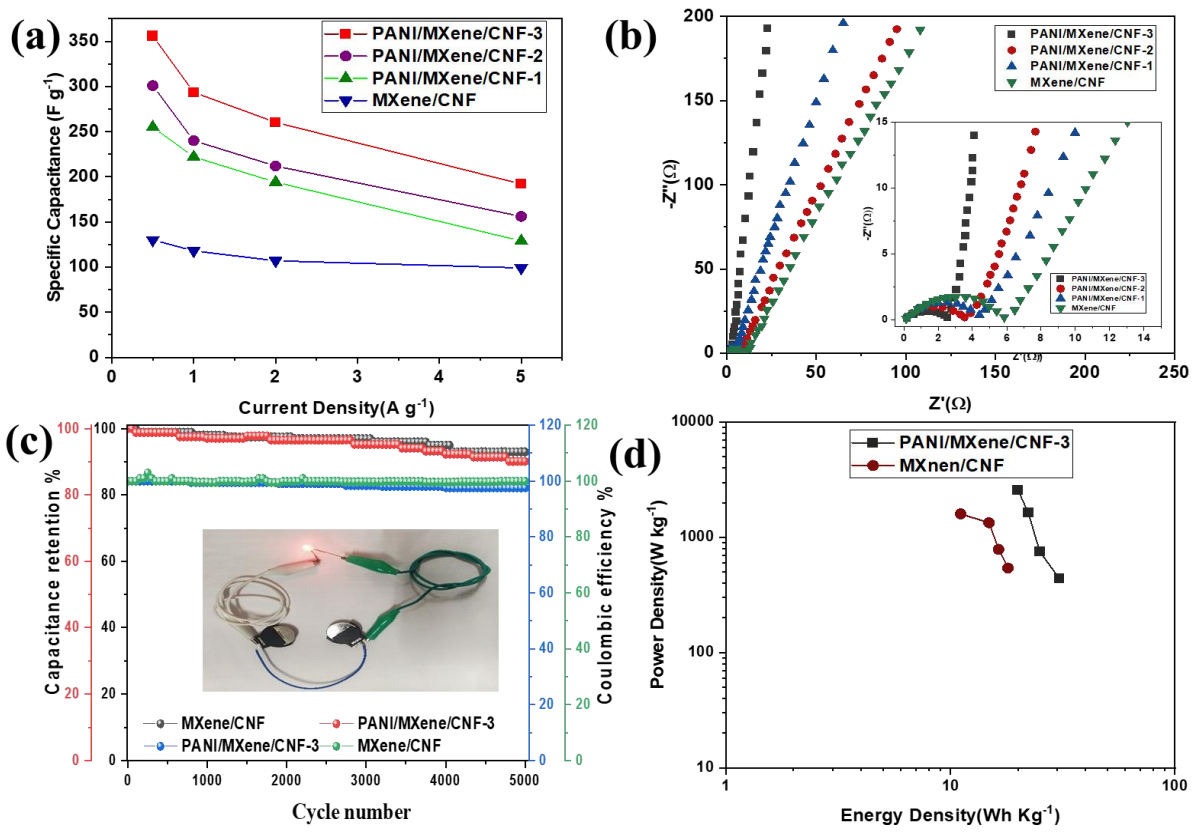

Figure 3.9 (a) Rate performance of binary and ternary composites at different current densities; (b) Nyquist plots of all electrodes-based supercapacitors (c) Cyclic stability (capacitance retention%) and coulombic efficiency of the ternary and binary at 1 A g^{-1} (d) Ragone plots for the different MXene/CNF and PANI/MXene/CNF-3.

The cyclic stability of ternary and binary composite electrodes was investigated by charging and discharging operation for the symmetric cell at current density of 1 A g^{-1}. Fig.3.9(c) illustrates the capacitance retention % and coulombic efficiency behavior of binder free flexible binary and ternary composite electrodes. The capacitance retention is of 91 % after 5000 cycles for ternary composite. Comparatively, the binary composite electrode showed a little better capacitance retention of (93 %) but lower specific capacitance. Moreover, it shows a great coulombic efficiency over 95% through the cycling test. Furthermore, an improved rate performance was accomplished for binder free flexible PANI/MXene/CNF-3 composite electrodes compared to binary composite electrode. Fig.3.9(d) shows Ragone plots for flexible MXene/CNF, PANI/MXene/CNF-1,2, and 3. Compared with MXene/CNF composite electrode's specific power density performance of 198 W kg^{-1} at specific energy density of 13 W h kg^{-1}, the flexible ternary composite electrode with 8 hours of polymerization time exhibited 440 W kg^{-1} power density at 30.5 W h kg^{-1} of energy density. An image of the

symmetric coin cell supercapacitor lighting a LED is shown in the inset of the Fig.3.8(c). Additionally, we have investigated the flexibility of the fabricated ternary electrode by bending and folding it as shown in Fig.3.10. The dark green (blackish) mat obtained by depositing PANI showed good resilience to bending and folding. Therefore, ternary composite electrodes can be used as binder free electrode material for flexible symmetric supercapacitors.

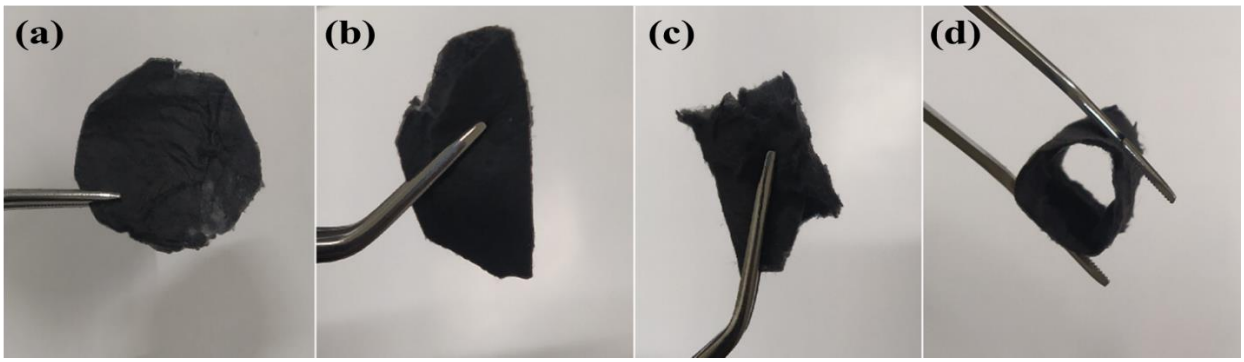

Figure 3.10 digital images PANI/MXene/CNF-3 Composite (a) flat, (b) bent, and (c-d) rolled

3.4 Conclusion

In summary, flexible binder-free binary (MXene/CNF) and ternary (PANI/MXene/CNF) composite electrodes were synthesized through electrospinning and subsequent in-situ process of polymerization. Ternary electrodes deposited with PANI showed increased fiber diameter, surface area, and wettability. Among ternary and binary composites, the ternary composite with 8-hour PANI deposition demonstrated great specific capacitance (356 F g^{-1}) and limited capacitance fade over 5000 cycles. The ternary composite electrode also unveiled excellent energy density, power density, coulombic efficiency, and good flexibility. This excellent performance is attributed to embedding two-dimensional MXene into the CNF, enhanced wettability, and micropore volume. These results indicate that PANI/MXene/CNF composite electrodes have great potential as flexible electrodes for high-performance supercapacitors.

3.5 References

[1] M.M. Atta, R.A. Fahim, Flexible and wearable supercapacitors: A short review, J. Energy Storage. 44 (2021) 103475. https://doi.org/10.1016/j.est.2021.103475.

[2] C.V.V. Muralee Gopi, R. Vinodh, S. Sambasivam, I.M. Obaidat, H.J. Kim, Recent progress of advanced energy storage materials for flexible and wearable supercapacitor: From design anddevelopmenttoapplications,J.EnergyStorage.27(2020)101035.

https://doi.org/10.1016/j.est.2019.101035.

[3] A. Ehsani, H. Parsimehr, H. Nourmohammadi, R. Safari, S. Doostikhah, Environment-friendly electrodes using biopolymer chitosan/poly ortho aminophenol with enhanced electrochemical behavior for use in energy storage devices, Polym. Compos. 40 (2019) 4629–4637. https://doi.org/10.1002/pc.25330.

[4] B. Wu, W. He, M. Lu, Z. Li, H. Qiang, Fabrication and electrochemical properties of flexible transparent supercapacitor electrode materials based on cellulose nanofibrils and reducedgrapheneoxide,Polym.Compos.41(2020)1135–1144. https://doi.org/10.1002/pc.25444.

[5] D.G. Lee, C.M. Yang, B.H. Kim, Enhanced electrochemical properties of boron functional groups on porous carbon nanofiber/MnO_2 materials, J. Electroanal. Chem. 788 (2017) 192–197. https://doi.org/10.1016/j.jelechem.2017.01.059.

[6] X. Zhu, Recent advances of transition metal oxides and chalcogenides in pseudo-capacitors and hybrid capacitors: A review of structures, synthetic strategies, and mechanism studies, J. Energy Storage. 49 (2022) 104148. https://doi.org/10.1016/j.est.2022.104148.

[7] G.H. An, H.J. Ahn, Surface modification of RuO_2 nanoparticles-carbon nanofiber composites for electrochemical capacitors, J. Electroanal. Chem. 744 (2015) 32–36. https://doi.org/10.1016/j.jelechem.2015.03.009.

[8] T. Kshetri, D.T. Tran, H.T. Le, D.C. Nguyen, H. Van Hoa, N.H. Kim, J.H. Lee, Recent advances in MXene-based nanocomposites for electrochemical energy storage applications, Prog. Mater. Sci. 117 (2021) 100733. https://doi.org/10.1016/j.pmatsci.2020.100733.

[9] A.S. Levitt, M. Alhabeb, C.B. Hatter, A. Sarycheva, G. Dion, Y. Gogotsi, Electrospun MXene/carbon nanofibers as supercapacitor electrodes, J. Mater. Chem. A. 7 (2019) 269–277. https://doi.org/10.1039/c8ta09810g.

[10] S. Anand, M.W. Ahmad, A.K. Ali Al Saidi, D.J. Yang, A. Choudhury, Polyaniline nanofiber decorated carbon nanofiber hybrid mat for flexible electrochemical supercapacitor,Mater.Chem.Phys.254(2020)123480. https://doi.org/10.1016/j.matchemphys.2020.123480.

[11] A.K. Thakur, M. Majumder, R.B. Choudhary, S.N. Pimpalkar, Supercapacitor based on electropolymerized polythiophene and multiwalled carbon nanotubes composites, IOP Conf. Ser. Mater. Sci. Eng. 149 (2016) 012166. https://doi.org/10.1088/1757-899X/149/1/012166.

[12] Q. Niu, Y. Guo, K. Gao, Z. Shao, Polypyrrole/cellulose nanofiber aerogel as a supercapacitor electrode material, RSC Adv. 6 (2016) 109143–109149. https://doi.org/10.1039/c6ra23216g.

[13] M. Cheng, Y.N. Meng, Z.X. Wei, Conducting Polymer Nanostructures and their Derivatives forFlexibleSupercapacitors,Isr.J.Chem.58(2018)1299–1314. https://doi.org/10.1002/ijch.201800077.

[14] X. Yan, Z. Tai, J. Chen, Q. Xue, Fabrication of carbon nanofiber-polyaniline composite flexible paper for supercapacitor, Nanoscale. 3 (2011) 212–216. https://doi.org/10.1039/c0nr00470g.

[15] J. Li, G.X. Xu, Research progress on applications of Polyaniline(PANI) for Electrochemical Energy Storage and Conversion, 2020. https://doi.org/10.3980/j.issn.1672-5123.2017.9.12.

[16] P. Bharadiya, R. Jain, V. Chaudhari, S. Mishra, Graphene oxide-wrapped polyaniline nanorods for supercapacitor applications, Polym. Compos. 40 (2019) E1716–E1724. https://doi.org/10.1002/pc.25129.

[17] M. Yanilmaz, M. Dirican, A.M. Asiri, X. Zhang, Flexible polyaniline-carbon nanofiber supercapacitor electrodes, J. Energy Storage. 24 (2019) 100766. https://doi.org/10.1016/j.est.2019.100766.

[18] J. Yang, Y. Yang, J. Lan, Y. Yu, X. Yang, Polyaniline-manganese dioxide-carbon nanofiber ternary composites with enhanced electrochemical performance for supercapacitors, J. Electroanal. Chem. 843 (2019) 22–30. https://doi.org/10.1016/j.jelechem.2019.04.073.

[19] R.R. Atram, V.M. Bhuse, R.G. Atram, C.M. Wu, P. Koinkar, S.B. Kondawar, Novel carbon nanofibers/thionickel ferrite/polyaniline (CNF/$NiFe_2S_4$/PANI) ternary nanocomposite for high performance supercapacitor, Mater. Chem. Phys. 262 (2021) 124253. https://doi.org/10.1016/j.matchemphys.2021.124253.

[20] C. Zhang, Y. Ma, X. Zhang, S. Abdolhosseinzadeh, H. Sheng, W. Lan, A. Pakdel, J. Heier, F. Nüesch, Two-Dimensional Transition Metal Carbides and Nitrides (MXenes): Synthesis, Properties, and Electrochemical Energy Storage Applications, Energy Environ. Mater. 3 (2020) 29–55. https://doi.org/10.1002/eem2.12058.

[21] A. Vahidmohammadi, J. Moncada, H. Chen, E. Kayali, J. Orangi, C.A. Carrero, M. Beidaghi, Thick and freestanding MXene/PANI pseudocapacitive electrodes with ultrahigh specific capacitance, J. Mater. Chem. A. 6 (2018) 22123–22133. https://doi.org/10.1039/c8ta05807e.

[22] S. Ghosh, W.D. Yong, E.M. Jin, S.R. Polaki, S.M. Jeong, H. Jun, Mesoporous carbon nanofiber engineered for improved supercapacitor performance, Korean J. Chem. Eng. 36 (2019) 312–320. https://doi.org/10.1007/s11814-018-0199-1.

[23] M.R.W.A.A.S.R.G. Sonkawade, PANINFs synthesized electrochemically as an electrode material for energy storage application, Polym. Bull. 76 (2019) 4703–4718. https://doi.org/10.1007/s00289-018-2634-1.

[24] G. Xu, D. Xu, J. Zhang, K. Wang, Z. Chen, J. Chen, Q. Xu, Controlled fabrication of PANI/CNF hybrid films: Molecular interaction induced various micromorphologies and electrochemical properties, J. Colloid Interface Sci. 411 (2013) 204–212. https://doi.org/10.1016/j.jcis.2013.08.024.

[25] P. Jiménez, P. Castell, R. Sainz, A. Ansón, M.T. Martínez, A.M. Benito, W.K. Maser, Carbon nanotube effect on polyaniline morphology in water dispersible composites, J. Phys. Chem. B. 114 (2010) 1579–1585. https://doi.org/10.1021/jp909093e.

[26] S.F. Shaikh, F.F.M. Shaikh, A. V Shaikh, M. Ubaidullah, A.M. Al-enizi, H.M. Pathan, Electrodeposited more-hydrophilic nano-nest polyaniline electrodes for supercapacitor application, J. Phys. Chem. Solids. 149 (2021) 109774. https://doi.org/10.1016/j.jpcs.2020.109774.

[27] P. Song, X. He, J. Tao, X. Shen, Z. Yan, Z. Ji, A. Yuan, H_2SO_4-assisted tandem carbonization synthesis of PANI @ carbon@ textile flexible electrode for high-performance wearable energy storage, Appl. Surf. Sci. 535 (2021) 147755. https://doi.org/10.1016/j.apsusc.2020.147755.

[28] K. Jin, W. Zhang, Y. Wang, X. Guo, Z. Chen, L. Li, Y. Zhang, Z. Wang, J. Chen, L. Sun, T. Zhang, In-situ hybridization of polyaniline nano fibers on functionalized reduced graphene oxide films for high-performance supercapacitor, Electrochim. Acta. 285 (2018) 221–229. https://doi.org/10.1016/j.electacta.2018.07.220.

[29] A.P.M. Udayan, O. Sadak, S. Gunasekaran, Metal-Organic Framework/Polyaniline Nanocomposites for Lightweight Energy Storage, ACS Appl. Energy Mater. 3 (2020) 12368–12377. https://doi.org/10.1021/acsaem.0c02376.

[30] S. Cao, T. Zhao, Y. Li, L. Yang, A. Ahmad, T. Jiang, Y. Shu, Z. Jing, H. Luo, X. Lu, H. Zhang, Fabrication of PANI @ Ti_3C_2Tx/PVA hydrogel composite as flexible supercapacitor electrode with good electrochemical performance, Ceram. Int. 48 (2022) 15721–15728. https://doi.org/10.1016/j.ceramint.2022.02.108.

[31] S. Liu, K. Wan, C. Zhang, T. Liu, Polyaniline-decorated 3D carbon porous network with excellent electrolyte wettability and high energy density for supercapacitors, Compos.

Commun. 24 (2021) 100610. https://doi.org/10.1016/j.coco.2020.100610.

[32] Y. Zhu, H. Xu, P. Chen, Y. Bao, X. Jiang, Electrochemical performance of polyaniline-coated γ -MnO_2 on carbon cloth as flexible electrode for supercapacitor, Electrochim. Acta. 413 (2022) 140146. https://doi.org/10.1016/j.electacta.2022.140146.

[33] W. Luo, Y. Wei, Z. Zhuang, Z. Lin, X. Li, C. Hou, T. Li, Y. Ma, Fabrication of Ti_3C_2Tx MXene/polyaniline composite films with adjustable thickness for high-performance flexible all-solid-state symmetric supercapacitors, Electrochim. Acta. 406 (2022) 139871. https://doi.org/10.1016/j.electacta.2022.139871.

[34] Y. Wei, W. Luo, X. Li, Z. Lin, C. Hou, M. Ma, J. Ding, T. Li, Y. Ma, PANI-MnO_2 and Ti $_3C_2T_x$ (MXene) as electrodes for high-performance flexible asymmetric supercapacitors, Electrochim. Acta. 406 (2022) 139874. https://doi.org/10.1016/j.electacta.2022.139874.

[35] A. Sikdar, P. Dutta, S. Kumar, A. Majumdar, N. Padma, S. Ghosh, U. Narayan, Spontaneous three-dimensional self-assembly of MXene and graphene for impressive energy and rate performance pseudocapacitors, Electrochim. Acta. 391 (2021) 138959. https://doi.org/10.1016/j.electacta.2021.138959.

[36] D.J. Ahirrao, A. Kumar, V. Singh, N. Jha, Nanostructured porous polyaniline (PANI) coated carbon cloth (CC) as electrodes for flexible supercapacitor device, J. Mater. Sci. Technol. 88 (2021) 168–182. https://doi.org/10.1016/j.jmst.2021.01.075.

[37] H. Huang, S.C. Abbas, D. Ph, Q. Deng, Y. Ni, S. Cao, X. Ma, An all-paper , scalable and flexible supercapacitor based on vertically aligned polyaniline (PANI) nano-dendrites@ fibers,J.PowerSources.498(2021)229886. https://doi.org/10.1016/j.jpowsour.2021.229886.

[38] M. Faraji, H.M. Aydisheh, Facile and scalable preparation of highly porous polyvinyl chloride-multi walled carbon nanotubes-polyaniline composite film for solid-state fl exible supercapacitor,Compos.PartB.168(2019)432–441. https://doi.org/10.1016/j.compositesb.2019.03.060.

[39] S.K. Simotwo, V. Kalra, Polyaniline-carbon based binder-free asymmetric supercapacitor in neutral aqueous electrolyte, Electrochim. Acta. 268 (2018) 131–138. https://doi.org/10.1016/j.electacta.2018.01.157.

[40] F. Miao, C. Shao, X. Li, K. Wang, N. Lu, Y. Liu, Electrospun Carbon Nanofibers/Carbon Nanotubes/Polyaniline Ternary Composites with Enhanced Electrochemical Performance for Flexible Solid-State Supercapacitors, ACS Sustain. Chem. Eng. 4 (2016) 1689–1696. https://doi.org/10.1021/acssuschemeng.5b01631.

[41] D. Liu, H. Wang, P. Du, W. Wei, Q. Wang, P. Liu, Flexible and robust reduced graphene oxide/carbon nanoparticles/polyaniline (RGO/CNs/PANI) composite films: Excellent candidates as free-standing electrodes for high-performance supercapacitors, Electrochim. Acta. 259 (2018) 161–169. https://doi.org/10.1016/j.electacta.2017.10.165.

Chapter-IV

Hierarchically structured carbon nanofibers with embedded MXene and coated with cobalt oxide as electrode

4.1. Literature review

Supercapacitors offer notable advantages like high-power density, quick charge/discharge capabilities, and excellent cyclic stability without significant degradation[1–3]. However, one main limitation of supercapacitors is the relatively limited energy density compared to other energy storage devices. To overcome this limitation, extensive studies are currently being conducted to develop supercapacitors with enhanced energy density[4–6]. Increasing energy density in supercapacitors can be attained by combining pseudocapacitive electrode materials with electrochemical double-layer capacitor (EDLC) electrode materials and engineering the physicochemical properties of the EDLC electrode materials. The EDLCs use mostly carbon materials, where energy is stored through the separation of charges at the electrode and the electrolyte interface, which makes surface area an important parameter to enhance the specific capacitance. Frequently, EDLCs utilize electrodes such as carbon nanofibers [7], carbon aerogels [8], carbon nanotubes [9], and activated carbons [10] as EDLC electrodes due to their high specific surface area (SSA) and controllable pore structure[7,8]. Carbon nanofibers (CNFs) are a relatively new type of carbon nanomaterial that offers several advantages over conventional powder or granular-form electrode materials. CNFs exhibit high conductivity, freestanding ability, high SSA, and excellent electrode-electrolyte interface. CNFs demonstrate specific capacitance in the range of 120 and 280 F g^{-1} in aqueous and non-aqueous electrolytes. To enhance the CNF's specific capacitance, the surface area of CNF was enhanced by either activation, creating porosity, or generating hollow fibers[9]. Despite the clear benefits of hollow fibers compared to other types of fibers such as significant surface area, improved mass transport, minimized volume expansion, and lightweight properties - research is constrained due to the intricate nature of the synthesis process[10,11].

Besides adjusting the porosity and surface area of CNF-based electrodes, they were frequently infused with transition metal oxides (TMOs) to increase the specific capacitance. TMOs exhibit pseudocapacitive charge-discharge behavior, which stores charge at the electrode surface via Faradaic redox processes. Although TMOs possess high theoretical capacitances due to their multiple valence states, they suffer from poor electrochemical stability due to low electrical conductivity. Often, TMOs were combined with conductive carbon materials and conductive polymer materials[12,13]. TMO electrode materials, such as RuO_2, Fe_2O_3, Mn_2O_3, and Co_3O_4, have been broadly examined as potential electrodes for supercapacitors. Among these, cobalt

oxide (Co_3O_4) has garnered considerable attention due to its reversible redox reactions, which result in an exceptional theoretical specific capacitance of 3560 F g^{-1}. Additionally, it also exhibits advantages such as low cost and good chemical stability. However, volume expansion during charging-discharging and poor electrical conductivity hinders Co_3O_4 from realizing its full potential in supercapacitor applications. To effectively tackle the problem, nano structuring of Co_3O_4 is a viable approach, which can help in accommodating the volume expansion during the charge-discharge [14,15]. Additionally, another method involves using carbon and Co_3O_4 composite electrodes [16]. Guetae et al. developed a flexible, hierarchically porous structure of carbon nanofibers (CNFs) containing embedded Co_3O_4. This architecture was fabricated through coaxial electrospinning and subsequent thermal treatment, demonstrating a specific capacitance of 188 F g^{-1} at 1 mA cm^{-2}[17]. In addition to metal oxides, MXenes are promising two-dimensional materials for energy storage and conversion applications[18,19]. MXene molecule is generally described by the general formula $M_{n+1}X_nT_x$, where X is N or C; M represents early transition metal (Mo, Ti, Nb); and Tx is a functional group such as -OH, -O, and -F. These are relatively new types of two-dimensional materials with excellent electrical conductivity, mechanical stability, and enhanced hydrophilicity. Often, MXenes are incorporated into carbon nanofibers or combined with binary material to make ternary composites, aiming to improve the specific capacitance[20]. This is due to their limited use in pristine form owing to the issue of self-restacking during the charge-discharge process[21]. In a few studies, MXene and metal oxide/conductive polymer were combined with carbon nanofibers to benefit from the synergetic effect of high capacitance and excellent electric conductivity. However, there are no available studies so far on hollow ternary composite nanofibers to the best of our knowledge.

In this study, we establish the synthesis of the novel Co_3O_4-coated hollow MXene-embedded carbon nanofibers (HMCNF) to harness the synergetic effects result from the combination of hollow fibers, metal oxide, and MXene. These fibers exhibited excellent electrode-electrolyte interface, mass transport, and conductivity, leading to excellent electrochemical performance.

4.2. Experimental

4.2.1. Materials and Reagents

Cobalt nitrate hexahydrate (Co $(NO_3)_2.6H_2O$) 98% pure, poly(acrylonitrile) (PAN) Molecular weight (Mw) of approximately 1,50,000, Poly (vinyl pyrrolidone) (PVP) Mw ~ 130 000 and Poly (methyl methacrylate) (PMMA) Mw ~350 000 and Lithium Fluoride (LiF) were

purchased from Sigma Aldrich Chemical Co., India; Potassium hydroxide (KOH) flakes and N, N-Dimethyl formamide (DMF) (95%) and Hydrochloric acid(HCl) (37 wt. %) were procured from Finar Chemicals Co; MAX (Ti_3AlC_2) phase was provided by Arizon Chemoze Pvt. Ltd.

4.2.2. Methods

4.2.2.1. Synthesis of Hollow MXene/CNF composite nanofibers

To begin, Multi-layered MXene (Ti_3C_2) was prepared by careful etching of Al from the MAX phase. In a Teflon reagent reactor, 1 g of LiF was safely added to 20 mL 9M HCl solution with proper safety precautions. Subsequently, 1 g of MAX phase was gradually introduced to the above solution and the solution was maintained at 35℃ for 24 hours in the fume hood. Afterward, the MXene colloidal solution underwent centrifugation for 6 minutes at 3500 rpm. This centrifugation step was repeated 6-7 times until the pH value reached a neutral level. Next, delaminated layers of MXene were obtained by subjecting the neutralized matter to ultra-sonication in DMF for 2 hours in a nitrogen atmosphere, followed by centrifugation for 1 hour at 3500 rpm. To prepare the polymer solution for the shell side, 0.8 g of PAN was dissolved into a delaminated MXene-containing DMF solution with magnetic stirring. Embedding MXenes into the PAN-derived carbon prevented 2D layer accumulation and self-restacking of MXenes, thereby improving the electrical conductivity of carbon nanofibers. For the core side, in another reagent bottle, 0.4 g of PVP and 0.6 g of PMMA were dissolved in pure DMF solvent and stirred for six hours. These two polymer solutions were transferred into two separate 10 ml syringes to perform co-axial electrospinning. The optimized parameters after several trials of experiments were maintained to obtain core-shell fibers, including an applied voltage of 18 kV, a needle tip-to-drum collector distance of 12 cm and 0.8 ml h^{-1} and 0.6 ml h^{-1} syringe flow rates for shell and core, respectively. Furthermore, in the process of obtaining the hollow nanofibers, the electrospun membrane was peeled from aluminum foil and was ultra-sonicated to remove PVP, which acted as a sacrificial polymer. Finally, the membrane was pre-oxidized(stabilization) at 240 ℃ for 2 h in air. During the stabilization process of the polymer mat, linear PAN molecules were dehydrogenated and cyclized, resulting in significant improvement in the flexibility of CNF. Subsequently carbonized at 900 ℃ for another 1 hour with nitrogen purging, with a heating rate of 4 ℃ min^{-1}, in the process of carbonization that occurs at 900 °C in an inert environment, causes chemical changes of de-polymerization, random scission, and side-group elimination. The core was derived from PVP and PMMA for

creating hollow structures, and mesopores were achieved by using PVP as a sacrificial polymeric phase. Moreover, the pyrolysis of PMMA can be used as a source of nitrogen for in situ nitrogen doping of hollow carbonaceous materials with the addition of functional groups enhancing HMCNF's wettability and also hierarchical pores and hollow structures. The core structure of PMMA can release volatile degradation products during thermal treatment, which can result in the formation of channels and porous structure, resulting in a hollow carbon composite nanofibrous membrane[22,23].

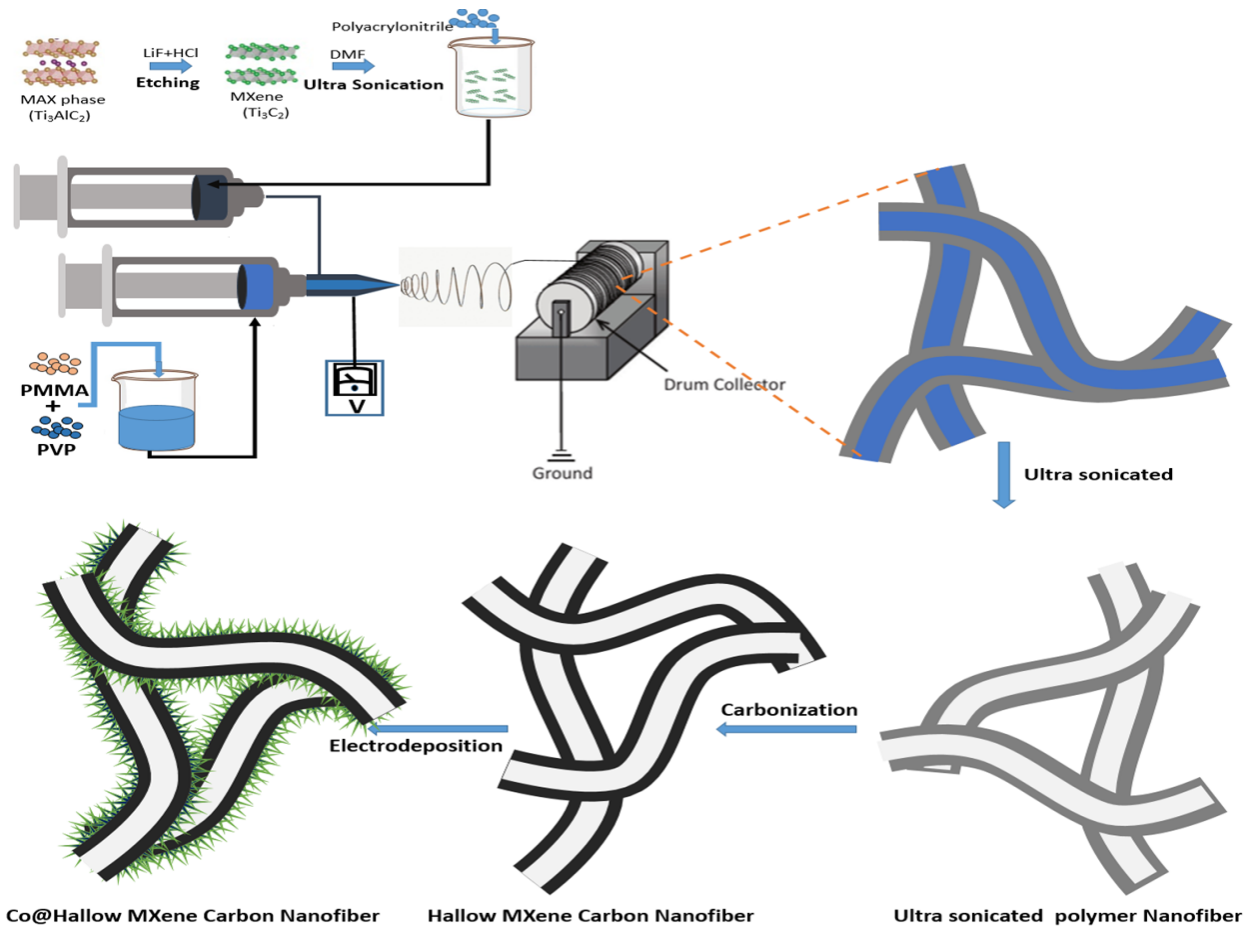

Figure.4.1: Schematic illustrating the synthesis process of the Co_3O_4/HMCNF composite.

4.2.2.2 Synthesis of Co_3O_4 coated HMCNF ternary composite and characterization

The electrodeposition process to create a cobalt oxide layer over the hollow nanofibers was performed using cyclic voltammetry, followed by thermal treatment. In a neutral medium, a three-electrode system was employed, comprising of binary/ternary composite nanofibrous membrane as a working electrode, a saturated calomel electrode (SCE) as the reference

electrode, and a platinum plate as a counter electrode. Cobalt nitrate hexahydrate (10 mM) dissolved in double distilled water was used as the electrolyte for the electrodeposition of cobalt hydroxide. Using the cyclic voltammetry technique at a voltage scan rate of 10 mV s^{-1}, the potential was swept from 0 to -1.2V, and the cyclic process was repeated ten times. As a result of the deposition process, cobalt hydroxide $Co(OH)_2$ was produced on the substrate surface, which was calcined for 60 minutes at 350℃[24]. This thermal treatment resulted in the formation of a cobalt tetroxide (Co_3O_4) film, and this sample was labeled as Co_3O_4/HMCNF. Further, anodic electrodeposition of cobalt species produces cobalt oxyhydroxide thin films, most likely through electrochemical processes onto HMCNF. The present case involved forming films on HMCNF substrates by cyclic voltammetry between 0 and -1.2 V/ SCE at a voltage scan rate of 10 mV s^{-1}. The transition of Co^{2+} to Co^{3+} occurs at about -0.45 V/SCE in the negative potential scan. The electrochemical process responsible for cobalt oxyhydroxide deposition can be understood through the reduction peak occurring at -0.35 V/SCE. This reduction corresponds to the transformation of different cobalt oxide species following a series of extensive sweeps. In addition, the crystallinity of the nanoparticles was enhanced by annealing them for 60 minutes at 350 ℃[25–27]. A schematic representation of the fabrication process for hollow hierarchical porous and bridging Co_3O_4/HMCNFs is shown in Fig.4.1.

Field emission electron microscopy (FESEM, Carl Zeiss, Zeiss Gemini 300) coupled with energy dispersive X-ray spectroscopy (EDS) was employed to examine the surface characteristics of the binary and ternary electrodes. To assess the structural properties of the electrodes, X-ray diffraction (XRD, PANalytical, XPert Powder) and Raman spectroscopy (Thermo Scientific DXR) were employed. Additionally, the elemental composition and chemical state were examined using X-ray photoelectron spectroscopy (XPS, ESCALAB Thermo-Scientific 250Xi), while the pore size distribution and surface area were assessed using Brunauer-Emmett-Teller (BET, Quanta chrome Autosorb) physisorption analyzer. An electrochemical workstation (CHI6002E, CH Instruments) was used to accomplish electrochemical techniques such as cyclic voltammetry (CV), galvanostatic charge-discharge experiments (GCD), and electrochemical impedance spectroscopy (EIS). 6 M KOH was used as an electrolyte, composites were cut into 1 × 1 cm^2 and used as free-standing, binder-free working electrodes. The performance of individual electrodes was researched by a three-electrode system, where the obtained composite, Hg/HgO and Pt wire were used as the working electrode, reference electrode and counter electrode, respectively. In order to test using a two electrodes system, Swagelok symmetric cells were fabricated using free-standing Co_3O_4

/HMCNF composite cut into 15 mm diameter round films as electrodes, 6M KOH as electrolyte solution, and glass microfiber filter as a separator.

4.3. Results and discussion

4.3.1 Morphology and structural characterization

4.3.1.1 FESEM analysis of Ternary and Binary composites

FESEM was employed to investigate the surface morphologies of composites involving HMCNF and Co_3O_4/HMCNFs. The FESEM images revealed a consistent and even surface on the core-shell nanofibers, as depicted in Fig.4.2(a), with no discernible bead formations. Fig.4.2(b) shows the higher magnification image of hollow fibers. These HMCNFs with the randomly interconnected network have an average fiber diameter of 261±10 nm. Moreover, the hollow architecture remained intact thanks to the uniform thickness of its shell and the rigid structure of MXenes. This structure also led to the formation of partial solid bridges within the matrix of the HMCNF shell.

FESEM images of Co_3O_4/HMCNFs shown in Fig.4.2(c) visually portray the well-arranged vertical orientation and uniform dispersion of Co_3O_4 nanopillars across the HMCNFs surface. Additionally, as shown in the magnified Fig.4.2(d) image, the presence of Co_3O_4 nanopillars on the HMCNFs surface results in a broadened nanofiber diameter. This increase in surface area contributes to an escalation in active site count. Fig.4.2(e) and 4.2(f) present the EDS analysis outcomes for the HMCNF and Co_3O_4/HMCNF samples. The analysis confirms the existence of Co on the surface of the Co_3O_4/HMCNF sample, in conjunction with N, O, Ti, and C elements, which are observable on both surfaces. The atomic weight percentage of individual elements within the samples was also provided in Fig.4.2(e) and Fig.4.2(f) as inset.

It was observed that the Co3O4 nanoparticles were homogeneous and aggregated. Figure 4a shows the TEM image of the Co3O4 nanoparticles on Hollow carbon nanofiber. Nanoparticles were estimated to have a size of 52 nm by TEM. Co3O4 nanoparticles consist of four diffraction rings with different radii and one center, as shown in Figure 4b the selected area diffraction pattern (SAED). These diffraction rings corresponded to the planes of Co3O4 (220), (311), (400), (511), and (440). Despite the particles' small size, dispersion of the particles was not uniform. Hence, it led to a widening of diffraction rings composed of many diffraction spots, indicating polycrystalline architectures. It was confirmed that Co_3O_4 nanoparticles had a cubic structure by the SAED pattern, and this was in good agreement with the XRD results.

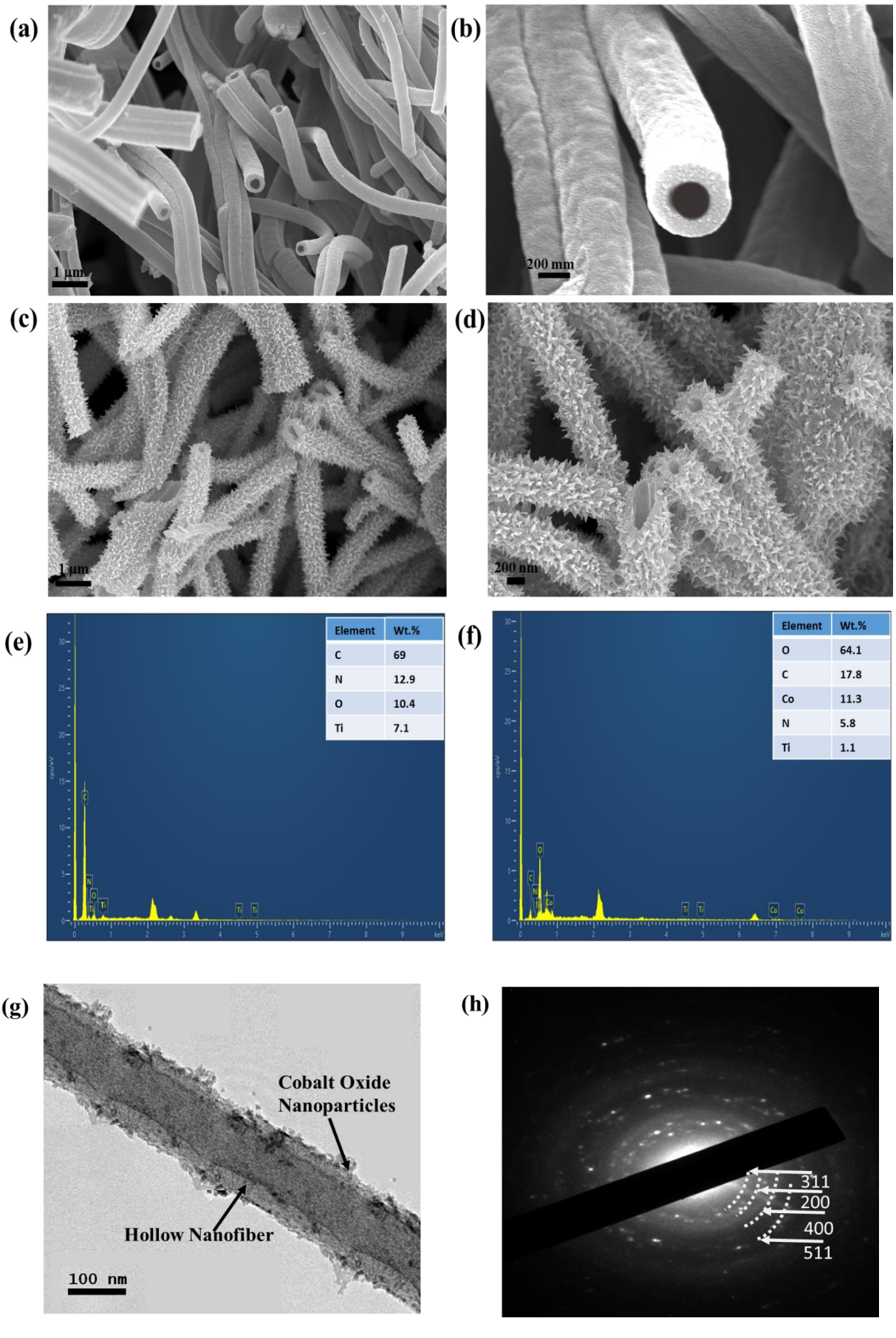
(a)
1 µm
(b)
200 mm
(c)
1 µm
(d)
200 nm
(e)
Element | Wt.%
C | 69
N | 12.9
O | 10.4
Ti | 7.1
(f)
Element | Wt.%
O | 64.1
C | 17.8
Co | 11.3
N | 5.8
Ti | 1.1
(g)
Cobalt Oxide Nanoparticles
Hollow Nanofiber
100 nm
(h)
311
200
400
511

Figure 4.2: Typical FESEM images of (a, b) HMCNF (c, d) the FESEM images of Co_3O_4/HMCNF composite superstructures, (e, f) EDS spectrum obtained from HMCNF and Co_3O_4/HMCNF composite. (g, h) TEM image of Co-MOF /MXene/CNF composite.

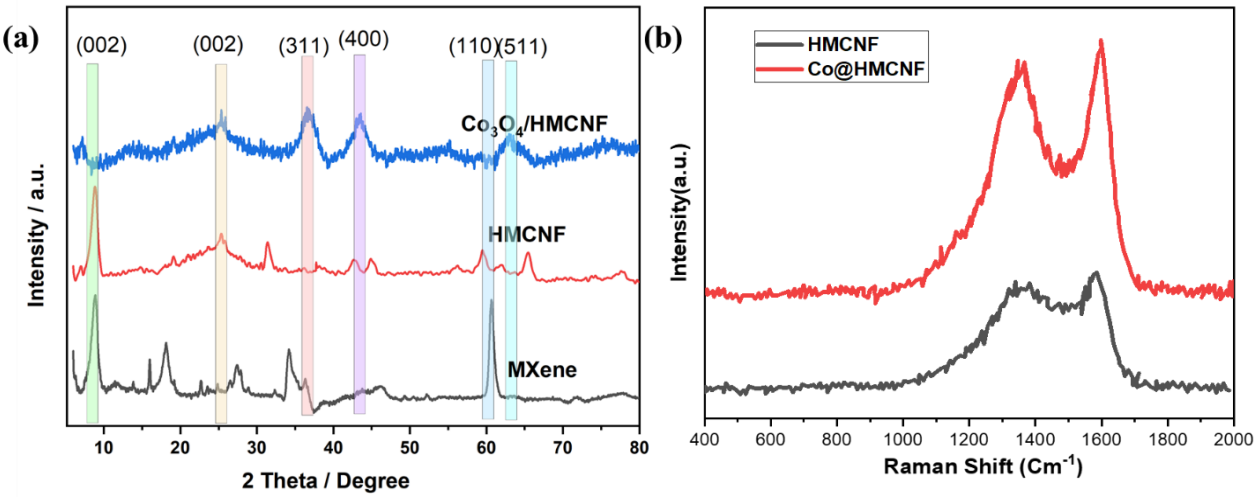

Figure 4.3: (a) comparison of X-Ray diffraction patterns, (b) Raman spectra of HMCNF and Co_3O_4/HMCNF composites.

4.3.1.2 XRD analysis of Ternary and Binary composites

The XRD patterns of pure MXene, Co_3O_4/HMCNF, and HMCNF composites were recorded and shown in Fig.4.3 (a). The comparison of diffraction patterns of the Co_3O_4/HMCNFs and HMCNFs composites revealed one standard broad peak at 2θ values around 25.6°, which can be indexed to the (0 0 2) plane of amorphous nature of the carbon nanofibers[28]. The Co_3O_4/HMCNFs composite exhibited diffraction peaks at 2θ values of 36.6, 44.5, and 59.9° , corresponding to (311), (400) and (511) planes of the cobalt oxide, respectively[29,30]. Furthermore, a diffraction peak positioned at approximately 2θ values of 6.4° can be associated with the (0 0 2) peaks of MXene. This peak's intensity diminishes and eventually vanishes in the Co_3O_4/HMCNF sample, a result of the deposition of Co_3O_4.[31]. While Co_3O_4 can crystallize in various structures, its crystallinity can be significantly affected by factors like synthesis conditions, impurities, and particle size. Poorly crystallized Co_3O_4, particularly in the form of nanoparticles, often exhibits reduced peak intensity and broadening in the X-ray diffraction pattern, making it appear closer to amorphous.

4.3.1.3 Raman spectroscopy analysis of Ternary and Binary composites

Molecular vibration Raman spectroscopy was also employed to delve into the structural properties of the composite materials. Fig.4.3(b) displays the presence of the characteristic D

and G bands, depicted by peaks at 1337 and 1581 cm^{-1}, respectively. The G band signifies an in-plane tangential stretch vibration contributing to the organized graphitic layer, while the presence of the D band is attributed to defects and disordered structures. For HMCNFs and Co_3O_4/HMCNFs, the I_D/I_G ratios were nearly 0.9 and 0.95 respectively [32].

4.3.1.4 XPS analysis of Ternary and Binary composites

XPS was employed to investigate the surface composition and electronic structure. As shown in Fig.4.4(a), the survey spectrum displays four well-defined peaks representing C 1s, Co 2p, O 1s, and N 1s. The presence of the N element in HMCNFs can be attributed to the in-situ doping of nitrogen. This hierarchically porous N-doped carbon improves wettability and capacitive storage, enhancing performance. Fig.4.4(b) is a high-resolution XPS spectrum of Co 2p, in which the peak values of 775.10 eV and 793.21 eV correspond to Co^{3+}. Additional peaks were observed at 777.15 eV and 795.33 eV, attributed to Co^{2+}. Apart from the Co $2p_{3/2}$ peak, another distinct vibration satellite ("sat") is evident. Deconvolution of the C 1s peak yielded three separate peaks at 284.91, 286.54, and 289.10 eV (Fig.4.4(c)), corresponding to C=C, C-O, and C=O functionalities, respectively. The deconvoluted O 1s spectra shown in Fig.4.4(d) shows three oxygen contributions: O1 (529.1 eV) is attributed to metal–oxygen, O_2 (530.50 eV) is attributed to C=O and O_3 (530.04 eV) is attributed to C-O-H[33–35].

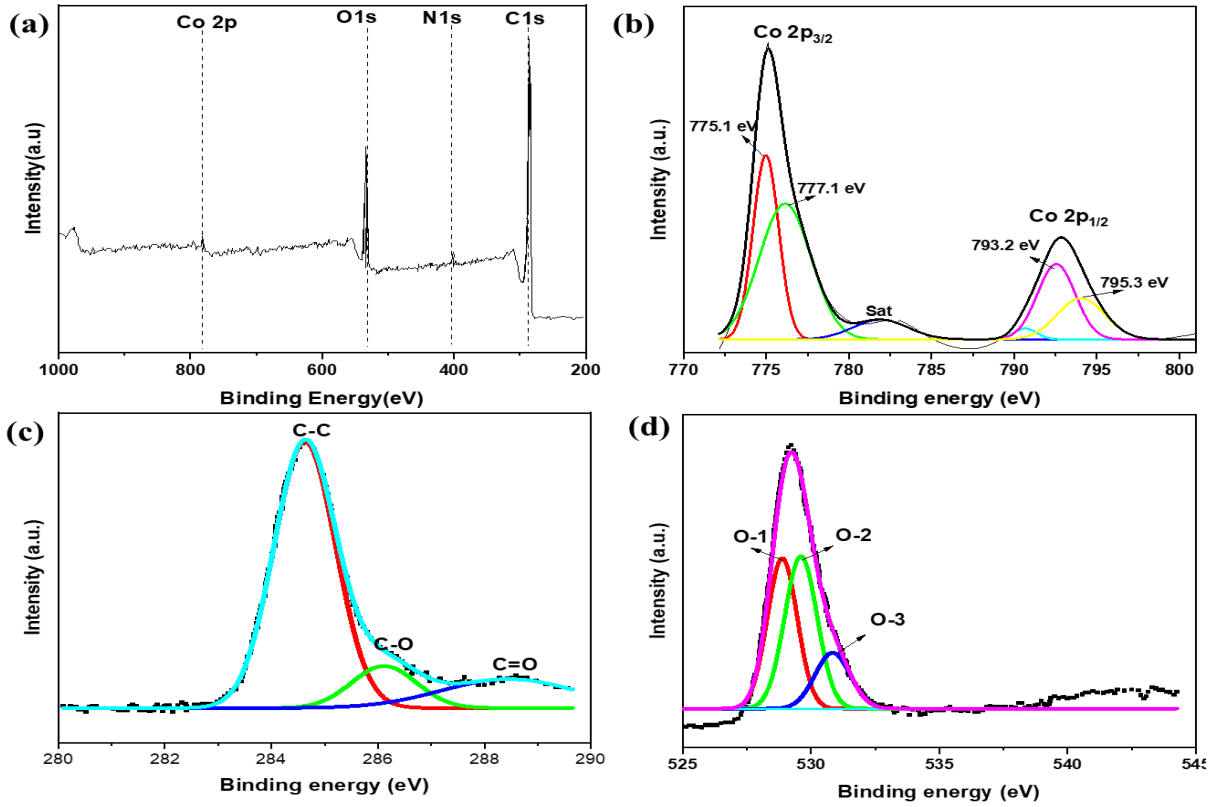

Figure 4.4: (a) XPS full spectra ;(b) Co 2p spectra: (c) C 1s spectra: and (d) O 1s spectra

4.3.1.5 BET analysis of Ternary and Binary composites

To analyze the pore size distribution and SSA of the prepared composites, we conducted N_2 adsorption/desorption isotherm measurements. Co_3O_4/HMCNFs isotherm displayed a hysteresis curve at a higher relative pressure, suggesting a substantially improved surface area of 174 m^2 g^{-1}. Similar findings were obtained from the pore size distribution data derived using the BJH method, as illustrated in Fig.4.5(b). The HMCNFs exhibited a broad distribution of mesopores ranging from 20 nm to 60 nm. This pore size distribution and high surface area (149 m^2 g^{-1}) of HMCNFs can be credited to the formation of pores and channels resulting from the evaporation of PMMA and PVP during pyrolysis[36]. In contrast, Co_3O_4/HMCNF displayed fewer mesopores, primarily around 25 nm. However, the hierarchical metal oxide deposition yielded enhanced specific surface area, which established pathways for electrolyte ion diffusion. A plausible explanation for enhanced SSA of Co_3O_4/HMCNF would be as follows: by aggregating nanoparticles, the entire surface of HMCNF became almost covered by Co_3O_4, causing the specific surface area to be increased. Moreover, these nanofiber pores and channels provide space for accommodating volume fluctuations in Co_3O_4 during charge and discharge cycles. Additionally, they function as conduits for ion storage and transmission[37,38]. Typical Carbon nanofiber resulting in a specific surface area in the range of 10–40 m2 g-1 (if the CNF does not possess internal porosity).Whereas Co3O4/HMCNF and HMCNF SSA are 149 and 174 m2 g-1 respectively.

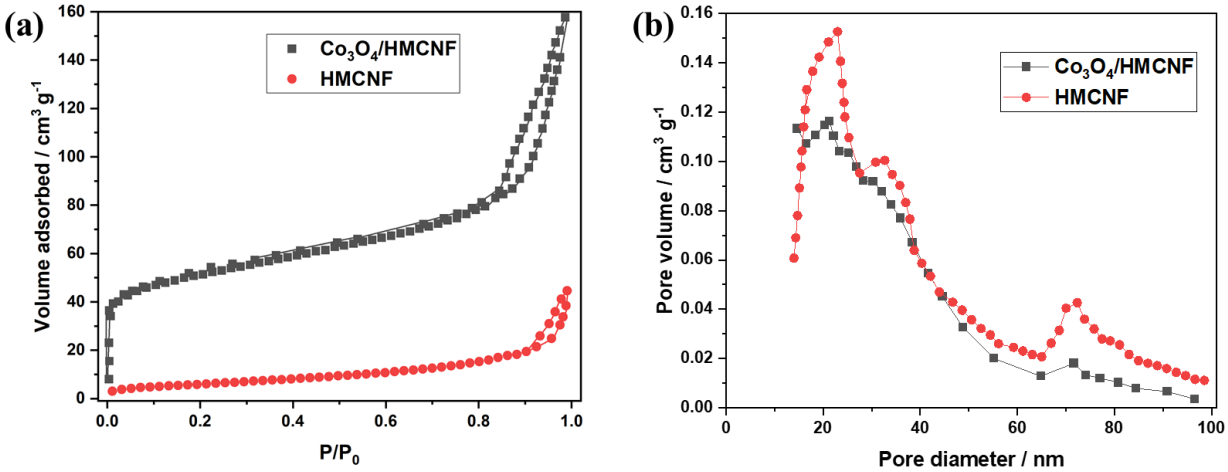

Figure 4.5: (a) BET hysteresis of as-prepared composites b) Pore size distribution curves

4.3.2 Electrochemical Characterization

4.3.2.1 Cyclic voltammetry analysis of Ternary and binary composite

Electrochemical performance of the Co_3O_4/HMCNFs and HMCNFs composite as supercapacitor electrode was assessed employing a three-electrode setup with an aqueous 6 M

KOH electrolyte. The CV curves of HMCNFs exhibit almost rectangular CV curves, whereas the curves of Co_3O_4 /HMCNF exhibit redox peaks attributable to active electrochemical functional groups. In the comparative CV curves shown in Fig.4.6(a), the non-rectangular nature of CV curves of Co_3O_4/HMCNF indicates the pseudocapacitive characteristics of electrodes, resulting in larger enclosed areas indicative of higher specific capacitance. Within the voltage range spanning from 0 to 0.6 V, a pair of reversible reduction and oxidation peaks becomes evident. The anodic peak materializes as Co_3O_4 is transformed into CoO_2 through oxidation, while the cathodic peak arises when the reverse process occurs for Co_3O_4[30].

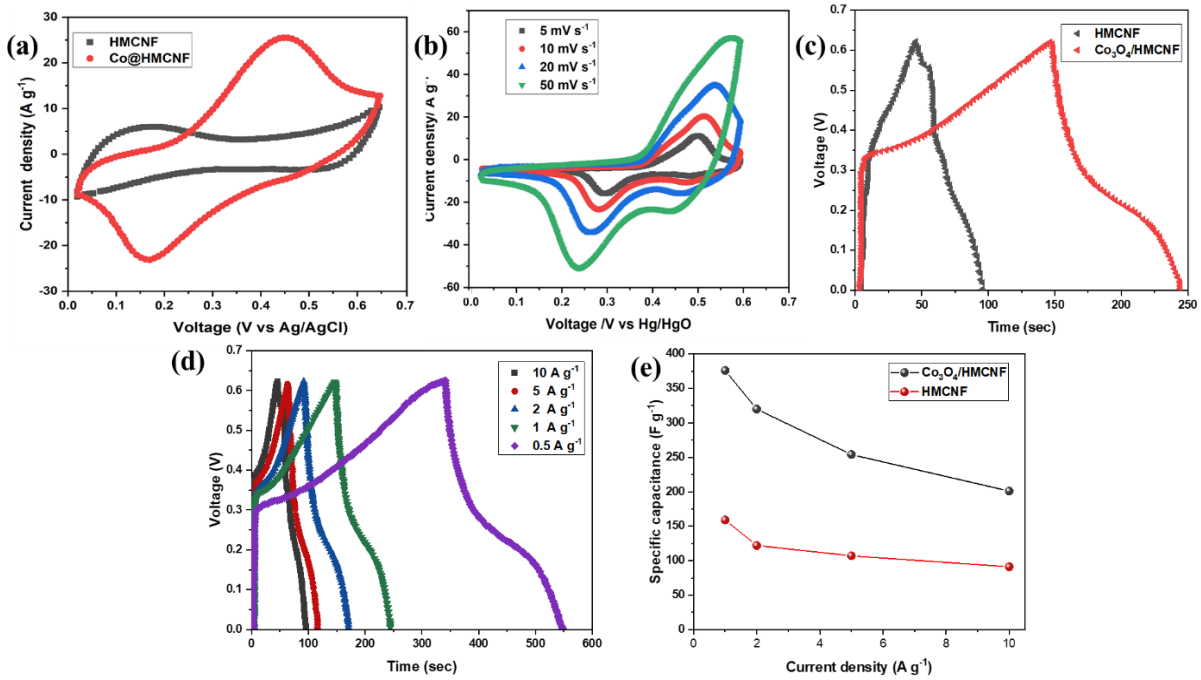

Figure 4.6: HMCNF and Co_3O_4/HMCNF composites (a) CV curve comparison (b) CV at different current densities (c) GCD comparison (d) GCD at different current densities and (e) Specific capacitance comparison

The CV curves of Co_3O_4/HMCNFs at different scan rates can be seen in Fig.4.6(b), displaying a quasi-rectangular shape pertaining to the hollow structure and hierarchical porous structure of the HMCNFs. The presence of Co_3O_4 nanopillars on the HMCNFs' surface facilitated the efficient transport of electrolyte ions. An increase in scan rate induced a minor right-side positive shift in oxidation peak and left-side negative shift in reduction peak potentials, which has mostly been endorsed to increasing electrochemical polarization[39,40]. For both Co_3O_4/HMCNFs and HMCNFs composites, GCD comparison curves were recorded at 0.5 A g^{-1}, as shown in Fig.4.6(c). The GCD curves align with CV findings, where a symmetrical triangle charge discharge profile indicates that HMCNFs exhibit EDLC like behaviour. Furthermore, as shown in Fig.4.6(d), the comparison of GCD curves of the Co_3O_4/HMCNFs

at varying current densities are non-symmetrical due to the presence of the pseudocapacitive material (Co_3O_4), consistent with the CV findings. The specific capacitance obtained from the GCD curves was 176.6 F g^{-1} for HMCNF and 384.1 F g^{-1} for Co_3O_4/HMCNF, indicating a synergistic interaction between Co_3O_4 nanopillars and HMCNF nanostructure. A comparison of the specific capacitance of two electrodes HMCNF and Co_3O_4/HMCNF, at different current densities are graphically presented in Fig.4.6(e).

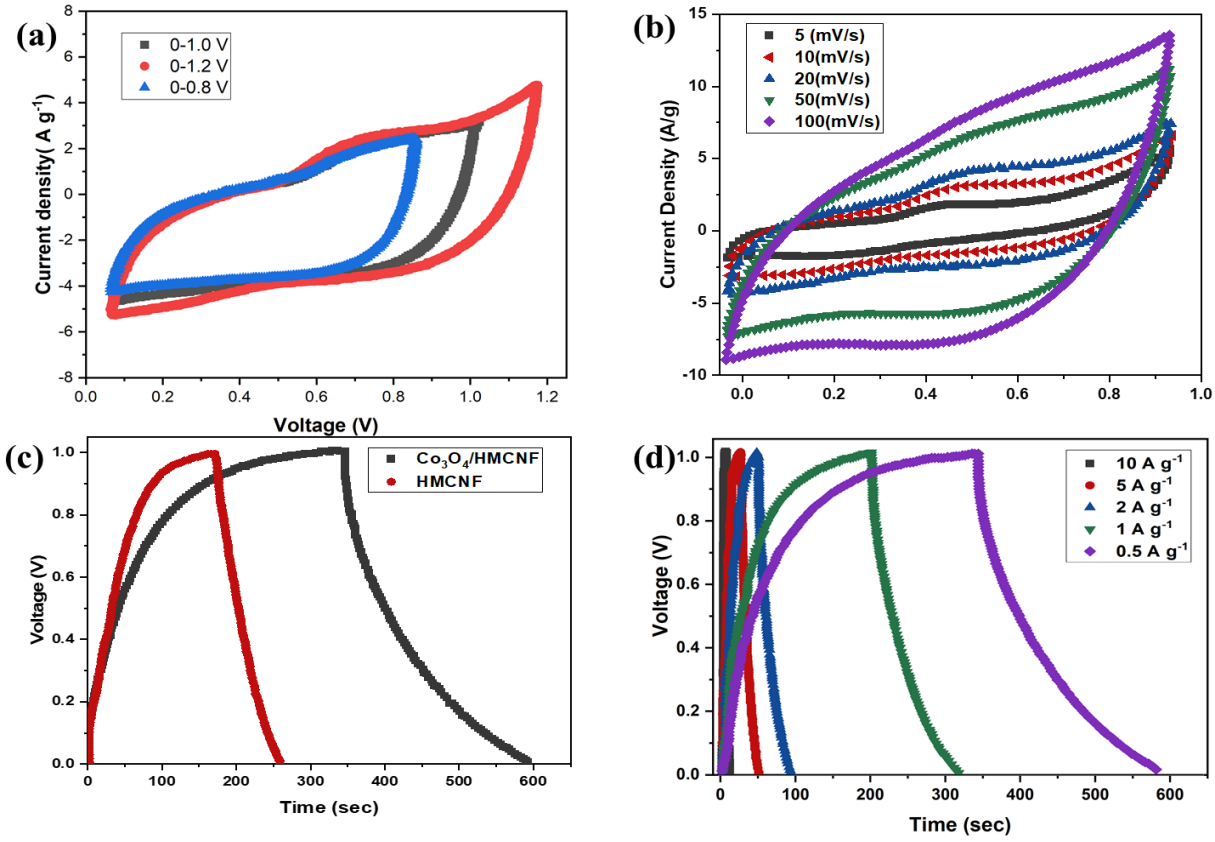

Figure 4.7: (a) CV curve at different series of voltage ranges for Co_3O_4/HMCNF (b) CV curves comparison for Co_3O_4/HMCNF at different scan rates (c) GCD curves comparison for HMCNF and Co_3O_4/HMCNF electrodes (d) GCD curves comparison for Co_3O_4/HMCNF at different current densities

Co_3O_4/HMCNF electrode material in three-electrode systems showed very good electrochemical performance and stability, making it an ideal electrode material for practical application. To assess the practicality of utilizing Co_3O_4/HMCNFs electrodes, a symmetric Co_3O_4/HMCNF electrode-based supercapacitor is constructed. A sequence of CV profiles was recorded for a symmetrically fabricated supercapacitor, spanning from 0 to 0.8 and up to 1.2 V at a voltage scan rate of 5 mV s^{-1} as demonstrated in Fig.4.7(a). Based on CV profile analysis, the 0 to1.2 V potential window showed a little electrochemical polarization, thereby suggesting 0 to1 V as an appropriate voltage window. There is no abrupt change in Current at potential 1

V, after 1.2 V only water molecules disassociate into Hydrogen and oxygen gases evolutions from the literature it is suggested that we can apply 1 V voltage for a symmetrical supercapacitor in an aqueous electrolyte. The quasi-rectangular CV curves in Fig.4.7(b) at different voltage scan rates for Co_3O_4/HMCNFs composite electrode indicated the combined effect of pseudocapacitive and electric double-layer charge storage. The redox peaks in CV curves remained unaffected with increased voltage scan rates.

4.3.2.2 GCD analysis of Ternary and binary composite

GCD curves comparison for HMCNF and Co_3O_4/HMCNF composite were recorded as shown in Fig.4.7(c). The symmetrical triangular curve seen in HMCNFs signifies the optimal electric double-layer capacitor (EDLC) traits, whereas the Co_3O_4/HMCNF composite's non-symmetrical behavior stems from pseudocapacitive influences. Additionally, all GCD curves show a non-symmetrical triangular shape at different current densities, as demonstrated in Fig.4.7(d). From the aforementioned GCD curves, we calculated the specific capacitance for Co_3O_4/HMCNFs, demonstrating a notable 374.4 F g^{-1} at 0.5 A g^{-1}. Furthermore, it succeeded in retaining 63.9% of its capacitance, even as the current density increased to 5 A g^{-1}, as illustrated in Fig.4.8(a). This enhanced performance can clearly be accredited to the hierarchical porous and hollow structure of the Co_3O_4/HMCNFs composite. The composite electrode's impressive specific capacitance and rate capability are ascribed to three key factors: (i) hollow structure and the hierarchical pores of HMCNF, (ii) large active electrochemical surface of Co_3O_4, which provides a supplementary contact interface between the electrolyte ions and the electrode materials and (iii) superb electrical conductivity of the MXene nanosheets[41–43]. The synergistic interplay of these factors contributed to the outstanding electrochemical performance. GCD experiments were also conducted to assess the cyclic stability of HMCNF and Co_3O_4/HMCNF composite electrodes for supercapacitors at 1 A g^{-1} for 5,000 cycles. Notably, the Co_3O_4/HMCNF and HMCNF electrodes showed commendable capacitance retention, retaining 88.5 % and 91% of its initial specific capacitance, respectively. This highlights their exceptional cycling stability, as depicted in Fig.4.8(c). Additionally, Co_3O_4/HMCNFs exhibited an outstanding energy density of 52 Wh kg^{-1} at a power density of 1000 W kg^{-1}. The energy densities at different power densities calculated based on GCD curves are displayed in Fig.4.8(d). This exceptional performance of Co_3O_4/HMCNF can be attributed to enhanced wettability and electrode-electrolyte interface. There is no IR drop in GCD curves for two electrode system and in three electrode system, GCD curves showed a nonsymmetrical triangular curve because of the pseudocapacitive behavior of materials. Furthermore, Co_3O_4 provided additional electron transport channels and increased active sites, while the stable

bridge structure between hollow HMCNF and MXene increased the strength and electrical conductivity. The specific conductivity of 6 M KOH aqueous solution (0.6266 S cm^{-1}) at room temperature is higher than that of 1 M KOH (0.2153 S cm^{-1}) and more suitable for enhancing the electrochemical properties. So, 6M KOH is commonly used as electrolyte for three and two electrode system.

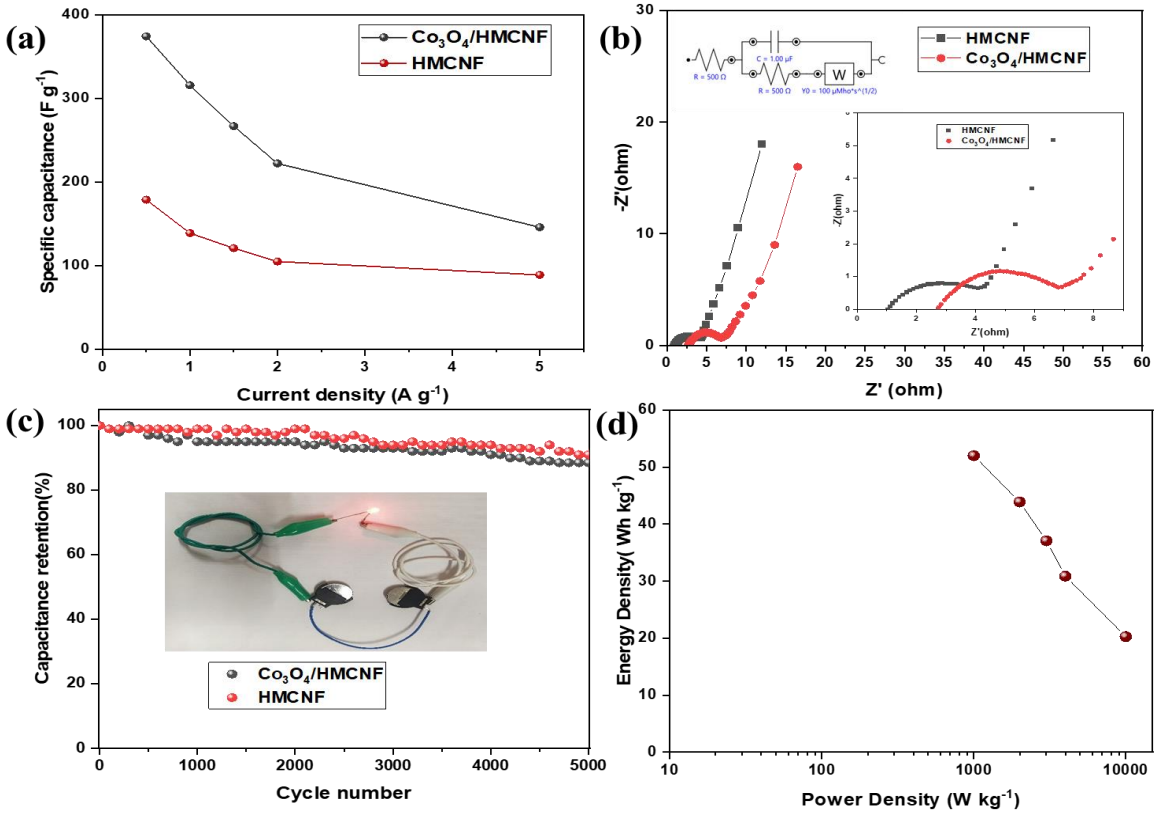

Fig.4.8: (a) Specific capacitance values of Co_3O_4/HMCNF and HMCNF composites at different current densities (b) Nyquist plot for Co_3O_4/HMCNF and HMCNF composites (c) capacitance retention (%) curves comparison for HMCNF and Co_3O_4/HMCNF electrodes (d) Ragone plot comparison for Co_3O_4/HMCNF.

4.3.2.3 EIS analysis of Ternary and binary composite

EIS technique is a very sensitive nondestructive characterization technique used to examine the electrical response of chemical systems. Nyquist plots were recorded for Co_3O_4/HMCNFs and HMCNF, illustrating the transport of ions and charges within electrodes. The Nyquist profiles shown in Fig.4.8(b) were allied with Warburg diffusion (ion diffusion) in the low frequency region. The presence of Co_3O_4 nanoparticles on the HMCNFs surface led to a reduction in electrical conductivity for Co_3O_4/HMCNFs in the high-frequency plot. Furthermore, the equivalent circuit fitting yielded a charge transfer resistance (R_{ct}) value of 2.6 for Co_3O_4/HMCNF and 1.4 for HMCNFs. This points towards an increase in resistance and a

decrease in electronic conductivity. This also indicates resistance to ion transfer between the electrolyte phases and the electrode surface as represented by charge transfer resistance (R_{ct}) or semicircle diameter. The inclusion of MXenes in HMCNFs improved the electron transit kinetics, attributed to the smaller semicircle (Rct) when HMCNFs were bridged with MXenes. The equivalent circuit creates Warburg diffusion ($W_{o)}$ by regulating ion transport and diffusion in the electrolyte at a low frequency. The dispersed resistance and capacitance at the HMCNF/electrolyte interface result in the transition of the Warburg zone at high frequency. In comparison to HMCNF, the steepest slope was observed for Co_3O_4/HMCNFs, indicating superior ion diffusion properties.

4.4 Conclusions

Hollow carbon nanofibers embedded with MXene were prepared using coaxial electrospinning, followed by pyrolysis. These fibers were further covered with hierarchical Co_3O_4 using an electrodeposition technique. Through an exhaustive analysis, this study meticulously compared the electrochemical performance of both types of electrodes while correlating their outcomes with the underlying physicochemical properties of binary and ternary electrode configurations, showcased a remarkable specific capacitance of 374.4 F g^{-1} at 0.5 A g^{-1}, accompanied by an impressive cycle stability with 88.5% capacity retention after undergoing 5,000 cycles. Furthermore, the symmetrical cell built upon this ternary electrode demonstrated exceptional energy storage capabilities, yielding a high energy density of 52.5 Wh kg^{-1} at a power density of 1000 W kg^{-1}, along with a noteworthy rate capability of 63.9% at 5 A g^{-1}. This study unveils the substantial potential encompassed within the synergistic structure of MXene-linked hierarchical porous and hollow carbon nanofibers adorned with Co_3O_4 nanoparticles. These findings extend its promise across a diverse spectrum of applications.

4.5 References

[1] C. Zhong, Y. Deng, W. Hu, J. Qiao, L. Zhang, J. Zhang, A review of electrolyte materials and compositions for electrochemical supercapacitors, Chem. Soc. Rev. 44 (2015) 7484–7539. https://doi.org/10.1039/c5cs00303b.

[2] F. Béguin, V. Presser, A. Balducci, E. Frackowiak, Carbons and electrolytes for advancedsupercapacitors,Adv.Mater.26(2014)2219–2251. https://doi.org/10.1002/adma.201304137.

[3] B. Ramasubramanian, S. Sundarrajan, V. Chellappan, M. V. Reddy, S. Ramakrishna, K. Zaghib, Recent Development in Carbon-$LiFePO_4$ Cathodes for Lithium-Ion Batteries: A Mini Review †, Batteries. 8 (2022) 1–25. https://doi.org/10.3390/batteries8100133.

[4] M.M. Baig, M.A. Khan, I.H. Gul, S.U. Rehman, M. Shahid, S. Javaid, S.M. Baig, A Review of Advanced Electrode Materials for Supercapacitors: Challenges and Opportunities, J. Electron. Mater. (2023). https://doi.org/10.1007/s11664-023-10532-5.

[5] X. Du, X. Ren, C. Xu, H. Chen, Recent advances on the manganese cobalt oxides as electrode materials for supercapacitor applications: A comprehensive review, J. Energy Storage. 68 (2023) 107672. https://doi.org/10.1016/j.est.2023.107672.

[6] D. Darbar, M. V. Reddy, S. Sundarrajan, R. Pattabiraman, S. Ramakrishna, B.V.R. Chowdari, Anodic electrochemical performances of $MgCo_2O_4$ synthesized by oxalate decomposition method and electrospinning technique for Li-ion battery application, Mater.Res.Bull.73 (2016) 369–376. https://doi.org/10.1016/j.materresbull.2015.09.025.

[7] S. Unknown, P. Chand, A. Joshi, Biomass derived carbon for supercapacitor applications:Review,J.EnergyStorage.39(2021)102646. https://doi.org/10.1016/j.est.2021.102646.

[8] R. Dubey, V. Guruviah, Review of carbon-based electrode materials for supercapacitor energy storage, Ionics (Kiel). 25 (2019) 1419–1445. https://doi.org/10.1007/s11581-019-02874-0.

[9] Q. Xu, X. Yu, Q. Liang, Y. Bai, Z.H. Huang, F. Kang, Nitrogen-doped hollow activated carbon nanofibers as high performance supercapacitor electrodes, J. Electroanal. Chem. 739 (2015) 84–88. https://doi.org/10.1016/j.jelechem.2014.12.027.

[10] P. Zhao, M. Yao, H. Ren, N. Wang, S. Komarneni, Nanocomposites of hierarchical ultrathin MnO_2 nanosheets/hollow carbon nanofibers for high-performance asymmetric supercapacitors,Appl.Surf.Sci.463(2019)931–938. https://doi.org/10.1016/j.apsusc.2018.09.041.

[11] V.S. Budhiraju, R. Kumar, A. Sharma, S. Sivakumar, Structurally stable hollow mesoporous graphitized carbon nanofibers embedded with $NiMoO_4$ nanoparticles for high performance asymmetric supercapacitors, Electrochim. Acta. 238 (2017) 337–348. https://doi.org/10.1016/j.electacta.2017.04.039.

[12] M. Naveed ur Rehman, T. Munawar, M.S. Nadeem, F. Mukhtar, A. Maqbool, M. Riaz, S. Manzoor, M.N. Ashiq, F. Iqbal, Facile synthesis and characterization of conducting polymer-metal oxide based core-shell PANI-Pr_2O–NiO–Co_3O_4 nanocomposite: As electrode material for supercapacitor, Ceram. Int. 47 (2021) 18497–18509. https://doi.org/10.1016/j.ceramint.2021.03.173.

[13] Y. Li, Z. Zhang, Y. Chen, H. Chen, Y. Fan, Y. Li, D. Cui, C. Xue, Facile synthesis of a Ni-based $NiCo_2O_4$-PANI composite for ultrahigh specific capacitance, Appl. Surf. Sci.

506 (2020) 144646. https://doi.org/10.1016/j.apsusc.2019.144646.

[14] L. Yang, Q. Zhu, K. Yang, X. Xu, J. Huang, H. Chen, H. Wang, A Review on the Application of Cobalt-Based Nanomaterials in Supercapacitors, Nanomaterials. 12 (2022). https://doi.org/10.3390/nano12224065.

[15] R. Ramaseshan, S. Sundarrajan, R. Jose, S. Ramakrishna, Nanostructured ceramics by electrospinning, J. Appl. Phys. 102 (2007). https://doi.org/10.1063/1.2815499.

[16] D.S. Dhawale, G.P. Mane, S. Joseph, S.N. Talapaneni, C. Anand, A. Mano, S.S. Aldeyab, K.S. Lakhi, A. Vinu, Cobalt oxide functionalized nanoporous carbon electrodes and their excellent supercapacitive performance, RSC Adv. 5 (2015) 13930–13940. https://doi.org/10.1039/c4ra14041a.

[17] G. Kim, B.H. Kim, One-dimensional hierarchical porous carbon nanofibers with cobalt oxide in a hollow channel for electrochemical applications, J. Alloys Compd. 910 (2022) 164886. https://doi.org/10.1016/j.jallcom.2022.164886.

[18] R. Ma, Z. Chen, D. Zhao, X. Zhang, J. Zhuo, Y. Yin, X. Wang, G. Yang, F. Yi, Ti3C2T: XMXene for electrode materials of supercapacitors, J. Mater. Chem. A. 9 (2021) 11501–11529. https://doi.org/10.1039/d1ta00681a.

[19] B. Anasori, M.R. Lukatskaya, Y. Gogotsi, 2D metal carbides and nitrides (MXenes) for energy storage, Nat. Rev. Mater. 2 (2017). https://doi.org/10.1038/natrevmats.2016.98.

[20] K. Donthula, R. Vooradi, V.S. Patnaikuni, M. Kakunuri, Binder-free Ruthenium Oxide/MXene/Carbon Nanofiber Ternary Composite Electrode for Supercapacitors, J. Electrochem. Soc. 170 (2023) 030508. https://doi.org/10.1149/1945-7111/acbee5.

[21] P. Huang, S. Zhang, H. Ying, Z. Zhang, W. Han, Few-layered Ti_3C_2 MXene anchoring bimetallic selenide $NiCo_2Se_4$ nanoparticles for superior Sodium-ion batteries, Chem. Eng. J. 417 (2021) 30–36. https://doi.org/10.1016/j.cej.2021.129161.

[22] X. Li, Y. Zhao, Y. Bai, X. Zhao, R. Wang, Y. Huang, Q. Liang, Z. Huang, A Non-Woven Network of Porous Nitrogen-doping Carbon Nanofibers as a Binder-free Electrode for Supercapacitors, Electrochim. Acta. 230 (2017) 445–453. https://doi.org/10.1016/j.electacta.2017.02.030.

[23] N.C. Abeykoon, J.S. Bonso, J.P. Ferraris, Supercapacitor performance of carbon nanofiber electrodes derived from immiscible PAN/PMMA polymer blends, RSC Adv. 5 (2015) 19865–19873. https://doi.org/10.1039/c4ra16594b.

[24] A.D. Jagadale, V.S. Kumbhar, C.D. Lokhande, Supercapacitive activities of potentiodynamically deposited nanoflakes of cobalt oxide (Co_3O_4) thin film electrode, J. Colloid Interface Sci. 406 (2013) 225–230. https://doi.org/10.1016/j.jcis.2013.05.037.

[25] C. V. Niveditha, R. Aswini, M.J. Jabeen Fatima, R. Ramanarayan, N. Pullanjiyot, S. Swaminathan, Feather like highly active Co_3O_4 electrode for supercapacitor application: A potentiodynamic approach, Mater. Res. Express. 5 (2018). https://doi.org/10.1088/2053-1591/aac5a7.

[26] J. Mei, W. Fu, Z. Zhang, X. Jiang, H. Bu, C. Jiang, E. Xie, W. Han, Vertically-aligned Co_3O_4 nanowires interconnected with $Co(OH)_2$ nanosheets as supercapacitor electrode, Energy. 139 (2017) 1153–1158. https://doi.org/10.1016/j.energy.2017.08.014.

[27] X. Li, R. Miao, B. Tao, F. Miao, Y. Zang, P.K. Chu, $Co_3O_4/MnO_2/Co(OH)_2$ on nickel foam composites electrode with excellent electrochemical performance for supercapacitor, Solid State Sci. 95 (2019) 105941. https://doi.org/10.1016/j.solidstatesciences.2019.105941.

[28] L. Zhang, Y. Jiang, L. Wang, C. Zhang, S. Liu, Hierarchical porous carbon nanofibers as binder-free electrode for high-performance supercapacitor, Electrochim. Acta. 196 (2016) 189–196. https://doi.org/10.1016/j.electacta.2016.02.050.

[29] H. Liu, X. Gou, Y. Wang, X. Du, C. Quan, T. Qi, Cauliflower-Like Co_3O_4/Three-Dimensional Graphene Composite for High Performance Supercapacitor Applications, J. Nanomater. 2015 (2015). https://doi.org/10.1155/2015/874245.

[30] W. Liu, H. Fan, W. Shen, S. Qu, Facile and Sustainable Synthesis of Co_3O_4@Hollow-Carbon-Fiber for a Binder-Free Supercapacitor Electrode, ChemistrySelect. 1 (2016) 6469–6475. https://doi.org/10.1002/slct.201601330.

[31] A.S. Levitt, M. Alhabeb, C.B. Hatter, A. Sarycheva, G. Dion, Y. Gogotsi, Electrospun MXene/carbon nanofibers as supercapacitor electrodes, J. Mater. Chem. A. 7 (2019) 269–277. https://doi.org/10.1039/c8ta09810g.

[32] S. Zallouz, B. Réty, L. Vidal, J.M. Le Meins, C. Matei Ghimbeu, Co_3O_4 Nanoparticles Embedded in Mesoporous Carbon for Supercapacitor Applications, ACS Appl. Nano Mater. 4 (2021) 5022–5037. https://doi.org/10.1021/acsanm.1c00522.

[33] Z. Zhu, Y. Zhou, S. Wang, C. Zhao, Z. Li, G. Chen, C. Zhao, Ni counterpart-assisted synthesis of nanoarchitectured Co_3O_4/CoS/$Ni(OH)_2$@Co electrode for superior supercapacitor,Electrochim.Acta.284(2018)444–453. https://doi.org/10.1016/j.electacta.2018.07.199.

[34] S. Li, K. Yang, P. Ye, K. Ma, Z. Zhang, Q. Huang, Three-dimensional porous carbon/Co_3O_4 composites derived from graphene/Co-MOF for high performance supercapacitor electrodes,Appl.Surf.Sci.503(2020) 144090. https://doi.org/10.1016/j.apsusc.2019.144090.

[35] D.K. Kim, M. Hwang, D. Ko, J. Kang, K. dong Seong, Y. Piao, Electrochemical performance of 3D porous Ni-Co oxide with electrochemically exfoliated graphene for asymmetric supercapacitor applications, Electrochim. Acta. 246 (2017) 680–688. https://doi.org/10.1016/j.electacta.2017.06.099.

[36] J. Zhu, Q. Zhang, L. guo, Y. Zhao, R. Zhang, L. Liu, J. Yu, Highly flexible, freestanding supercapacitor electrodes based on hollow hierarchical porous carbon nanofibers bridgedbycarbonnanotubes,Chem.Eng.J.434(2022)134662. https://doi.org/10.1016/j.cej.2022.134662.

[37] C. Wang, F. Zhu, G. Wang, M. Xiao, Y. Meng, Y. Zhang, Co_3O_4/carbon nano-onions composite as supercapacitor electrode and its excellent electrochemical performance, Int. J. Mater. Res. 109 (2018) 873–879. https://doi.org/10.3139/146.111682.

[38] M.H. Yang, B.G. Choi, Preparation of Three-Dimensional Co_3O_4/graphene Composite for High-Performance Supercapacitors, Chem. Eng. Commun. 204 (2017) 723–728. https://doi.org/10.1080/00986445.2016.1277523.

[39] J. Li, G.X. Xu, Research progress on applications of Polyaniline(PANI) for Electrochemical Energy Storage and Conversion, 2020. https://doi.org/10.3980/j.issn.1672-5123.2017.9.12.

[40] M. Yanilmaz, M. Dirican, A.M. Asiri, X. Zhang, Flexible polyaniline-carbon nanofiber supercapacitor electrodes, J. Energy Storage. 24 (2019) 100766. https://doi.org/10.1016/j.est.2019.100766.

[41] S. Abouali, M. Akbari Garakani, B. Zhang, Z.L. Xu, E. Kamali Heidari, J.Q. Huang, J. Huang, J.K. Kim, Electrospun Carbon Nanofibers with in Situ Encapsulated Co_3O_4 Nanoparticles as Electrodes for High-Performance Supercapacitors, ACS Appl. Mater. Interfaces. 7 (2015) 13503–13511. https://doi.org/10.1021/acsami.5b02787.

[42] Y. Zhao, Y. Liu, J. Du, X. Zhang, J. Zhou, X. Li, C. Wu, Z. Zhu, E. Xie, X. Pan, Facile synthesis of interconnected carbon network decorated with Co_3O_4 nanoparticles for potential supercapacitor applications, Appl. Surf. Sci. 487 (2019) 442–451. https://doi.org/10.1016/j.apsusc.2019.05.142.

[43] I. Rabani, J. Yoo, H.S. Kim, D. Van Lam, S. Hussain, K. Karuppasamy, Y.S. Seo, Highly dispersive Co_3O_4 nanoparticles incorporated into a cellulose nanofiber for a high-performance flexible supercapacitor, Nanoscale. 13 (2021) 355–370. https://doi.org/10.1039/d0nr06982e.

Chapter-V

Facile synthesis of Cobalt-MOF/MXene/carbon nanofiber electrodes

5.1 Literature Review

In recent years, the fast growth of flexible and wearable electronics has greatly raised the need for flexible energy storage and conversion devices. Supercapacitors (SC) are particularly useful in this regard because of their ultra-long cycle life, fast charging-discharging rate, safety to use, and ability to achieve higher power density[1,2]. Flexible supercapacitors can be promising resources for such wearable and flexible electronic gadgets. However, the biggest difficulty in key to manufacturing SCs is to make flexible electrodes without dropping their electrochemical features. A variety of electroactive materials, such as conducting polymers, metal nanoparticles, graphene, MXene, and their composites, have been considered as porous and high-performance flexible electrodes[3–5]. In particular, the two-dimensional layered metal carbide ($Ti_3C_2T_x$), which is also known as MXene, has gained considerable attention as a potential electrochemical energy storage material due to its high electrical conductivity and hydrophilicity. However, in preparing MXene-based flexible film electrodes, synthesized MXene nanosheets are susceptible to restacking. Hence, these 2D materials are often embedded into other materials such as carbon nanofibers, aerogels, etc.[6]. These composites enhanced specific capacitance, wettability, electrical conductivity and flexibility of the electrode materials. [7]

Moreover, there has been a notable focus on materials derived from Metal-Organic Frameworks (MOFs) in recent supercapacitor research. This interest is driven by their potential for achieving high specific energy storage density, thanks to their exceptional surface area. The coordination structures formed by combining metal ions with organic ligands in MOFs result in structures with extremely high surface areas. By exposing MOF nanoparticles to intense pyrolytic heat, we attain their carbonization while preserving the specific surface area. This process ensures the uniform distribution of metal oxide sites within the porous carbon framework [7,8]. This elevated SSA (specific surface area) of the material has the potential to boost charge storage rates, as it actively participates in EDLC at the interface of the electrode and electrolyte. Under optimal carbonization conditions, MOFs maintain their structures and ion diffusion channels within their host frameworks. Numerous studies have explored MOFs and their composites as electrodes for energy storage, particularly in lithium-ion batteries, due to their enticing combination of high SSA and porosity. In the realm of MOFs, zeolitic imidazolate framework (ZIF-8) distinguishes itself with remarkable thermal and chemical stability, adjustable pore size, and inherent flexibility. The design of ZIF-8, featuring

coordinated Zn^{2+} tetrahedral and coupled imidazolate N atoms, additionally holds the promise of superior ion adsorption and energy storage capabilities. Nevertheless, the investigation of composites derived from ZIF-8 as flexible electrodes for supercapacitors is currently in its emerging phase [9][10]. Shao et al. detailed the synthesis of Ni@MOF with distorted crystal structures using a solvothermal process involving Ni-nitrate hexahydrate and 2,5-dihydroxyterephthalic acid. Theoretically, Ni^{2+} is expected to maintain the topology to sustain the ordered coordination of the MOF [11]. Because of their outstanding EDLC qualities, low cost, wide potential range, and environmentally friendly, cobalt-based compound materials are generally attractive for the application of supercapacitors [12,13]. Moreover, introducing heteroatoms into MOFs has the potential to modify the electron transport properties of carbon compounds, thereby augmenting interfacial capacitance. This has led to the exploration of Ni and based MOFs combined with CNTs (Ni-MOF/CNTs) to enhance the performance of electrode material and shown a specific capacitance of 103 F g^{-1} at current density of 0.5 A g^{-1} as electrode for supercapacitor applications [14]. In another work, Ni/Co-MOFs nanoparticles were combined with materials like reduced graphene(rGO) and the composite Ni/Co-MOF-rGO was shown improved electrochemical performance with specific capacitance of 181 F g^{-1} at current density of 1 A g^{-1}[15]. Nevertheless, there is a notable absence of studies focused on ternary composites involving MOF, MXene, and carbon nanofibers. Consequently, this chapter is dedicated to unraveling the synergistic effects arising from the incorporation of MXene and MOF into membranes based on carbon nanofibers. Both binary and ternary composite electrochemical performances were analyzed to assess the influence of MOF and MXene. The freestanding supercapacitor electrode, composed of Co-MOF/MXene/carbon nanofiber, significantly enhanced charge transfer and boosted ion adsorption. Remarkably, this freestanding supercapacitor electrode demonstrates exceptional electrochemical stability even under high current densities and extended cycling periods.

5.1. Experimental

2-methylimidazole (2MI, 2MI, $C_4H_6N_2$,99%), Cobalt nitrate hexahydrate ($Co(NO_3)_6 \cdot 6H_2O$), and polyacrylonitrile (PAN, Mw = 1,50,000) chemicals were acquired from Sigma Aldrich India. Titanium aluminum carbide (Ti_3AlC_2, 99% MAX phase) was sourced from Arizona Chemical Co. Ltd., India. The solvents, methanol (CH_3OH) and N, N-dimethylformamide (DMF, 99.8%), were obtained from Merck Chemicals and SRL-Chemicals, India, respectively, and were used without further purification.

5.1.2. Preparation of Co-MOF nanoparticles

In the initial step, cobalt nitrate hexahydrate (8 mmol) was dissolved in 200 mL of DMF. Simultaneously, 28 mmol of 2-methyl imidazole was dissolved in 200 ml of DMF in a separate reagent bottle. The two solutions were then stirred together for 5 minutes in a large reagent bottle. After allowing the covered reagent bottle to react for 12 hours, a misty, purple solution and a dark purple precipitate were formed. Subsequently, the solution was promptly centrifuged at 5500 rpm for 10 minutes, subjected to repeated washing, and dried at 70 ℃ for 12 hours. The same procedure was repeated using methanol as the solvent to synthesize Co-MOF nanoparticles.

5.1.3 Synthesis of MXene/CNF composite electrode

To obtain the precursor polymer solution, PAN (12 wt.%) was gradually introduced to MXene-dispersed colloidal solution, prepared like our previous work discussed in chapter 2 [14]. Employing an 18-gauge needle, an electrospinning process was conducted using a plastic syringe filled with the MXene/PAN solution. Electrospinning from polymer precursors was achieved with a feed flow rate of 1 ml h^{-1} and a voltage of 16 kV, while maintaining a tip-to-collector distance of 12 cm. After collecting nanofibers for six hours on aluminum foil-wrapped rotating drums (400 rpm), the deposited fiber mat was peeled off the aluminum foil. The mat underwent stabilization at 250 °C for 2 hours before being carbonized at 900 °C side a tubular furnace. For the fabrication of flexible MXene/CNF composite electrodes, the furnace was heated to 900 °C with a ramp rate of 5 °C per minute after stabilization, held there for 2 h, and then gradually cooled to room temperature[15].

5.1.4 Synthesis of Co-MOF/MXene/CNF composite electrode

First delaminated MXene nanosheets synthesized using probe sonication of 0.3 g of as-prepared $Ti_3C_2T_x$ flakes in 12 ml of DMF for 2 hours. To make the electrospinning solution, delaminated MXene solution was then mixed with 0.94 g of PAN polymer and 0.8 g of as-prepared Co-MOF and then agitated for 8 hours. A violet color viscous electrospinning solution was produced after thoroughly dissolving the PAN polymer. Subsequently, a straightforward single-step electrospinning process was used to produce nanofibers. The prepared viscous Co-MOF/MXene/PAN polymer solution was loaded into a 10 ml syringe connected to an 18-gauge needle for electrospinning. The polymer solution flow rate was optimized at 1 mL/h to maintain the cone-jet and generate consistent nanofibers, while a high potential of 16 kV was applied at the needle tip, maintaining a 12 cm distance between the drum collector and the needle tip.

This nanofibrous electrode underwent stabilization at 250 ℃ followed by carbonization at 900 ℃ as discussed in the previous section.

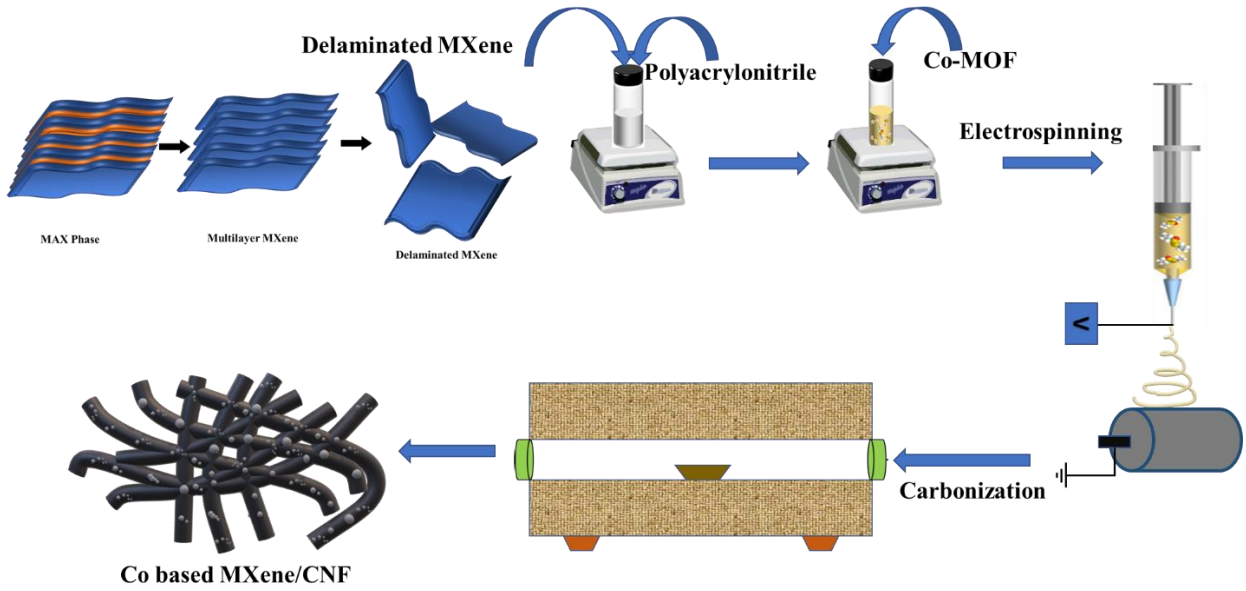

Fig.5.1 Schematic for synthesis of Co-MOF and MXene embedded CNF composite

5.3 Results and discussion

5.3.1 Physicochemical properties of Co-MOF/MXene/CNF and MXene/CNF

5.3.1.1 FESEM analysis of Co-MOF/MXene/CNF and MXene/CNF

The FESEM images of Co-MOF nanoparticles shown in 5.2(a) and 5.2(b) exhibit higher magnification and lower magnification, respectively. The FESEM images suggest that methanol, employed as a solvent for MOF preparation, resulted in a well-defined morphology. This is attributed to methanol being a less polar solvent, facilitating the formation of more distinct MOF crystals. Additionally, methanol is less prone to react with the MOF material, contributing to the preservation of its morphology [16].

Additionally, the FESEM technique was utilized to examine the intricate surface morphology of the ternary composite nanofibrous electrode. Fig. 5.3 (a&b) presents FESEM images of the surface of the ternary composite. In the higher magnification FESEM images shown in Fig. 5.3b, the Co-MOF nanoparticles are intricately embedded within CNF structures, indicating improved adhesion of Co-MOF. The Co-MOF forms a connected network with a hierarchically porous structure, leading to an increased specific surface area (SSA) and the exposure of electrochemically active sites.

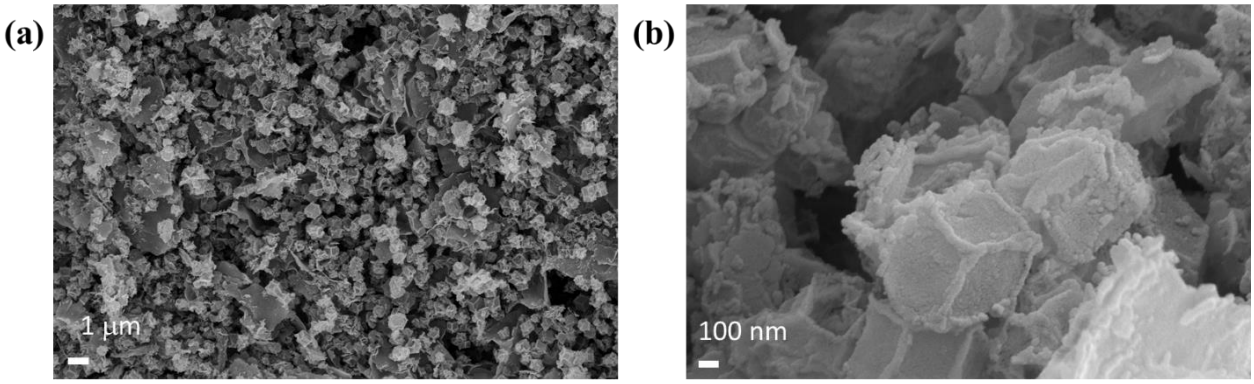

Figure.5.2 (a) and (b) FESEM images with higher magnification and lower images of Co-MOF in DMF as solvent (c) and (d) FESEM images with higher magnification and lower images of Co-MOF in Methanol as solvent

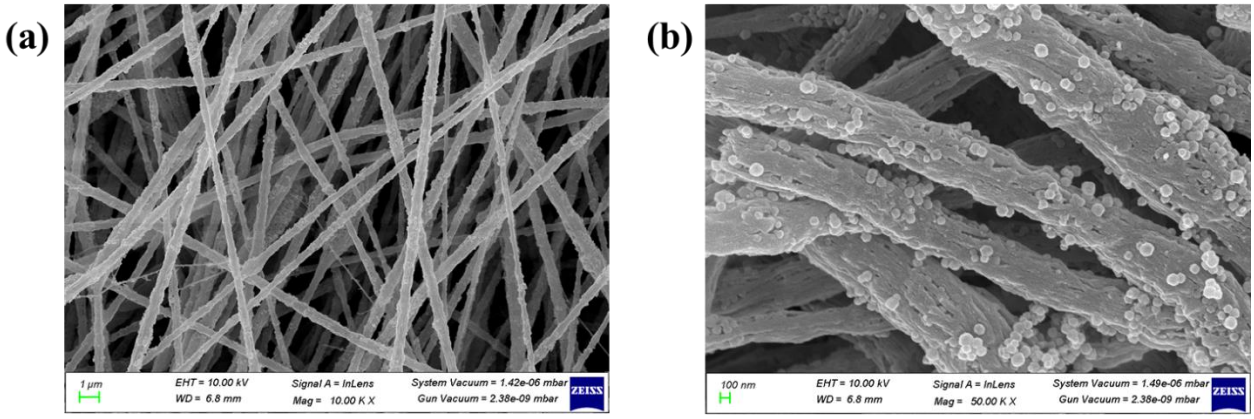

Figure.5.3 (a) &(b) FESEM images of Co-MOF/MXene/CNF at lower and higher magnification

5.3.1.2 HR-TEM analysis of Co-MOF/MXene/CNF and MXene/CNF

For additional confirmation of the MOF particle embedding, we conducted HRTEM imaging of the Co-MOF/MXene/CNF ternary composites. The HRTEM analysis validated the embedding of Co-MOFs both on the surface and inside CNFs, as depicted in Fig. 5.4 (a-d). MXene embedded layers are smaller than Co-MOF particles and are randomly distributed as layers post delamination. Consequently, the size of MXene particles may be challenging to distinguish in a TEM image due to their lower loading compared to Co-MOF. The varied morphologies observed indicate a significant impact of MXene on the binding of Co-MOF within CNFs.

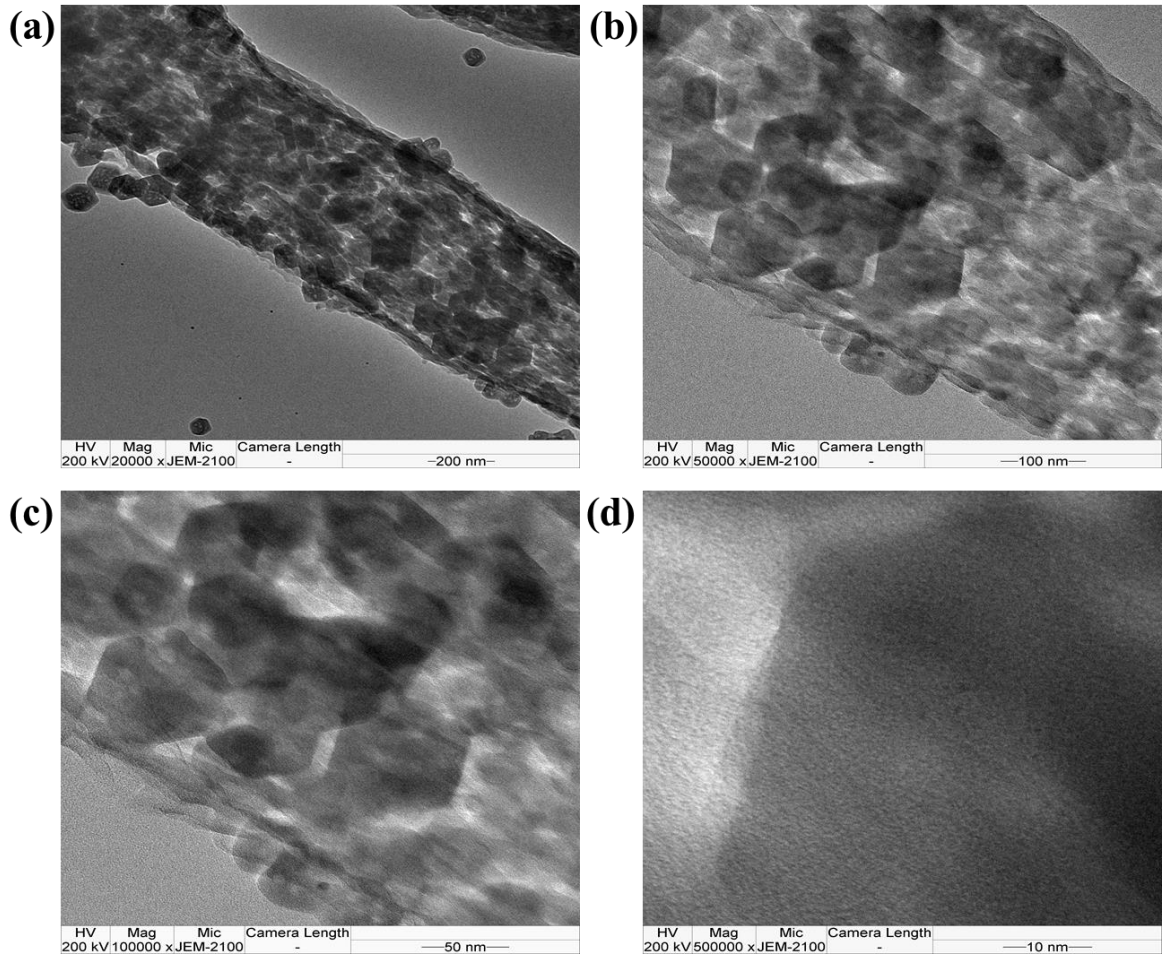

Figure.5.4 (a-d) HR-TEM images of Co-MOF/MXene/CNF

5.3.1.3 XRD analysis of Co-MOF/MXene/CNF and MXene/CNF

The samples obtained were subjected to XRD analysis to determine their crystal structures. The Co-MOF nanoparticles exhibited identical diffraction peaks, as illustrated in Fig. 5.5a, aligning with the previously reported XRD patterns of Co-MOF [16]. The XRD patterns of the ternary composite containing Co-MOFs and MXene embedded in CNFs displayed characteristic peaks similar to each other. Additionally, as depicted in Fig. 5.5a, an observed peak at 25.6° is linked to the amorphous nature of CNF [17]. Apart from the CNF peaks, the remaining peaks align well with the crystalline peaks of Co-MOF [18].

5.3.1.4 FTIR analysis of Co-MOF/MXene/CNF and MXene/CNF

A comparative analysis of the FTIR spectra for MXene/CNF and Co-MOF/MXene/CNF composites was conducted to characterize the functional groups and the coordination mechanism of MXene, CNF, and Co-MOF. As depicted in Fig. 5.5b, the intense bands at 1585 and 1419 cm^{-1} correspond to symmetric stretching modes of C-C and C=C, respectively. Additionally, the 484 cm^{-1} band indicates stretching attributed to Co and N, affirming the

presence of a coordination mode in the ligands and the Co ions. The stretching vibrations of -OH and aromatic C-H groups are represented by the 3593 and 1505 cm^{-1} bands, respectively [19].

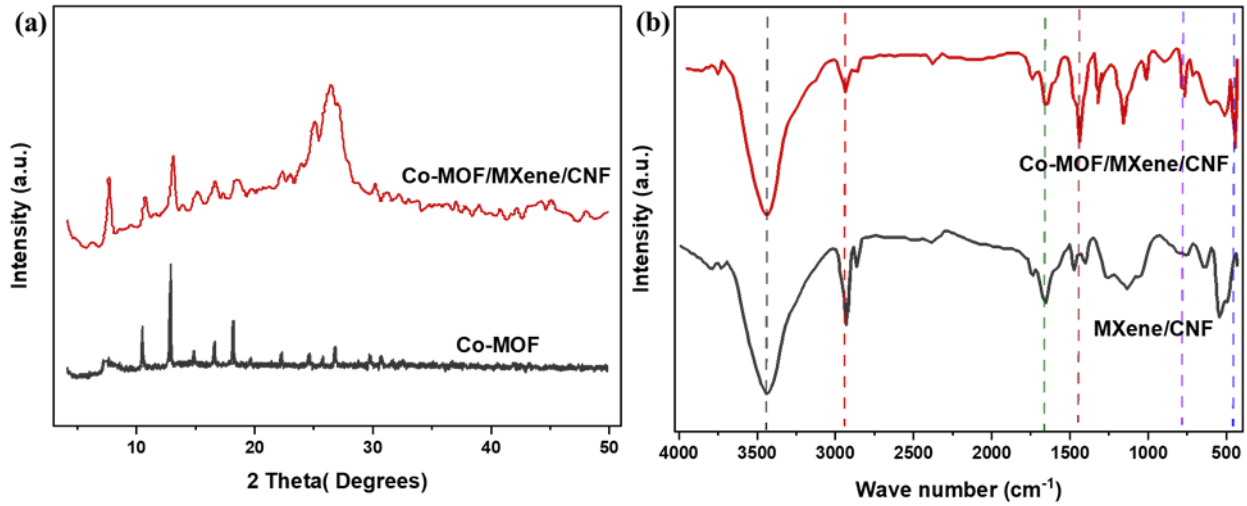

Figure 5.5(a) XRD comparison of Co-MOF and Ternary composite (b) FTIR spectra comparison for Ternary and binary composite.

5.3.1.5 BET analysis of Co-MOF/MXene/CNF and MXene/CNF

The N_2 absorption-deposition isotherms were employed to assess the surface area and pore distribution of the composite electrodes. In Fig. 5.6a, a distinct type-IV isotherm is evident for both ternary and binary composites, with a noticeable hysteresis loop in the P/P_0 range between 0 and 1, indicating the presence of both mesopores and micropores. According to BET results, the surface area of Co-MOF/MXene/CNF is 224 $m^2 g^{-1}$, while MXene/CNF has a surface area of 169 $m^2 g^{-1}$. The analysis of pore size distribution, as depicted in Fig.5.6 (b), reveals that Co-MOF/MXene/CNF exhibits mesopores with a size of ~6.6 nm, whereas MXene/CNF displays larger mesopore sizes of 20.5 nm. Co-MOF/MXene/CNF predominantly features microporous structures, followed by mesoporous structures. The introduction of Co-MOF nanoparticles into the composite material gradually increases the size of the porous structure, as Co-MOF nanoparticles have the ability to self-assemble into larger structures, thereby creating larger pores in the composite material [20,21].

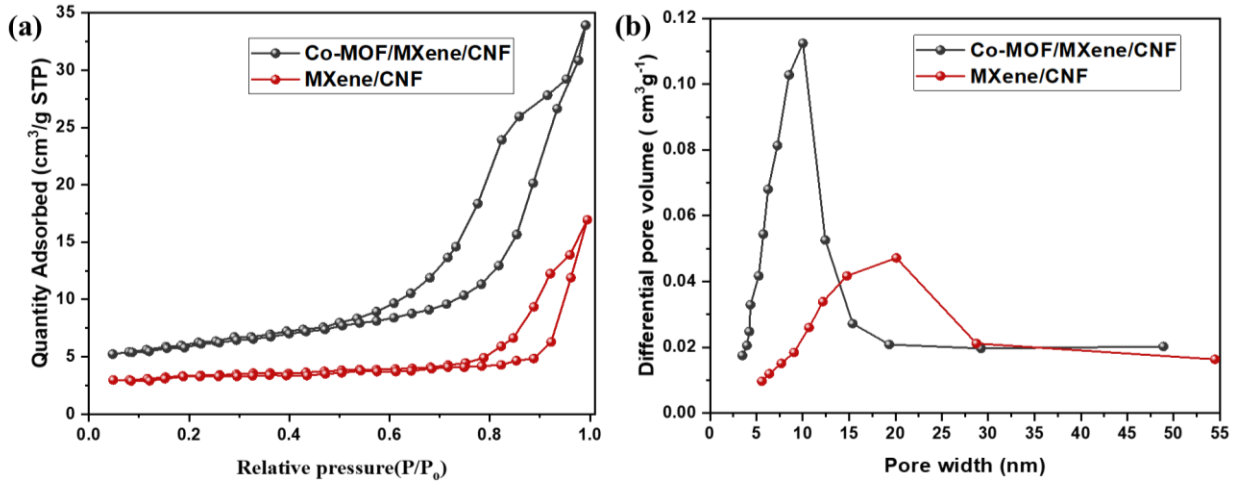

Figure.5.6. (a) N_2 absorption-desorption isotherms and (b) pore size distribution of Co-MOF/MXene/CNF and MXene/CNF

5.3.2. Electrochemical Characterization

Electrochemical performance tests, including Cyclic voltammetry (CV), Galvanostatic Charge Discharge (GCD), and Electrochemical Impedance Spectroscopy (EIS), were conducted on Co-MOF/MXene/CNF and MXene/CNF composite electrodes using symmetric cell assembly, to gain in-depth insights into the influence of various materials, including Co-MOF and MXene, integrated into CNFs on electrochemical behavior. Both MXene/CNF and Co-MOF/MXene/CNF serve as EDLC-type electrode materials, contributing to their energy storage capacity.

5.3.2.1 CV analysis of Co-MOF/MXene/CNF and MXene/CNF

The Cyclic voltammogram comparison for ternary and binary shown in Fig.5.7 (a) and ternary composite showed more area enclosed by the CV curve because of high surface area and more mesopore volume of possessed by Co-MOF [22]. The CV curves of Co-MOF/MXene/CNF at various sweep rates are shown in Fig.5.7b. The symmetric forms of CV curves stay consistent when the scan rate increased from 5 to 100 mV s^{-1}, demonstrating the superior reversibility of composite electrode. Among these, the CV curve of Co-MOF/MXene/CNF at 100 mV s^{-1} has the biggest enclosed area, suggesting the highest specific capacitance. A high scanning speed induced insufficient diffusion reaction, which moderated the specific capacitance due to increased internal diffusion resistance.

5.3.2.2 GCD analysis of Co-MOF/MXene/CNF and MXene/CNF

The galvanostatic charging-discharging plots recorded and comparison curves were EDLC in nature, as demonstrated in Fig.5.7d. Furthermore, the GCD performance was recorded using Co-MOF/MXene/CNF electrodes as shown in Fig.5.7c at different current densities. Symmetric capacitors with MXene/CNF, and Co-MOF/MXene/CNF electrodes exhibited specific capacitances as 149, and 215.7 F g^{-1} at 1 A g^{-1}, respectively. The electron storage capacitance of Co-MOF/MXene/CNF surpasses that of binary electrodes due to the uniform loading of Co-MOF and the introduction of Co from the exterior to the interior. These characteristics can be attributed to the structure of Co-MOF. Fig. 5.8a illustrates the GCD curves of Co-MOF/MXene/CNF at various current densities, ranging from 1 to 10 A g^{-1}. The specific capacitance of Co-MOF/MXene/CNF and MXene/CNF remains consistently high, with values of 47.5% and 41.3%, respectively, indicating that the inclusion of MXene nanosheets in the CNFs contributes to their enhanced supercapacitor performance.

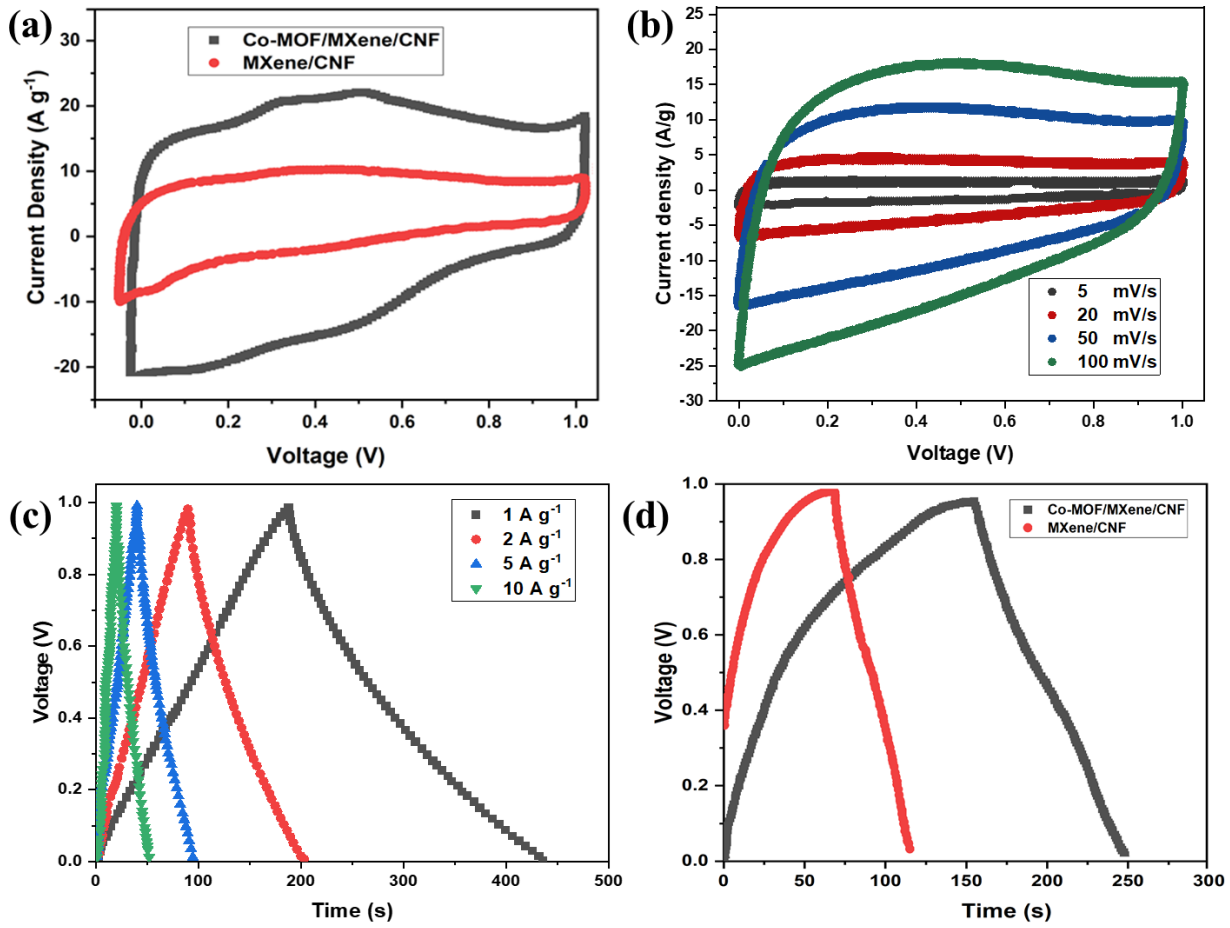

Figure.5.7(a) CV curves comparison for ternary and binary composite (b) CV curve comparison for ternary composite at various scan rates (c) GCD comparison for ternary

composite at various current density (d) GCD comparison or binary and ternary composite at current density of 1 A g^{-1}

5.3.2.3 EIS analysis of Co-MOF/MXene/CNF and MXene/CNF

EIS technique deployed on symmetrical supercapacitor fabricated using Co-MOF/MXene/CNF and MXene/CNF composite electrodes to investigate their internal resistance and ion diffusion properties. As depicted in Fig.5.8c, MXene/CNF exhibits lower charge transfer resistance and diffusion resistance, this is attributed to the improved electrical conductivity resulting from the doping of MXene nanosheets in binary composite electrodes. The highly hierarchical connected network of CNF structures, exposes abundant active sites and provides large specific surface areas, thereby enhancing ion transport. Additionally, the incorporation of Co-MOF nanoparticles contributes to increased charge transfer resistance and diffusional resistance, because of less electrical conductivity of Co-MOF particles. Furthermore, Co-MOF/MXene/CNF composite showed more internal resistance compared to binary composite and its better when compared with Co-MOF/CNFs composite [23,24].

Energy density (E) and Power density (P) of the symmetrical SC devices were calculated from GCD recorded values of ternary and binary composites at different current densities. The maximum energy density at 1 A g^{-1} is 33.0 Wh kg^{-1}, and the corresponding power density is 440.5 W kg^{-1}, which are promising than MXene/CNF symmetric SC device as shown in Fig.5.8d, and as well as previously reported. At 1 A g^{-1}, the MXene/CNF symmetric SC device achieved a high-power density of 451.8 W kg^{-1} at an energy density of 18.1 Wh kg^{-1}. Furthermore, when joined in series, Co-MOF/MXene/CNF SC may light up a red LED. As time passes, the brightness of the LED decreases, as seen in Fig.5.8b.

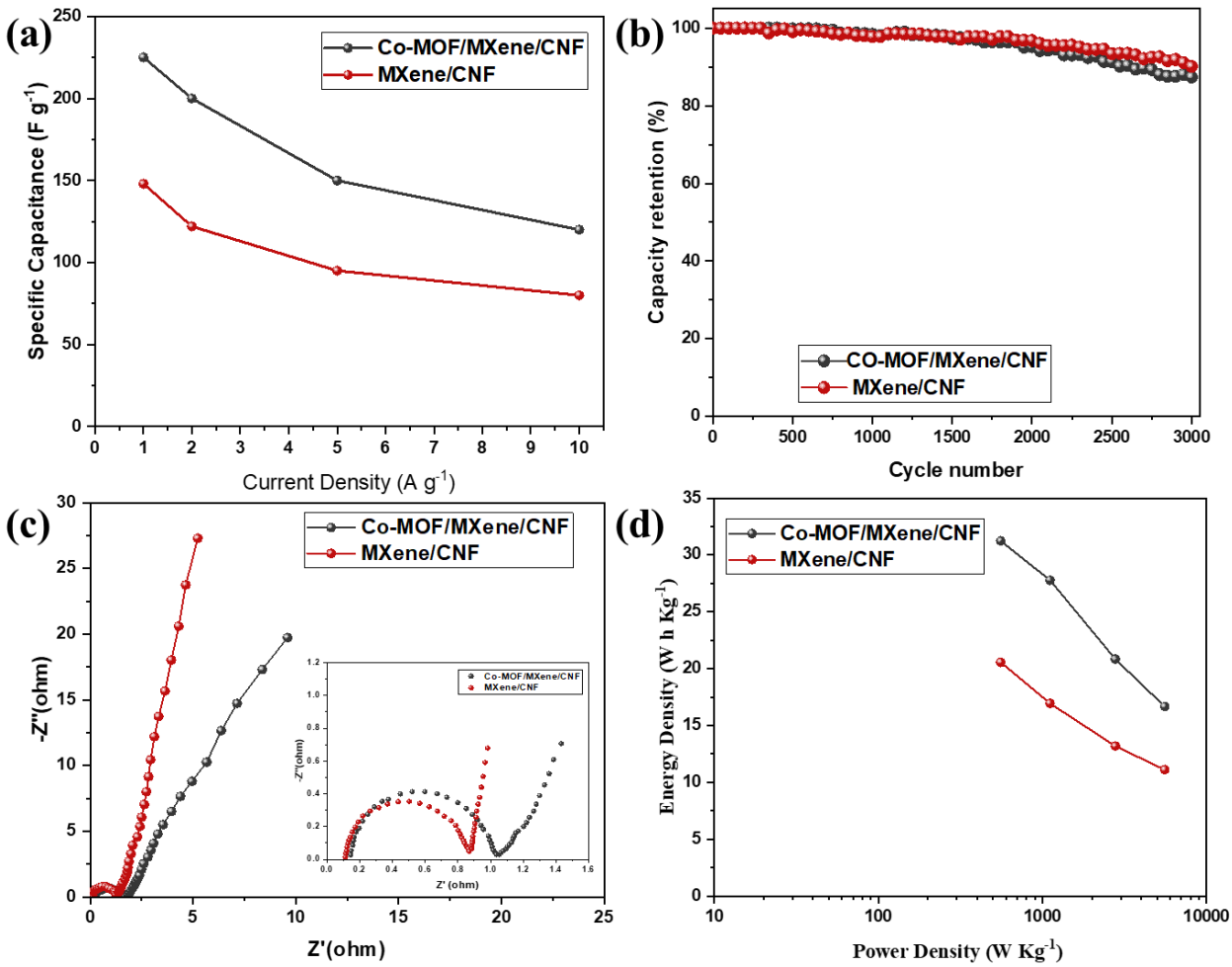

Figure 5.8(a) Specific capacitance values of Co-MOF/MXene/CNF and MXene/CNF composites at different current densities (b) capacitance retention (%) curves comparison for HMCNF and Co_3O_4/HMCNF electrodes (c) Nyquist plot for Co-MOF/MXene/CNF and MXene/CNF composites (d) Ragone plot comparison for Co-MOF/MXene/CNF and MXene/CNF.

Cycle stability of the Co-MOF/MXene/CNF symmetrical SC system were investigated 3000 cycles at the current density of 1 A $g^{-1,}$ the capacitance retention can remain over 91 %, as shown in Fig.5.8b. The stability in capacitance retention can be ascribed to the Co-MOF EDLC electrochemical process, stemming from its substantial specific surface areas. Simultaneously, the space provided by the Co-MOF structure mitigates material volume expansion during charging and discharging, a crucial factor for ensuring the durability of electrode materials. Additionally, we have also compared the electrochemical performance of the ternary composite with existing binary and ternary composite electrodes in the table below. The specific capacitance is higher than most of the binary and ternary MOF-based composite electrodes and comparable with the Co/Ni-MOF.

Table 5.1 Comparison for various MOF based composites performances

Electrode materials	**Electrolyte**	**SSA (m^2 g^{-1})**	**Specific capacitances**
Ni-MOF [25]	2M KOH	6.5	95 F g^{-1} at 1 A g^{-1}
Ni-MOF [26]	2M KOH	40	87 F g^{-1} at 0.5 A g^{-1}
Co/Ni-MOF [27]	3M KOH	404	211 F g^{-1} at 1 A g^{-1}
Ni,Co-MOF [28]	2M KOH	54	158 F g^{-1} at 0.5 A g^{-1}
Ni-MOF/CNTs [29]	6M KOH	41	103 F g^{-1} at 0.5 A g^{-1}
Zn/Ni-MOF@PPy [30]	3M KOH	-	160 F g^{-1} at 1 A g^{-1}
Ni/Co-MOF-rGO [31]	6M KOH	-	181 F g^{-1} at 1 A g^{-1}
Co-MOF/MXene/CNF	6M KOH	224	215.7 F g^{-1} at 1 A g^{-1}

5.4 Conclusion

In conclusion, we have devised a simple method to create Co-MOFs embedded in MXene/CNF with a hierarchical porous structure, surpassing the electrochemical performance of Co-MOFs produced on CNFs. The incorporation of Co-MOF nanoparticles into CNFs not only enhances graphitization but also provides a larger surface area, leading to improved conductivity. As a result, Co-MOF/MXene/CNF demonstrates a superior specific capacitance of 215.7 F g^{-1}. Additionally, the symmetric supercapacitor based on Co-MOF/MXene/CNF exhibits an energy density of 33.0 Wh kg^{-1} at a power density of 440.5 W kg^{-1} and remarkable cyclic stability over 3000 charging-discharging cycles. This study outlines an innovative approach for the integration of Co-MOF nanoparticles into MXene/CNFs, presenting a novel pathway for the development of Co-MOF-doped materials with potential applications in a wide range of energy storage and conversion systems.

5.5 References

[1] X. Wang, X. Lu, B. Liu, D. Chen, Y. Tong, G. Shen, Flexible energy-storage devices: Design consideration and recent progress, Adv. Mater. 26 (2014) 4763–4782. https://doi.org/10.1002/adma.201400910.

[2] C. Yu, J. An, Q. Chen, J. Zhou, W. Huang, Y.J. Kim, G. Sun, Recent Advances in Design of Flexible Electrodes for Miniaturized Supercapacitors, Small Methods. 4 (2020) 1–31. https://doi.org/10.1002/smtd.201900824.

[3] L. Feng, N. Xie, J. Zhong, Carbon nanofibers and their composites: A review of synthesizing, properties and applications, Materials (Basel). 7 (2014) 3919–3945.

https://doi.org/10.3390/ma7053919.

[4] B. Joshi, E. Samuel, Y. il Kim, A.L. Yarin, M.T. Swihart, S.S. Yoon, Review of recent progress in electrospinning-derived freestanding and binder-free electrodes for supercapacitors, Coord. Chem. Rev. 460 (2022) 214466. https://doi.org/10.1016/j.ccr.2022.214466.

[5] M.A.A. Mohd Abdah, N.H.N. Azman, S. Kulandaivalu, Y. Sulaiman, Review of the use of transition-metal-oxide and conducting polymer-based fibres for high-performance supercapacitors, Mater. Des. 186 (2020) 108199. https://doi.org/10.1016/j.matdes.2019.108199.

[6] J. Orangi, M. Beidaghi, A Review of the Effects of Electrode Fabrication and Assembly Processes on the Structure and Electrochemical Performance of 2D MXenes, Adv. Funct. Mater. 30 (2020) 1–22. https://doi.org/10.1002/adfm.202005305.

[7] W. Li, X. Zhao, Q. Bi, Q. Ma, L. Han, K. Tao, Recent advances in metal-organic framework-based electrode materials for supercapacitors, Dalt. Trans. 50 (2021) 11701–11710. https://doi.org/10.1039/d1dt02066h.

[8] D. Tian, C. Wang, X. Lu, Metal–Organic Frameworks and Their Derived Functional Materials for Supercapacitor Electrode Application, Adv. Energy Sustain. Res. 2 (2021). https://doi.org/10.1002/aesr.202100024.

[9] K. Chhetri, A. Adhikari, J. Kunwar, D. Acharya, R.M. Bhattarai, Y.S. Mok, A. Adhikari, A.P. Yadav, H.Y. Kim, Recent Research Trends on Zeolitic Imidazolate Framework-8 and Zeolitic Imidazolate Framework-67-Based Hybrid Nanocomposites for Supercapacitor Application, Int. J. Energy Res. 2023 (2023) 1–46. https://doi.org/10.1155/2023/8885207.

[10] M. Kim, X. Xu, R. Xin, J. Earnshaw, A. Ashok, J. Kim, T. Park, A.K. Nanjundan, W.A. El-Said, J.W. Yi, J. Na, Y. Yamauchi, KOH-Activated Hollow ZIF-8 Derived Porous Carbon: Nanoarchitectured Control for Upgraded Capacitive Deionization and Supercapacitor, ACS Appl. Mater. Interfaces. 13 (2021) 52034–52043. https://doi.org/10.1021/acsami.1c09107.

[11] S.R. Wu, J.B. Liu, H. Wang, H. Yan, NiO@ graphite carbon nanocomposites derived from Ni-MOFs as supercapacitor electrodes, Ionics (Kiel). 25 (2019) 1–8. https://doi.org/10.1007/s11581-018-2812-z.

[12] D.G. Wang, Z. Liang, S. Gao, C. Qu, R. Zou, Metal-organic framework-based materials for hybrid supercapacitor application, Coord. Chem. Rev. 404 (2020) 213093. https://doi.org/10.1016/j.ccr.2019.213093.

[13] B. Xu, H. Zhang, H. Mei, D. Sun, Recent progress in metal-organic framework-based supercapacitor electrode materials, Coord. Chem. Rev. 420 (2020) 213438. https://doi.org/10.1016/j.ccr.2020.213438.

[14] K. Donthula, R. Vooradi, V.S. Patnaikuni, M. Kakunuri, Binder-free Ruthenium Oxide/MXene/Carbon Nanofiber Ternary Composite Electrode for Supercapacitors, J. Electrochem. Soc. 170 (2023) 030508. https://doi.org/10.1149/1945-7111/acbee5.

[15] K. Donthula, U.R. Malothu, R. Araga, R. Vooradi, V.S. Patnaikuni, M. V. Reddy, M. Kakunuri, Flexible polyaniline/MXene/CNF composite nanofibrous mats as high-performance supercapacitor electrodes, Polym. Compos. (2023) 1–14. https://doi.org/10.1002/pc.27646.

[16] Y. Wang, L. Ma, F. Xu, R. Ren, J. Wang, C. Hou, Ternary ZIF-67/MXene/CNF aerogels for enhanced photocatalytic TBBPA degradation via peroxymonosulfate activation, Carbohydr. Polym. 298 (2022) 120100. https://doi.org/10.1016/j.carbpol.2022.120100.

[17] S. Ghosh, W.D. Yong, E.M. Jin, S.R. Polaki, S.M. Jeong, H. Jun, Mesoporous carbon nanofiber engineered for improved supercapacitor performance, Korean J. Chem. Eng. 36 (2019) 312–320. https://doi.org/10.1007/s11814-018-0199-1.

[18] S. Li, K. Yang, P. Ye, K. Ma, Z. Zhang, Q. Huang, Three-dimensional porous carbon/Co3O4 composites derived from graphene/Co-MOF for high performance supercapacitor electrodes, Appl. Surf. Sci. 503 (2020) 144090. https://doi.org/10.1016/j.apsusc.2019.144090.

[19] K. Liu, W. Zhang, M. Tang, Z. Wang, Y. Yang, S. Li, H. Long, NiCo2O4 nanosheet stereostructure with N-doped carbon/Co array supports derived from Co-MOF for asymmetric supercapacitor, J. Electroanal. Chem. 923 (2022) 116818. https://doi.org/10.1016/j.jelechem.2022.116818.

[20] R.A. Senthil, S. Osman, J. Pan, X. Liu, Y. Wu, Recent progress on porous carbon derived from Zn and Al based metal-organic frameworks as advanced materials for supercapacitor applications, J. Energy Storage. 44 (2021) 103263. https://doi.org/10.1016/j.est.2021.103263.

[21] P.G. Raje, S.R. Gurav, M.R. Waikar, A.S. Rasal, J.Y. Chang, R.G. Sonkawade, The review of different dimensionalities based pristine metal organic frameworks for supercapacitor application, J. Energy Storage. 56 (2022) 105700. https://doi.org/10.1016/j.est.2022.105700.

[22] J. Pokharel, A. Gurung, A. Baniya, W. He, K. Chen, R. Pathak, B.S. Lamsal, N. Ghimire, Y. Zhou, MOF-derived hierarchical carbon network as an extremely-high-performance

supercapacitor electrode, Electrochim. Acta. 394 (2021) 139058. https://doi.org/10.1016/j.electacta.2021.139058.

[23] X. Zhang, S. Yang, W. Lu, D. Lei, Y. Tian, M. Guo, P. Mi, N. Qu, Y. Zhao, MXenes induced formation of Ni-MOF microbelts for high-performance supercapacitors, J. Colloid Interface Sci. 592 (2021) 95–102. https://doi.org/10.1016/j.jcis.2021.02.042.

[24] G. Zhu, H. Wen, M. Ma, W. Wang, L. Yang, L. Wang, X. Shi, X. Cheng, X. Sun, Y. Yao, A self-supported hierarchical Co-MOF as a supercapacitor electrode with ultrahigh areal capacitance and excellent rate performance, Chem. Commun. 54 (2018) 10499–10502. https://doi.org/10.1039/c8cc03669a.

[25] S. Gao, Y. Sui, F. Wei, J. Qi, Q. Meng, Y. He, Facile synthesis of cuboid Ni-MOF for high-performance supercapacitors, J. Mater. Sci. 53 (2018) 6807–6818. https://doi.org/10.1007/s10853-018-2005-1.

[26] P. Du, Y. Dong, C. Liu, W. Wei, D. Liu, P. Liu, Fabrication of hierarchical porous nickel based metal-organic framework (Ni-MOF) constructed with nanosheets as novel pseudo-capacitive material for asymmetric supercapacitor, J. Colloid Interface Sci. 518 (2018) 57–68. https://doi.org/10.1016/j.jcis.2018.02.010.

[27] Y. Jiao, J. Pei, D. Chen, C. Yan, Y. Hu, Q. Zhang, G. Chen, Mixed-metallic MOF based electrode materials for high performance hybrid supercapacitors, J. Mater. Chem. A. 5 (2017) 1094–1102. https://doi.org/10.1039/C6TA09805C.

[28] Y. Wang, Y. Liu, H. Wang, W. Liu, Y. Li, J. Zhang, H. Hou, J. Yang, Ultrathin NiCo-MOF Nanosheets for High-Performance Supercapacitor Electrodes, ACS Appl. Energy Mater. 2 (2019) 2063–2071. https://doi.org/10.1021/acsaem.8b02128.

[29] P. Wen, P. Gong, J. Sun, J. Wang, S. Yang, Design and synthesis of Ni-MOF/CNT composites and rGO/carbon nitride composites for an asymmetric supercapacitor with high energy and power density, J. Mater. Chem. A. 3 (2015) 13874–13883. https://doi.org/10.1039/c5ta02461g.

[30] Y. Jiao, G. Chen, D. Chen, J. Pei, Y. Hu, Bimetal-organic framework assisted polymerization of pyrrole involving air oxidant to prepare composite electrodes for portable energy storage, J. Mater. Chem. A. 5 (2017) 23744–23752. https://doi.org/10.1039/c7ta07464f.

[31] M.S. Rahmanifar, H. Hesari, A. Noori, M.Y. Masoomi, A. Morsali, M.F. Mousavi, A dual Ni/Co-MOF-reduced graphene oxide nanocomposite as a high performance supercapacitor electrode material, Electrochim. Acta. 275 (2018) 76–86. https://doi.org/10.1016/j.electacta.2018.04.130.

Chapter-VI

Prediction of capacitance using artificial neural networks for carbon nanofiber-based supercapacitors

6.1. Literature review

The use of carbon nanomaterials, such as activated carbons, nanoparticles, nanofibers, etc., as electrode materials for supercapacitors, has been widely studied because of their high surface area, high conductivity, and low production cost [2–4]. Compared to other electrode materials, CNFs are unique in that they are both flexible and possess tunable surface area, porosity, and fiber diameter. These characteristics make them ideal electrode materials for flexible supercapacitors. Hence, these CNFs have been extensively studied as electrode materials for supercapacitors [5]. However, the improvement in the specific capacitance is inadequate due to charge storage at the electrode-electrolyte interface. Activation and physical etching methods were used to engineer the microstructural properties of these CNFs to enhance their electrochemical performance. The microstructural properties, micro (<2 nm) and mesopore (2-50 nm) volumes, specific surface area (SSA), and fiber diameter greatly rely on the polymer precursor and carbonization process. In addition to these microstructural properties, supercapacitor performance depends on voltage window, scan rate, cell configuration, and electrolyte characteristics. As the performance of CNF-based supercapacitors depends on these many parameters, there is a significant need to develop a model that correlates these parameters to the performance of the supercapacitors. It is imperative to note that the development of a model does not only assist in predicting the performance of the supercapacitor, but also in planning the experiments to achieve the desired microstructural properties for enhancing its performance. The qualitative deviation of electrochemical performance with electrode SSA, micropore, and mesopore volumes has been examined through experimental studies. However, no physical model has been developed that predicts how these parameters interact to affect electrochemical performance in a synergetic manner. Alternatively, experimental data may be used to develop a data-driven machine-learning model that addresses this problem. In recent years, various machine learning models have been applied to determine the synergetic effects of multiple variables on the electrochemical performance of energy storage devices. Among different machine-learning models, an ANN was widely used to develop a model using complex and nonlinear data [6,7]. In a recent study, an ANN-based data-driven model developed that correlated microstructural characteristics of activated carbon electrodes, electrode synthesizing procedures, and operational conditions that affect the electrode's performance [8]. The developed model accurately predicted the performance of activated

carbon electrodes with an R-square value of 0.9. To our knowledge, there are no studies on CNF-based electrodes using data-driven machine-learning models. In this work, we have developed an ANN model to predict the performance of CNF-based electrodes using various independent input variables. Our goal is to examine the effect of input variables independently and synergistically on the prediction of specific capacitance of the CNF based electrode. Kim et al. proposed the required precision for screening improved electrolyte materials for supercapacitors at scan rates and current densities. Using different ML methods, the Bio-activated carbons demonstrated that they may be employed as electrode materials for the prediction of supercapacitor-specific capacitance due to their acceptable microstructure features, The ANN model predicted specific capacitance of supercapacitor of activated carbon material with remarkable accuracy ($R^2 = 0.93$). Table 1 demonstrates the use of ML approaches for diverse energy storage goals. The ML was used to discover relationships between physical and chemical characteristics such as the surface area, pore-volume, and activation temperature of certain materials and their operational characteristics, on the energy storage capabilities and performance of various advanced materials. Several models have been developed to interpretation for such performance of energy storage systems.

Table 6.1 Various machine learning models to predict the performances

Material	**Performance prediction approach**	**ML model**	**R^2(RMSE)**	**Reference**
BAC-based Supercapacitor	The performance of the supercapacitor was evaluated using BAC-based electrode variables (synthetic and operational).	RBF-NN	4.66 (0.99)	[2]
Supercapacitor performance	Electrolyte's kind, concentration, and heteroatoms-doped are considered input variables to predict the capacitance performance.	ANN	(0.964)	[9]
Supercapacitor (EDLCs) performance	Particular surface area, doping elements, a ratio of ID / IG, pore size ,and the test system (potential window) are all	ANN	(0.91)	[10]

	factors that affect specific capacitance.			

6.2. Methodology

6.2.1 Experimental data collection and preprocessing

The artificial neural network (ANN) machine learning methodology is used in this study to predict the specific capacitance of Activated carbon nanofibers as electrode material for flexible supercapacitors. The data was gathered using keywords such as "ACNFs," "CNF," and "biomass-based ACNFs," as well as a combination of "Energy storage," "Supercapacitor," and "Ultracapacitor", From 2007 to 2021, extensive searches were conducted utilizing important scientific search engines such as Google Scholar, Web of Sciences and Scopus. We took data from hundreds of published publications to train the ANN model. We aggregated over 100 published publications on Activated carbon nanofibers supercapacitors to create the database. Then, 70 data sets were retrieved, which included the morphological and chemical properties of the activated carbon nanofiber material (pore-volume, micropore volume, mesopore volume, and the specific surface area, electrode configuration (i.e., testing voltage window, electrolyte type, and concentration, and corresponding specific capacitance). Following that, the traits are chosen following existing scientific knowledge. In this study, seven variables are chosen as ANN method features: SSA, total pore volume, micropore volume, mesopore volume, carbonization temperature, nanofiber diameter, and voltage window.

The ANN model in this work was trained using seven input parameters, which include carbonization temperature (C_t), SSA, total pore volume (V_t), mesopore volume (V_{meso}), micropore volume (V_{mic}), nanofiber diameter (NFD), and voltage window (VW) and a single output parameter (Specific capacitance). Data for both input and output parameters were collected from 70 research articles reporting experimental data, each reference paper we took one single data set. The data was limited to the pristine CNFs-based electrode studies with the aqueous electrolytes and incorrect or outdated data can also impact the accuracy of the model so we considered only recent research articles data and inconsistent formatting or scaling of data can affect the model's accuracy so as a preprocessing step, all the parameters were normalized between 0 and 1. This normalization enables the ANN to learn more quickly since the output is more sensitive to changes in the input [8]. The following function was used to normalize the data in this study:

$$X_{\text{nor}} = \frac{X - X_{min}}{X_{max} - X_{min}} \qquad \text{----------7.1}$$

Where X denotes the variable value X_{nor} where X denotes value of the normalized variable, X_{max} and X_{min} correspond to the minimum and maximum values of the variables, respectively. During the analysis, the correlation coefficient index was used to determine the correlation between all variables. To measure linear dependence between all variables, Pearson correlation coefficients (PCCs) were used. By using a PCC, we checked whether two independent variables were co-correlated with each other and their linear correlation. PCC determines that there is a linear relationship between the variables by analyzing the following information:

$$PCC = \frac{\sum_{i=1}^{n}(x_i-\bar{x})\sum_{i=1}^{n}(y_i-\bar{y})}{\sqrt{\sum_{i=1}^{n}(x_i-\bar{x})^2}\sqrt{\sum_{i=1}^{n}(y_i-\bar{y})^2}} \rightarrow 1$$

where x and y represent independent and dependent variables and x and y are their mean values (x input variables and y for specific capacitance output variable). According to PCC, a positive value indicates that the dependent variable is impacted by the independent variable in a positive manner. It is possible to remove inputs that have no significant linear correlation or collinearity

6.2.2 Artificial neural network

It is possible for an ANN to learn rather than be programmed to make predictions. The ANN consists of input parameters, output parameters, and several hidden layers.

$$z = b_{ji} + \sum_{j=1}^{n} w_j f\left(\sum_{i=1}^{m} W_{ji}x_i\right) \rightarrow 2$$

As shown in equation 2 , depending on the weight (W_{ij}) and bias (B_i), the hidden layer will augment or cripple the received information. Herein, our goal is to use this ANN and the experimental data collected from the literature to build a data-driven model as shown in Fig.6.1 that can predict the specific capacitance performance of a CNF electrode-based supercapacitor. Our model was trained and tested using input and output data collected using the supervised machine learning method and the neural network toolbox in MATLAB 2021a. The artificial neural network consists of one hidden layer with a different number of neurons (11 to 23), a log-sigmoid activation function in a hidden layer, and a pure linear transfer function at the output layer.

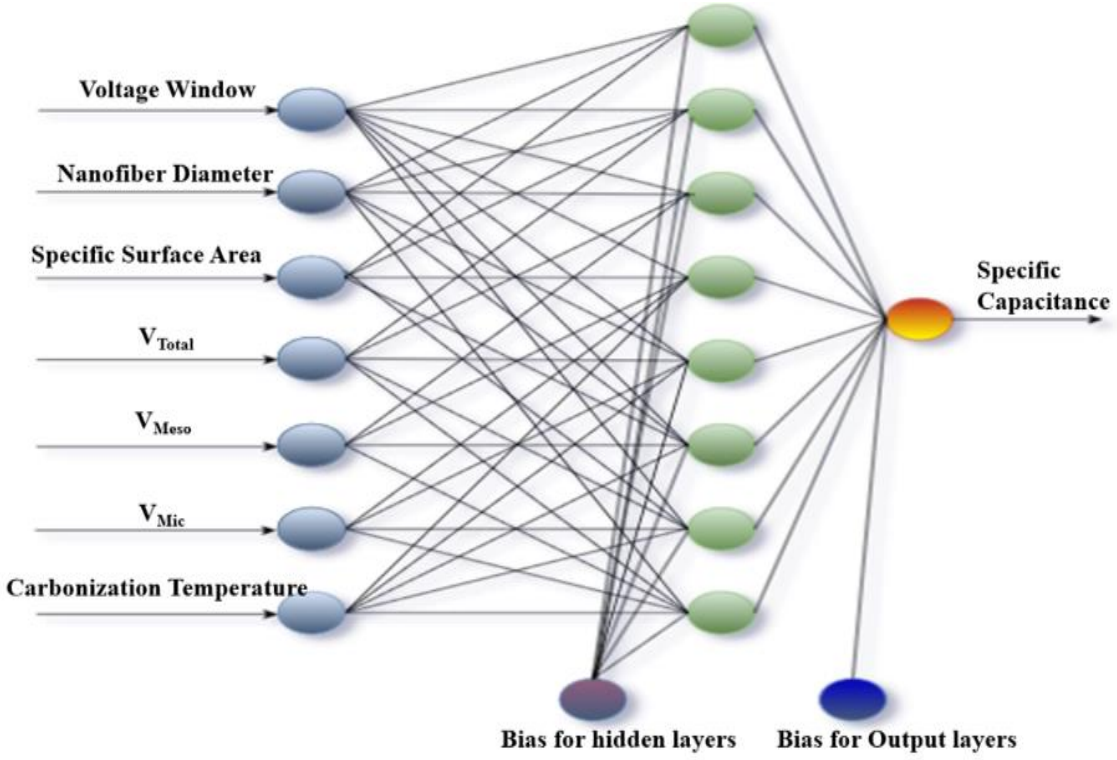

Figure 6.1. The neural network model of ANN used in this study.

An ANN model was trained using Levenberg–Marquardt with backpropagation of errors (LM-BP) [11] Levenberg-Marquardt algorithm appears to be the fastest method for training moderate-sized feedforward neural networks (up to several hundred weights). It also has an efficient implementation in MATLAB software, because the solution of the matrix equation is a built-in function. The data was divided into three subsets of 70%, 15%, and 15% for training, testing, and validation, respectively. The schematic illustration of the dataset preparation procedures and modeling implementation is shown in Fig.6.2.

$$RMSE = \sqrt{\left(\sum_{r=1}^{N}\left|S_r - \hat{S}_p\right|^2\right)/(N-1)} \qquad \rightarrow \ 3$$

$$R^2 = 1 - \sum_{1}^{N}\left(S_r - S_p\right)^2 / \sum_{1}^{N}\left(S_r - \hat{S}_r\right)^2 \qquad \rightarrow \ 4$$

Where S_r is the real value, S_p is the predicted value and $\hat{S}_r$ is average values of predicted values: A reliable model with allowable estimation errors is also characterized by RMSE values close to zero.

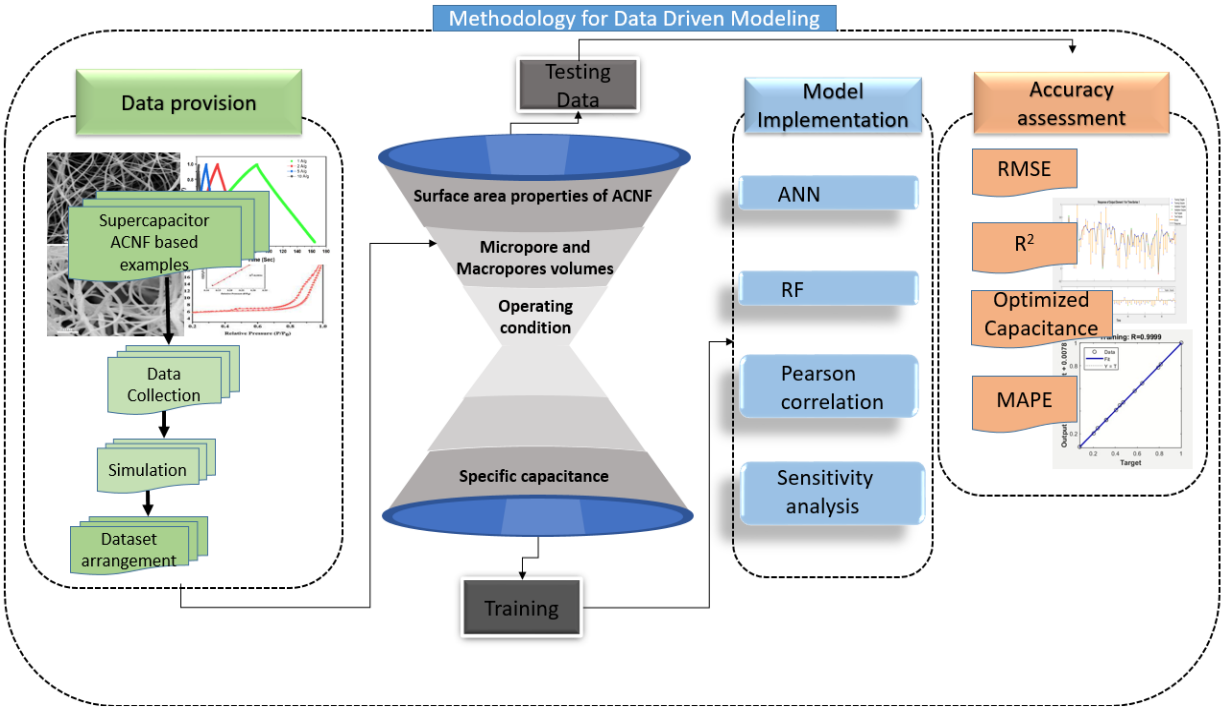

Figure 6.2. Schematic representation of data-driven modeling methodology

The number of neurons in an ANN model's hidden layer also significantly affects the prediction. To avoid overfitting (a high number of neurons) and offsetting (a low number of neurons), the number of neurons in the ANN model were optimized [12]. In this study, the number of neurons in hidden layers (hidden layer size) varied between 11 and 23. After the training, the performance of ANN was evaluated using the test data set. The error of ANN is determined by the root mean square error (RMSE) and correlation coefficient (R-Square) as above mentioned equations 3 and 4 respectively.

6.3. Results and Discussion

6.3.1 Result of ANN model

The Pearson correlation coefficient (PCC) was used to investigate the linear relationship and co-occurrence of input and output parameters, as shown in Fig.6.3. The PCC analysis reveals the dependency of the specific capacitance (output parameter) on all the input parameters. The reliance is in the decreasing order of SSA>V_{meso}>V_t>V_{mic}>C_t>VW>NFD, an independent input variable, showed a negative correlation (-0.16) with specific capacitance in the group of seven input parameters. Due to this, linear/inverse relationships cannot be used accurately to predict capacitance.

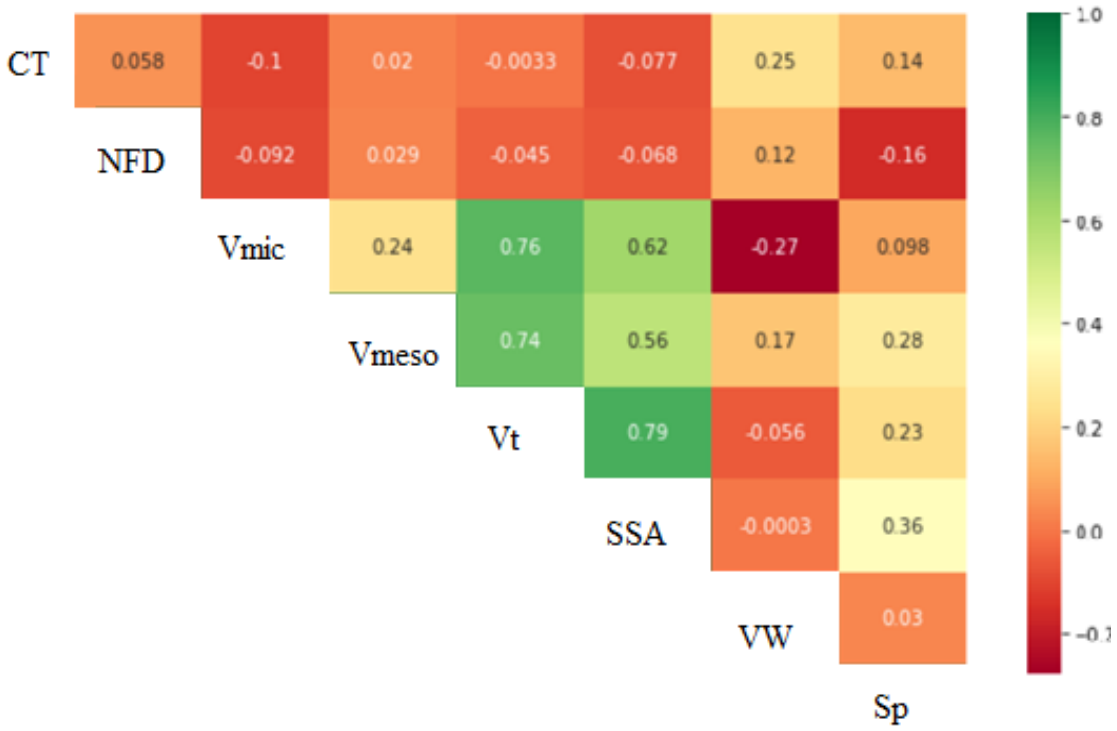

Figure 6.3. Pearson correlation matrix of the seven input variables and single output variable (specific capacitance).

Table 7.2 summarizes the effect of hidden layer size on the performance (as MSE & R square) of the training algorithm LM-BE. Increasing the number of neurons in the hidden layer from 11 to 19 resulted in a moderate decrease in the MSE from 0.0554 to 0.0031, and a further increase in neurons from 19 to 23 resulted in a moderate increase in the MSE to 0.006. As a result, a network with 19 neurons with least MSE value (0.0031) was used for sensitivity analysis studies. Furthermore, the network with 19 neurons demonstrated excellent correlation coefficients, with R-square values exceeding 0.95 for both training and testing achieved performance metrics are consistent across multiple training repetitions.

Table 6.2 Performance of ANN vs. Number of neurons in hidden layer

Hidden layer size	Training		Testing	
	MSE	R^2	MSE	R^2
11	0.01550	0.786	0.05540	0.918
13	0.00117	0.888	0.00700	0.921
15	0.00392	0.873	0.00310	0.967
17	0.00238	0.878	0.00835	0.910
19	0.00035	0.955	0.00286	0.955
21	0.00703	0.916	0.00160	0.854
23	0.00648	0.867	0.00200	0.866

Based on the results presented in Fig.6.4, it can be concluded that substantial agreement exists between the actual and predicted values of specific capacitance during both the training and testing phases. Mostly, ANN models can be compared to other machine learning models such as Decision Trees, Random Forests, Support Vector Machines, etc., so Random Forest (RF) model is used to compare the ANN accuracy results. ANN model showed better accuracy than RF model.

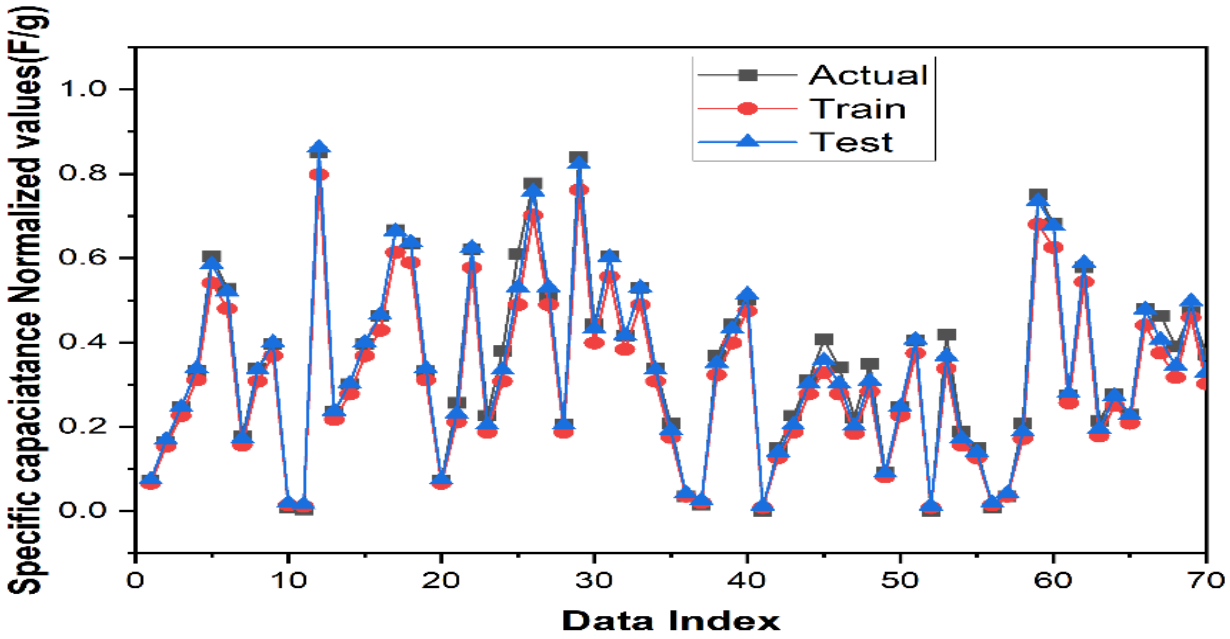

Figure.6.4 The predicted and actual values of specific capacitance in both test and training, using the ANN.

6.3.2 Sensitivity analysis

A sensitivity analysis was conducted by selecting input parameters precisely to determine how they affect the performance of CNF-based supercapacitors. The sensitivity analysis is presented in detail in Table 2. First, all input variables were considered in this analysis, and then a single input parameter was excluded from other analyses. Microstructural variables appear to have a substantial impact on the electrochemical performance of CNF based supercapacitors. According to this analysis, specific capacitance is greatly influenced by V_{meso} and SSA, in agreement with experimental observations [13]. In addition, the mean absolute percentage error (MAPE) was also used to quantify the degree of dependency. The MAPE values for the input set excluding V_t and the input set excluding SSA rose to 4.1% and 4.74%, respectively. This increase in error value indicates the importance of these microstructural properties on the

performance of CNF based supercapacitors. The input set without NFD, however, showed lower sensitivity, with MAPE of 1.57.

Table 6.3 Sensitivity analysis of the ANN model versus independent variables.

Model Input	Input set	MAPE		
		Train	Test	Total
	All	0.56	1.10	0.58
Structural	All exclude V_{mic}	3.20	3.56	2.93
	All exclude V_{meso}	4.63	4.20	4.10
	All exclude SSA	5.14	5.96	4.74
	All exclude V_t	2.10	2.90	2.01
	All exclude NFD	1.90	1.00	1.57
Carbonization	All exclude C_t	2.88	1.69	2.41
Operational	All exclude VW	3.12	3.39	2.84

6.4. Conclusion

The ANN model predicts the CNF-based electrode performance accurately using microstructural properties and operational parameters as input. In addition, the proposed model with 19 neurons showed a high R-square value of 0.95 and a lower MSE value of 0.003. The results of a sensitivity analysis on seven input parameters suggested that SSA and V_{meso} have a significant impact on electrode performance. In contrast, the input parameter NFD has a relatively small effect. The developed model can be employed to design nanofiber-based electrode materials experimentally, which reduces the need for labor-intensive experimentation to optimize the microstructural properties.

6.5 References

[1] P.K. Panda, A. Grigoriev, Y.K. Mishra, R. Ahuja, Progress in supercapacitors: Roles of two dimensional nanotubular materials, Nanoscale Adv. 2 (2020) 70–108. https://doi.org/10.1039/c9na00307j.

[2] J. He, D. Zhang, Y. Wang, J. Zhang, B. Yang, H. Shi, K. Wang, Y. Wang, Biomass-derived porous carbons with tailored graphitization degree and pore size distribution for supercapacitors with ultra-high rate capability, Appl. Surf. Sci. 515 (2020) 146020. https://doi.org/10.1016/j.apsusc.2020.146020.

[3] P.E. Lokhande, U.S. Chavan, A. Pandey, Materials and Fabrication Methods for Electrochemical Supercapacitors: Overview, Springer Singapore, 2020. https://doi.org/10.1007/s41918-019-00057-z.

[4] T.S. Mathis, N. Kurra, X. Wang, D. Pinto, P. Simon, Y. Gogotsi, Energy Storage Data

Reporting in Perspective—Guidelines for Interpreting the Performance of Electrochemical Energy Storage Systems, Adv. Energy Mater. 9 (2019). https://doi.org/10.1002/aenm.201902007.

[5] C.V.V. Muralee Gopi, R. Vinodh, S. Sambasivam, I.M. Obaidat, H.J. Kim, Recent progress of advanced energy storage materials for flexible and wearable supercapacitor: From design and development to applications, J. Energy Storage. 27 (2020) 101035. https://doi.org/10.1016/j.est.2019.101035.

[6] L. Himanen, A. Geurts, A.S. Foster, P. Rinke, Data-Driven Materials Science: Status, Challenges, and Perspectives, Adv. Sci. 6 (2019). https://doi.org/10.1002/advs.201900808.

[7] M. Safaei-Farouji, H. Vo Thanh, Z. Dai, A. Mehbodniya, M. Rahimi, U. Ashraf, A.E. Radwan, Exploring the power of machine learning to predict carbon dioxide trapping efficiency in saline aquifers for carbon geological storage project, J. Clean. Prod. 372 (2022) 133778. https://doi.org/10.1016/j.jclepro.2022.133778.

[8] M. Rahimi, M.H. Abbaspour-Fard, A. Rohani, Synergetic effect of N/O functional groups and microstructures of activated carbon on supercapacitor performance by machine learning, J. Power Sources. 521 (2022) 230968. https://doi.org/10.1016/j.jpowsour.2021.230968.

[9] A.A. Oladipo, N,S co–doped biocarbon for supercapacitor application: Effect of electrolytes concentration and modelling with artificial neural network, Mater. Chem. Phys. 260 (2021) 124129. https://doi.org/10.1016/j.matchemphys.2020.124129.

[10] S. Zhu, J. Li, L. Ma, C. He, E. Liu, F. He, C. Shi, N. Zhao, Artificial neural network enabled capacitance prediction for carbon-based supercapacitors, Mater. Lett. 233 (2018) 294–297. https://doi.org/10.1016/j.matlet.2018.09.028.

[11] M.J. Willis, C. Di Massimo, G.A. Montague, M.T. Tham, A.J. Morris, Artificial neural networks in process engineering, IEE Proc. D Control Theory Appl. 138 (1991) 256–266. https://doi.org/10.1049/ip-d.1991.0036.

[12] S. Karsoliya, Approximating Number of Hidden layer neurons in Multiple Hidden Layer BPNN Architecture, Int. J. Eng. Trends Technol. 3 (2012) 714–717.

[13] L. Xie, F. Su, L. Xie, X. Guo, Z. Wang, Q. Kong, G. Sun, A. Ahmad, X. Li, Z. Yi, C. Chen, Effect of pore structure and doping species on charge storage mechanisms in porous carbon-based supercapacitors, Mater. Chem. Front. 4 (2020) 2610–2634. https://doi.org/10.1039/d0qm00180e.

CHAPTER-VII

Overall Conclusions

Overall, we have demonstrated the synthesis of diverse ternary composite electrodes through electrospinning, electrodeposition, and ultrasound-assisted methods to prepare core-shell, hollow, and nanostructured electrodes. Further electrochemical performance of these electrode materials is assessed for supercapacitors. Following are the findings from the research conducted in this thesis.

- Incorporating MXene into the electrodes of a carbon nanofibrous host created abundant active sites and efficient electron pathways. Simultaneously, the addition of RuO_2 nanoparticles boosted capacitance by augmenting redox reaction sites. The performance improvement achieved by embedding both ruthenium oxide and MXene into the nanofibrous electrode surpassed that of binary composite electrodes.
- Applying a PANI layer to the MXene-infused carbon nanofiber electrode not only enhanced the specific capacitance of the ternary composite electrode but also increased the flexibility of the nanofibrous electrodes. The increase in coating thickness led to larger fiber diameter and capacitance, attributed to the expanded surface area and higher content of pseudocapacitive material.
- Nanostructured cobalt oxide coating improved the specific surface area, and the gaps between tiny pillars helped in accommodating volume expansion when the battery charges and discharges. This improved the cyclic performance. In addition, hollow composite fibers embedded with MXene showed great performance as electrodes. This happened because it improved electron transport and the electrode-electrolyte interface.
- When Co-MOF nanoparticles are embedded, they trigger the graphitization of CNF, acting as a catalyst. This enhanced graphitization, combined with the impressive surface area of MOF, leads to a demonstration of excellent electrochemical performance.
- The proposed ANN model predicts the CNF-based electrode specific capacitance performance precisely which allows them to learn complex relationships that would be difficult to identify using traditional methods. The sensitivity analysis on seven input parameters suggested that SSA and V_{meso} have a noteworthy impact on specific capacitance (electrode performance).

In summary, ternary composite electrodes demonstrated excellent electrochemical performance compared to binary composite and pristine electrodes due to the synergistic effect of the MXene and pseudocapacitive.

Chapter 8

Scope for further investigations

In this thesis, we have synthesized a diverse array of nanofibrous electrodes, each composed of MXene-based ternary composites tailored for applications in supercapacitors. Our investigative efforts extended beyond the mere synthesis of these electrodes; we meticulously probed into their physicochemical attributes, drawing intricate connections between these characteristics and the electrochemical performance they exhibited.

Despite the depth of our exploration, we acknowledge that the landscape of knowledge in this domain remains expansive, calling for further inquiry to refine our insights. To better understand the topic, it is important to carefully look at certain aspects. These include a detailed examination of how much MXene is in the main material, a deep understanding of the surface termination groups of MXene, adjusting the spaces between layers in a thoughtful way, and tuning the surface area. Additionally, we see a big opportunity to combine these new materials with different types of biomass derived carbon or biomass derived activated carbon materials. Based on the valuable insights we gained from our study, we propose following studies as future investigations:

Optimization of MXene Content and Interlayer Spacing: A dedicated effort towards fine-tuning the MXene content within the composite and strategically engineering interlayer spacing is warranted.

Exploration of Surface Termination Groups: A comprehensive study into the role played by surface termination groups of MXene in influencing the electrochemical performance of supercapacitors is essential.

Synthesis of Nitride-Based MXenes: Venturing into the synthesis of MXenes with a nitride-based composition represents an exciting frontier. The subsequent assessment of their electrochemical performance promises to broaden our understanding and potentially unveil novel applications.

List of publications

Kiran Donthula, Ramsagar Vooradi, Venkata Suresh Patnaikuni and Manohar Kakunuri,Binder-free Ruthenium Oxide/MXene/Carbon Nanofiber Ternary Composite Electrode for Supercapacitors. Journal of the Electrochemical Society, 2023, 170 030508 (SCI Indexed Journal **I.F 4.37**). DOI 10.1149/1945-7111/acbee5

Kiran Donthula, Usha Rani Malothu, Ramya Araga, Ramsagar Vooradi, Venkata Suresh Patnaikuni and Manohar Kakunuri, Flexible Polyaniline/MXene/CNF Composite Nanofibrous Mats as High-performance Supercapacitor Electrodes. Polymer Composite,1-14, (**I.F 5.2**). https://doi.org/10.1002/pc.27646.

Kiran Donthula, Naresh Thota, Sarat Anne, Manohar Kakunuri" Prediction of capacitance using artificial neural networks for carbon nanofiber-based supercapacitors Computer Aided Chemical Engineering 52, 1015-1020

Kiran Donthula, Ramya Araga, Naresh Thota, Subramanian Sundarrajan, Seeram Ramakrishna and Manohar Kakunuri, Hierarchically structured carbon nanofibers with embedded MXene and coated with cobalt oxide as high-performance electrode for supercapacitors, Journal of Energy Storage (Under Review: Comments received).